National School on Neutron and X-ray Scattering

Argonne and Oak Ridge National Laboratories

X-ray and Neutron Reflectometry

June 23, 2010

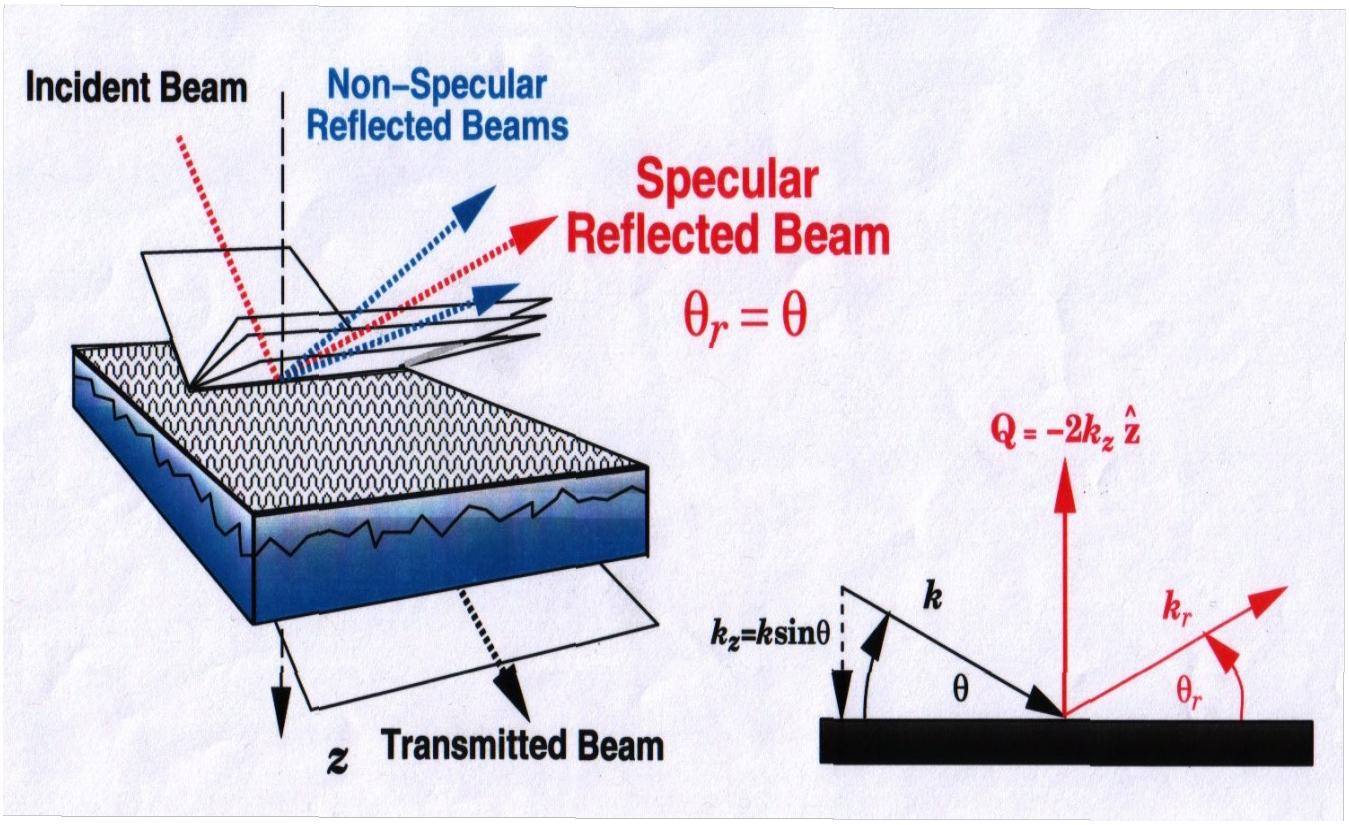

(Figure courtesy of Norm Berk)

C.F.Majkrzak, *NIST Center for Neutron Research*,
Gaithersburg, MD

PROBES OF THE MICROSTRUCTURE OF SURFACES AND INTERFACES

photons, electrons, neutrons, atom and ion beams, miniature mechanical devices

* DIRECT IMAGING (REAL SPACE)

  e.g.:

  - optical microscopy (~ 1000 x magnification)
  - scanning electron microscopy (SEM) (orders of magnitude higher magnification than possible with light)
  - transmission electron microscopy (TEM)
  - atomic force microscopy (AFM)

* DIFFRACTION (RECIPROCAL SPACE)

  e.g.:

  - low energy electron diffraction (LEED)
  - spin polarized LEED (SPLEED)
  - reflection high energy electron diffraction (RHEED)
  - ellipsometry (optical polarimetry)
  - x-ray reflectometry
  - neutron reflectometry

For quantitative measurements of depth profiles along a normal to the surface, x-ray and neutron reflectometry are particularly useful because of their relatively weak interactions with condensed matter and the fact that these interactions can be described accurately by a comparatively simple theory. In the case of electron diffraction, on the other hand, the potential is non-local and the scattering is non-spherical, relatively strong and highly energy-dependent. For atom diffraction, the description of the interaction potential can be even more complicated.

Principal Uses and Advantages of Neutron Reflectometry:

* For the specular condition, provides the chemical (isotopic) scattering length density (SLD) depth profile along the surface normal with a spatial resolution approaching half a nanometer.

* With polarized neutrons, provides the *vector* magnetization depth profile of a ferromagnetic material.

* Isotopic contrast, particularly applicable to hydrogen and deuterium.

* A non-destructive probe which can penetrate macroscopic distances through single crystalline substrates, making possible reflection studies of films in contact with liquids within a closed cell.

* As a consequence of the relatively weak interaction between the neutron and material, a remarkably accurate theoretical description of the reflection process and quantitative analysis of the data is possible, although the Born approximation is often not valid and an “exact” or “dynamical” formulation is required.

> The great success in using neutron reflection/diffraction to study thin film systems of hard condensed matter, in particular the structures and fundamental interactions in magnetic materials, is largely due to the ability to tailor, with atomic-layer accuracy and precision, single-crystalline, layered sandwiches and superlattices (using vapor deposition techniques such as molecular beam epitaxy in ultra-high vacuum). Advances in film deposition techniques and lithography continue at a remarkable rate.

> Similarly, neutron reflectometry in principle can be applied as a probe to further our understanding of the structure and function of molecules in lipid membranes, of relevance in biology and bioengineering, when comparable control over the fabrication of model systems is achieved. Great progress has been made toward realizing this goal in practice. However, we are still at a relatively early stage of development in our ability to engineer soft condensed matter films on atomic and nanometer scales. Progress can be expected as efforts in creating and manipulating membrane / molecular systems accelerates.

> Employing phase-sensitive methods in reflectivity measurements ensures a unique scattering length density (SLD) depth profile. Additional application of hydrogen / deuterium substitution techniques and comparison with molecular dynamics calculations assures a correspondingly high degree of certainty of obtaining an unambiguous chemical composition depth profile.

"SPECULAR" OR "MIRROR" REFLECTION OF A WAVE

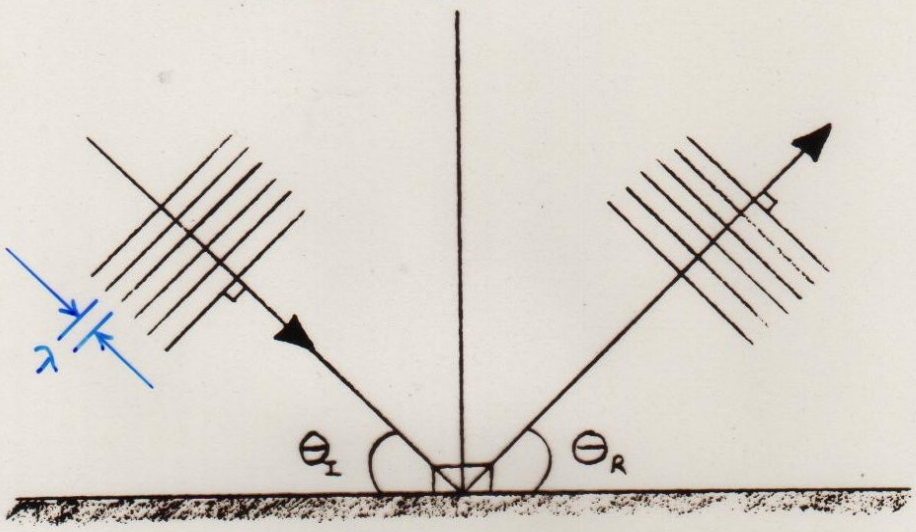

ANGLE OF INCIDENCE θ_I
= ANGLE OF REFLECTION θ_R

REFRACTION OF A LIGHT WAVE

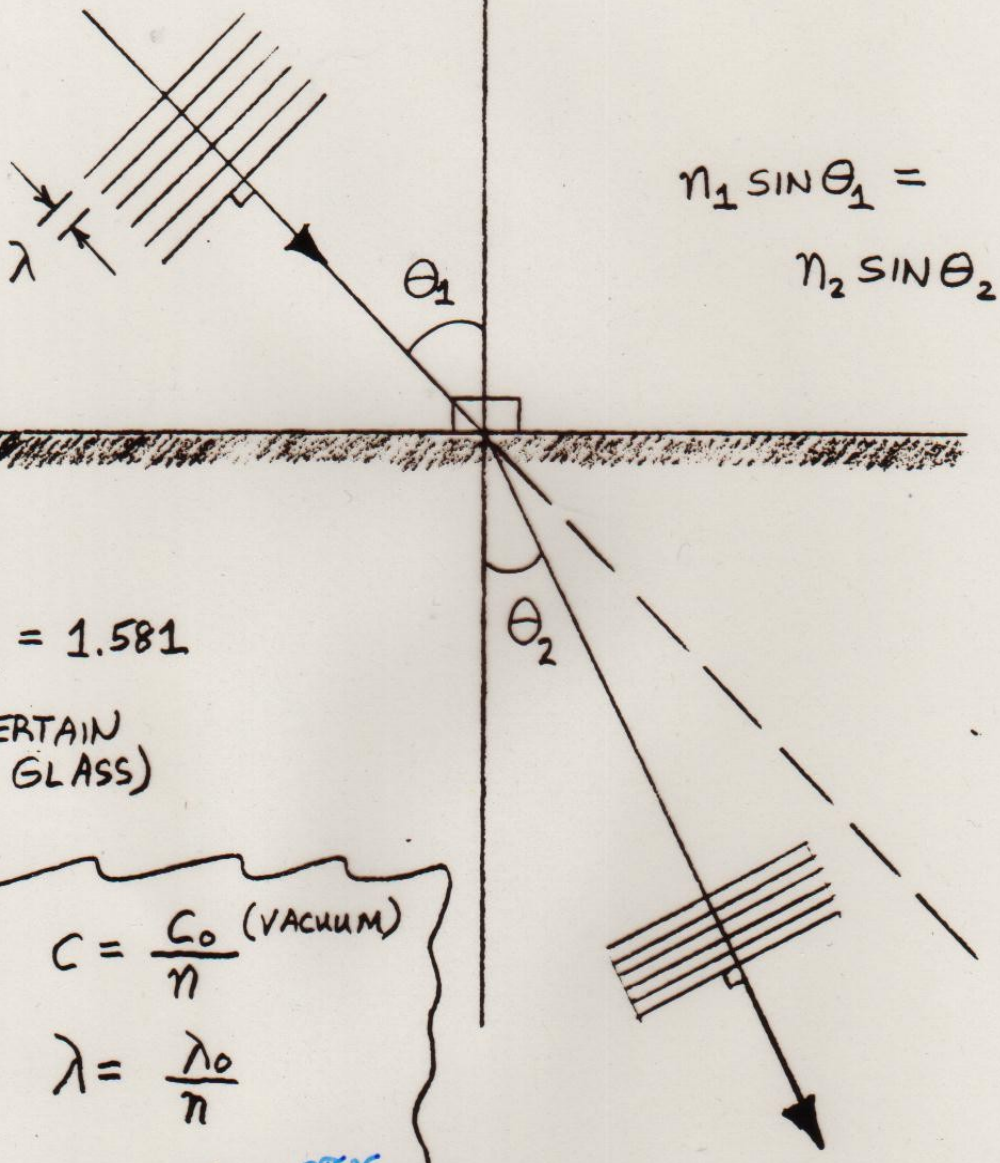

e.g. $n_2 = 1.581$
(CERTAIN GLASS)

WAVE SPEED $c = \frac{c_0}{n}$ (VACUUM)

WAVE-LENGTH $\lambda = \frac{\lambda_0}{n}$

WAVE-VECTOR $k = n k_0 = \frac{2\pi\nu}{c}$

FREQUENCY ν = CONSTANT

REFRACTIVE INDEX n DEPENDS ON MATERIAL AND WAVELENGTH OF THE LIGHT

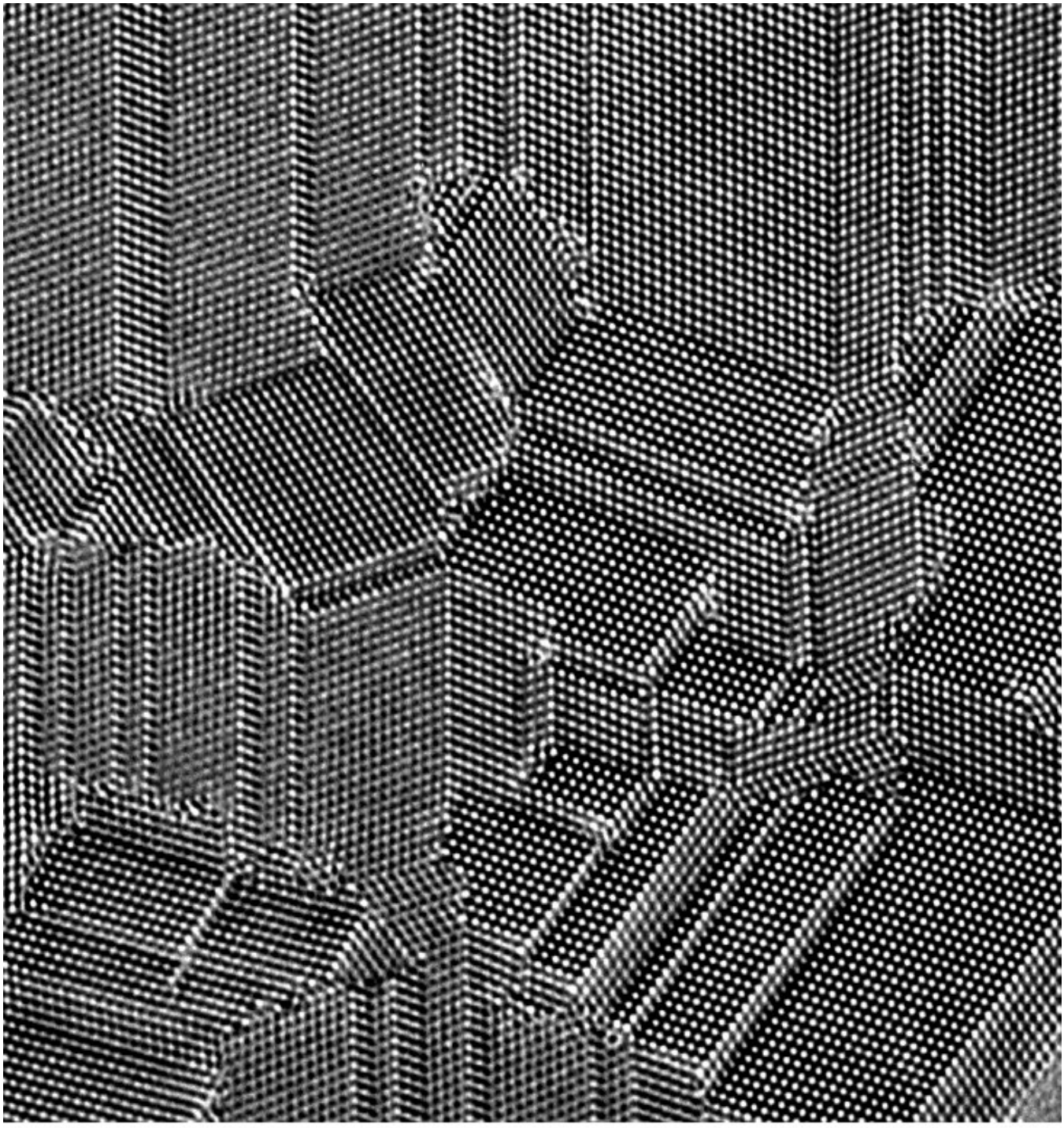

Atomic resolution micrograph of multiply-twinned nanocrystalline film of Si. (C. Song)

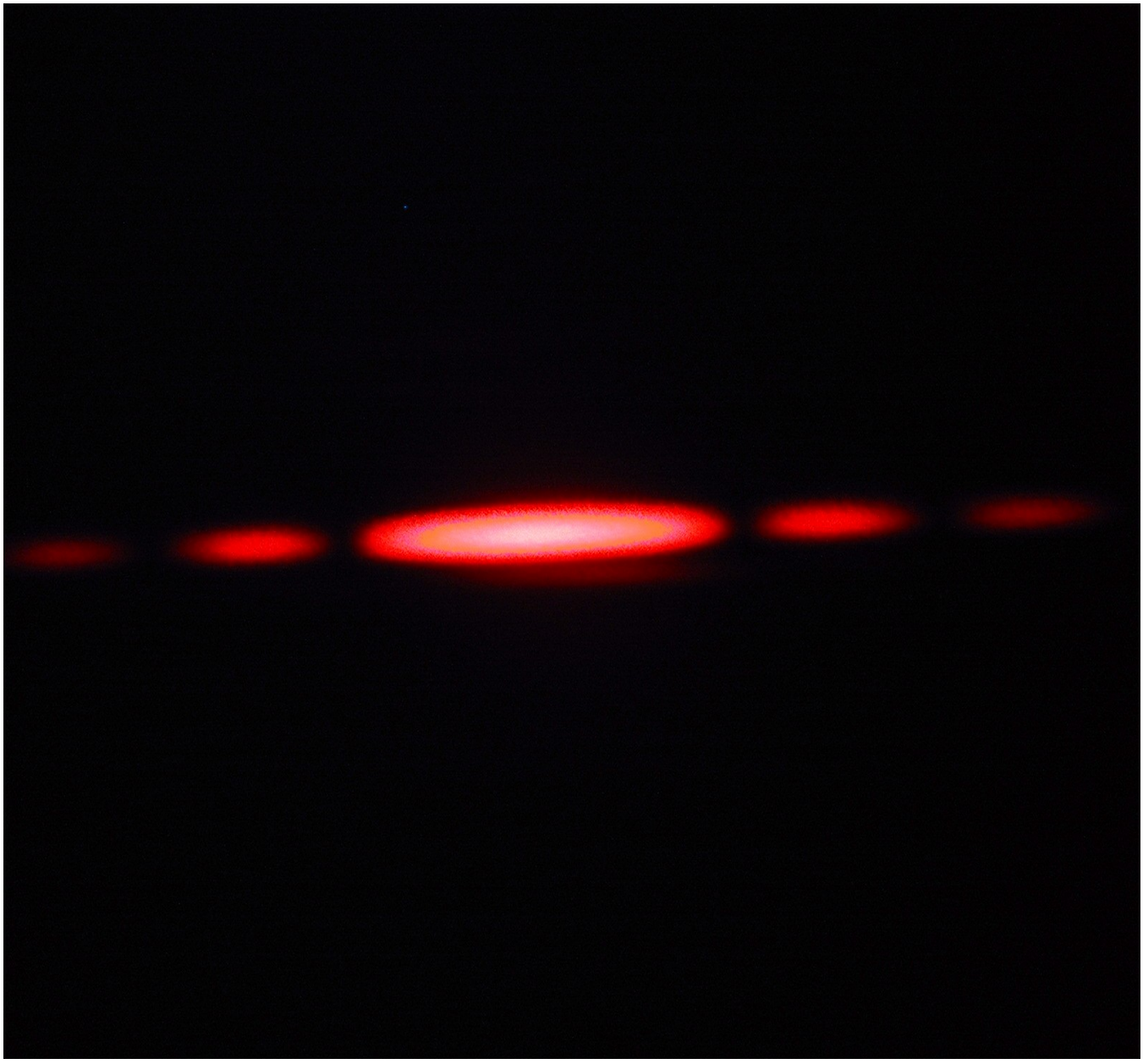

Single slit monochromatic light diffraction – Maleki/Newman at www1.union.edu.

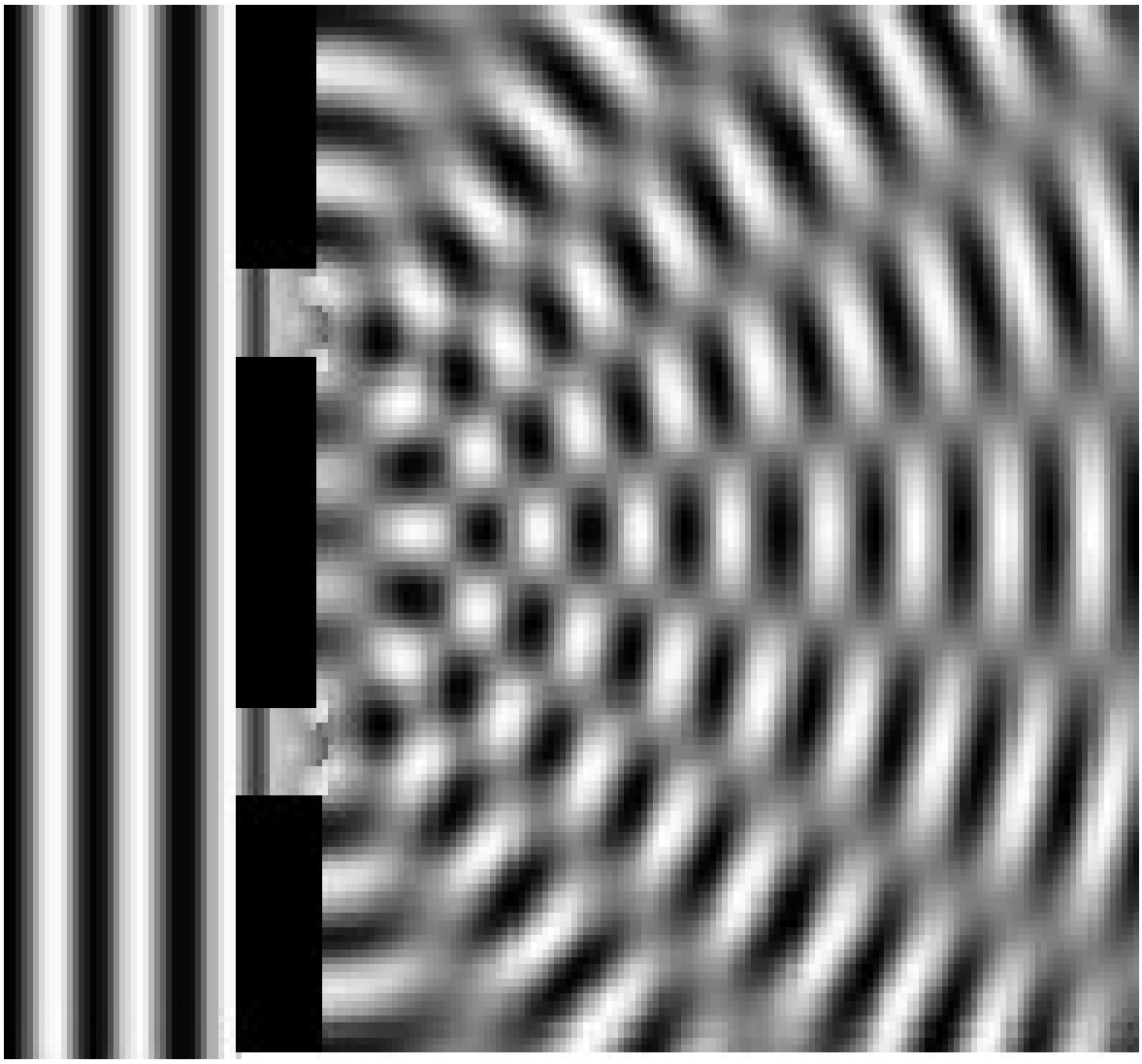

Water wave diffracting through a double aperture (from left to right) – B.Crowell, *Light and Matter*, www.vias.org/physics.

(from Photonics by Saleh & Teich)

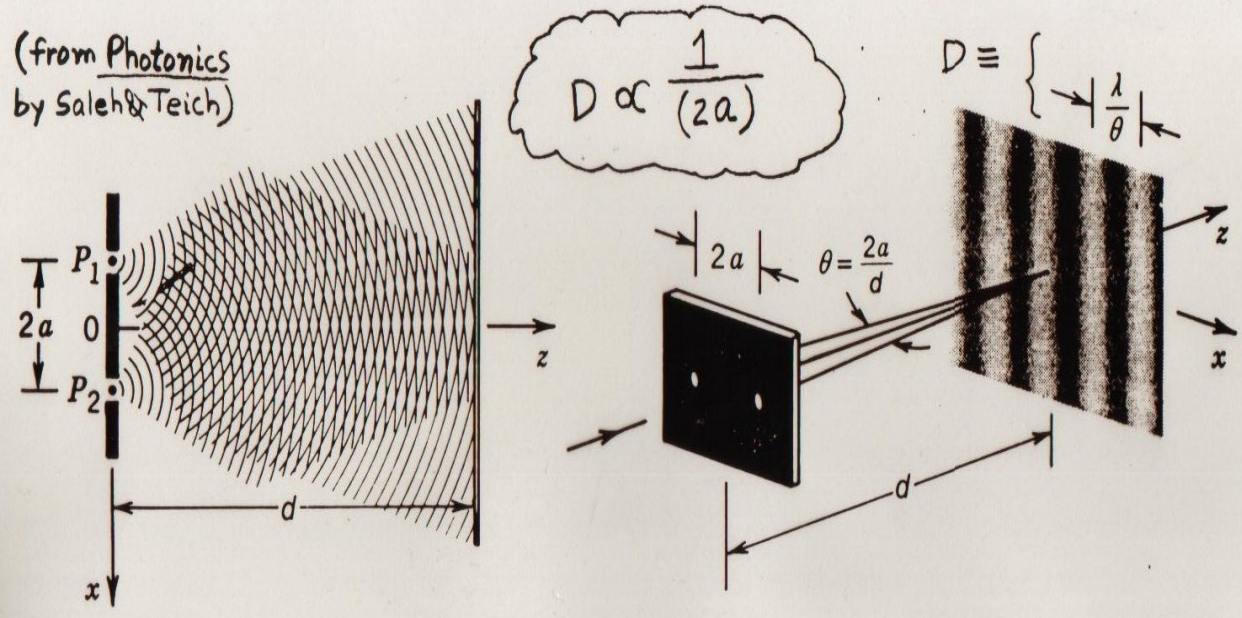

Figure 2.5-6 Interference of two spherical waves of equal intensities originating at the points P_1 and P_2. The two waves can be obtained by permitting a plane wave to impinge on two pinholes in a screen. The light intensity at an observation plane a distance d away takes the form of a sinusoidal pattern with period $\approx \lambda/\theta$.

DIFFRACTION PATTERN WHICH RESULTS FROM THE COHERENT SUPERPOSITION OF TWO WAVES (AMPLITUDES OF THE TWO WAVES ADD TOGETHER AT ANY GIVEN POINT IN SPACE)

A CHARACTERISTIC RECIPROCAL RELATIONSHIP EXISTS BETWEEN THE POSITIONS OF THE INTENSITY MAXIMA IN THE DIFFRACTION PATTERN AND THE DISTANCE SEPARATING THE OBJECTS CAUSING THE SCATTERING.

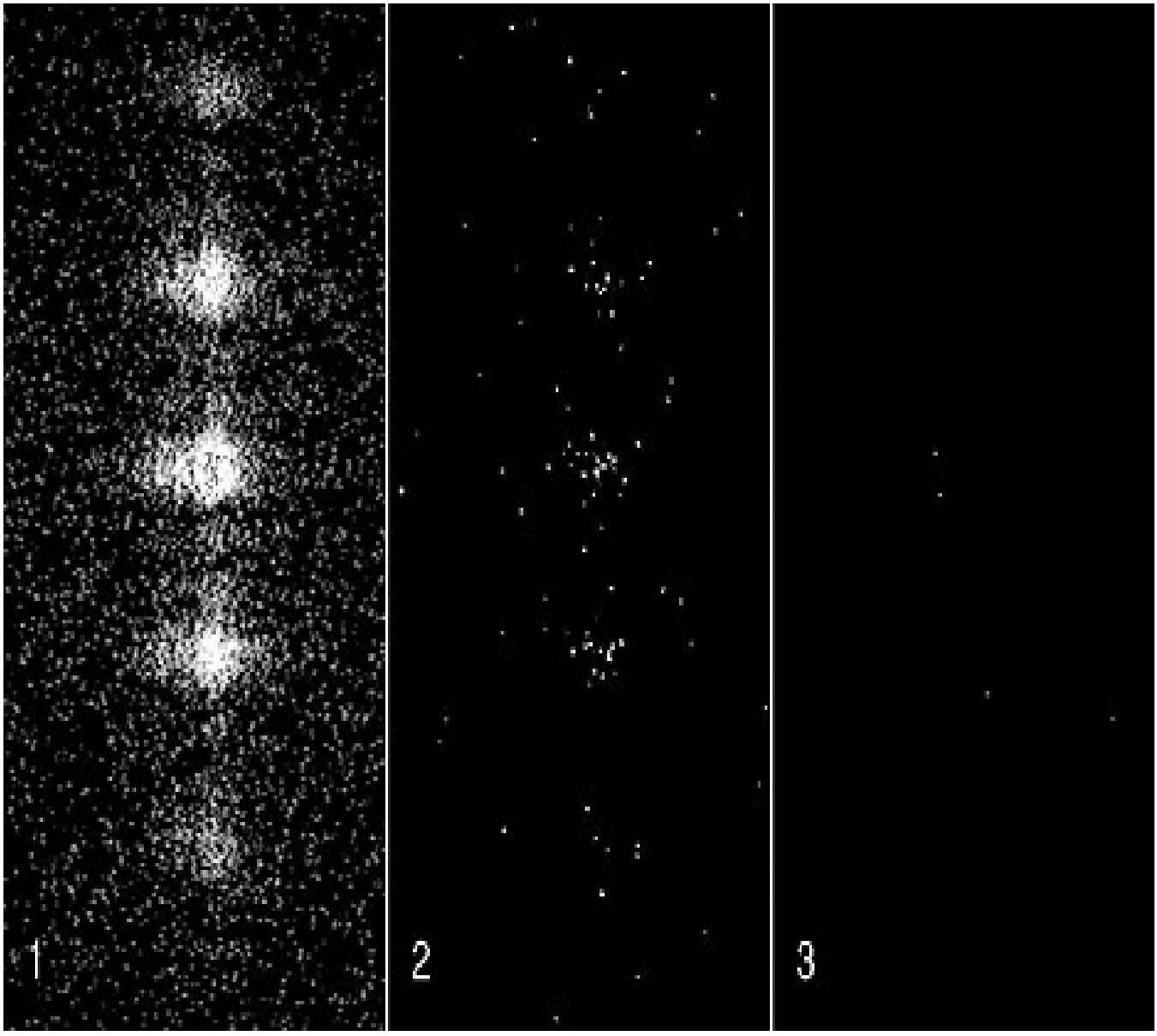

Wave interference patterns produced by monochromatic laser light diffracting through a triple slit aperture for various intensities – L.Page (www.vias.org/physics). This is a dramatic illustration of wave-particle duality.

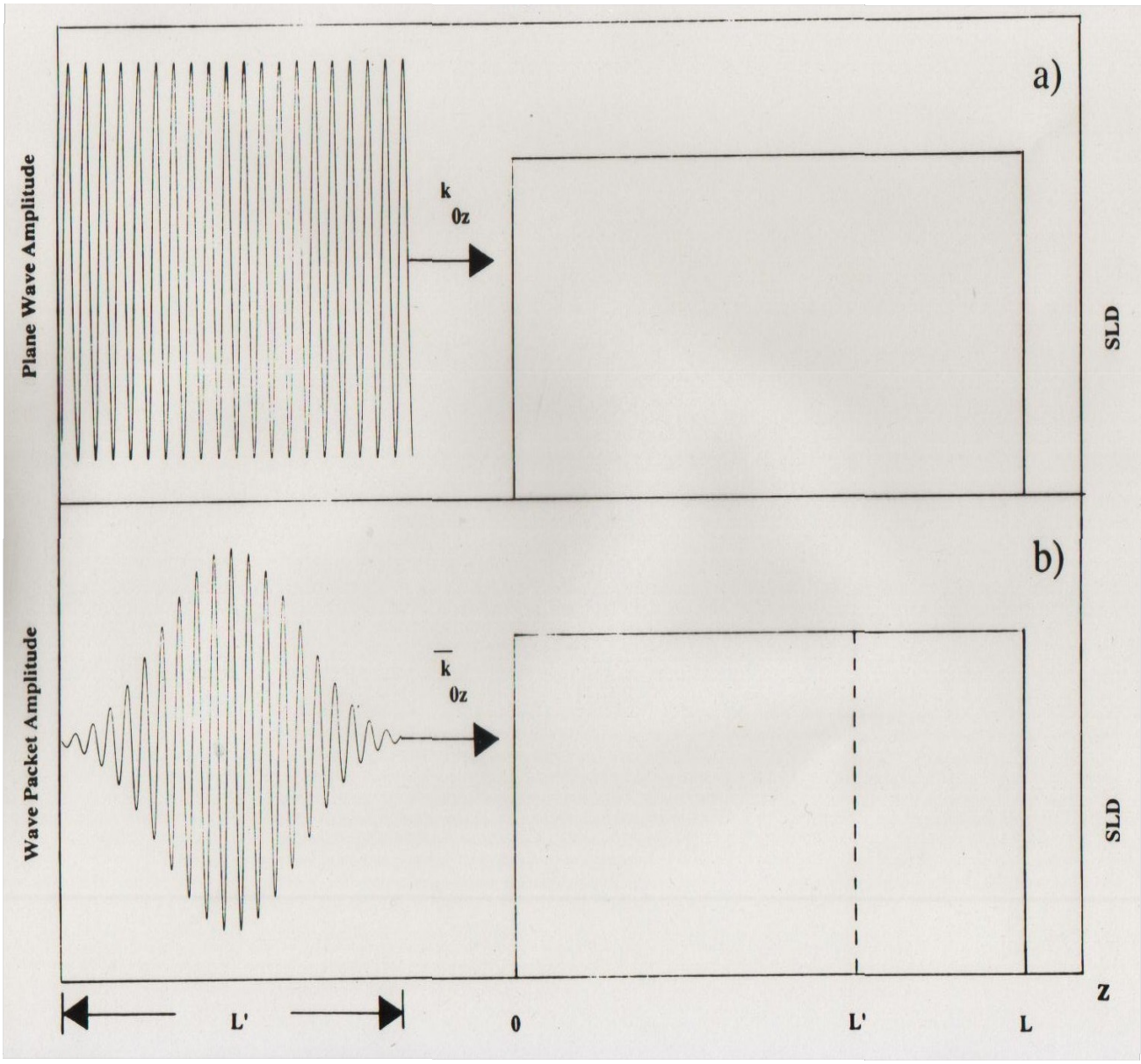
a)
Plane Wave Amplitude
k
0z
SLD
b)
Wave Packet Amplitude
k
0z
SLD
z
L'
0
L'
L

$$\text{Reflectivity} = \frac{\text{Number of reflected neutrons}}{\text{Number of incident neutrons}} = |r|^2$$

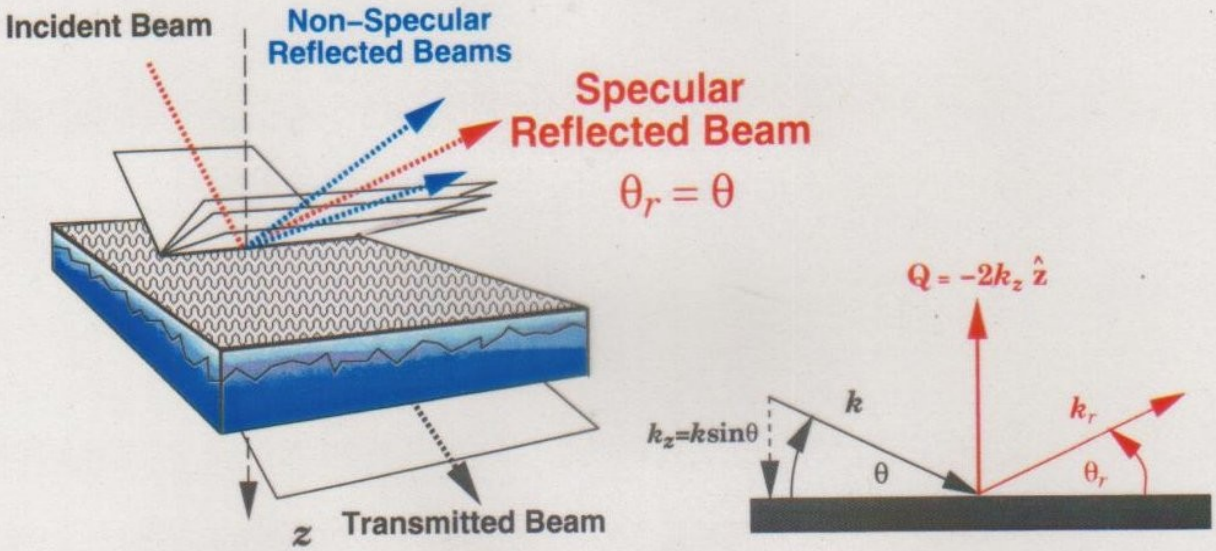

Specular reflection: $\bar{\rho}(z) = \langle \rho(x,y,z) \rangle_{xy}$

Non–Specular reflection: $\Delta\rho(x,y,z) = \rho(x,y,z) - \bar{\rho}(z)$

(AFTER N.F.BERK ET AL.)

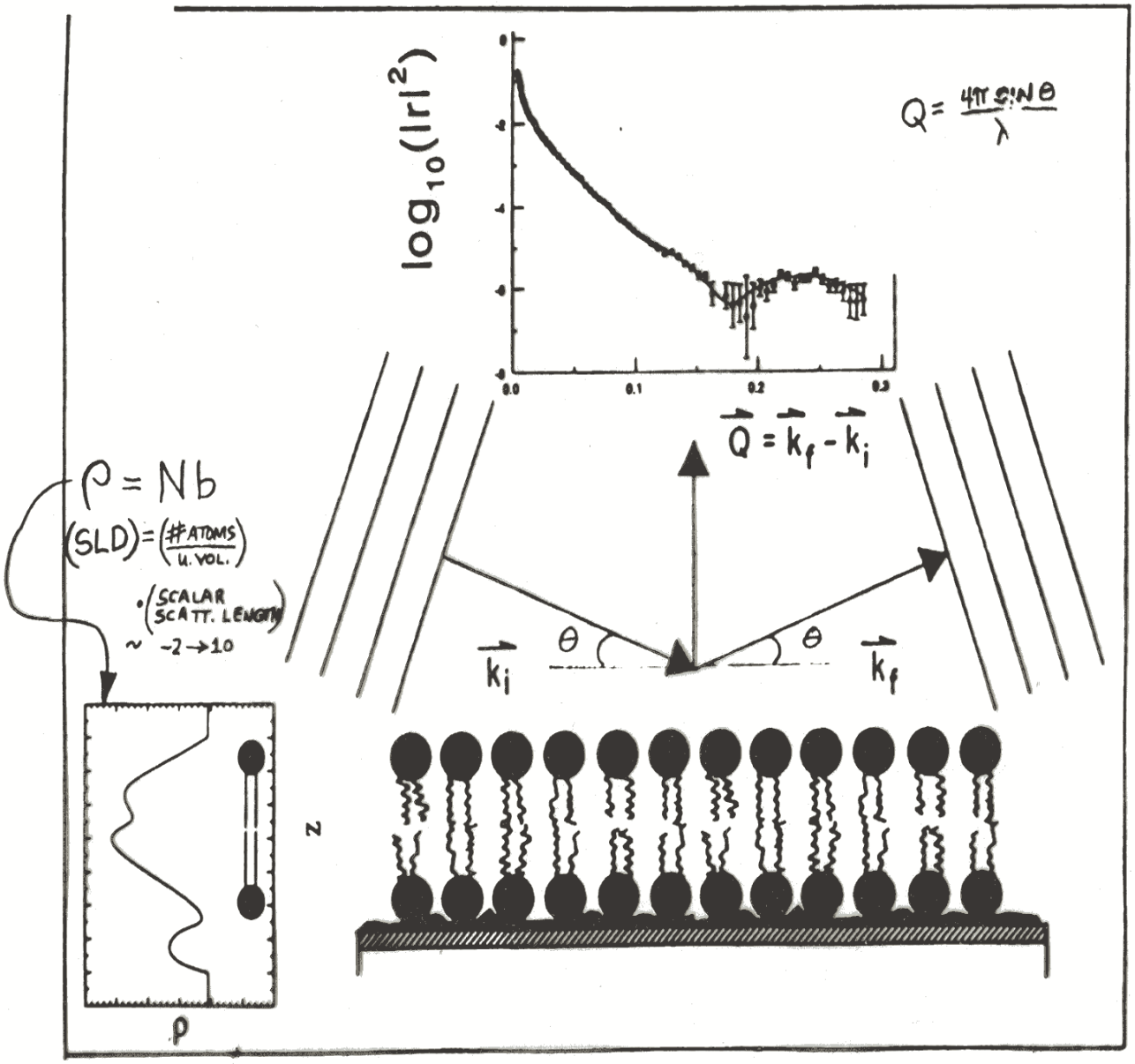
$\log_{10}(|r|^2)$
0.0
0.1
0.2
0.3
$Q = \frac{4\pi \sin\theta}{\lambda}$
$\vec{Q} = \vec{k}_f - \vec{k}_i$
$\rho = Nb$
(SLD) = (#ATOMS / U. VOL.) · (SCALAR SCATT. LENGTH)
~ −2 → 10
θ
θ
$\vec{k}_i$
$\vec{k}_f$
z
ρ

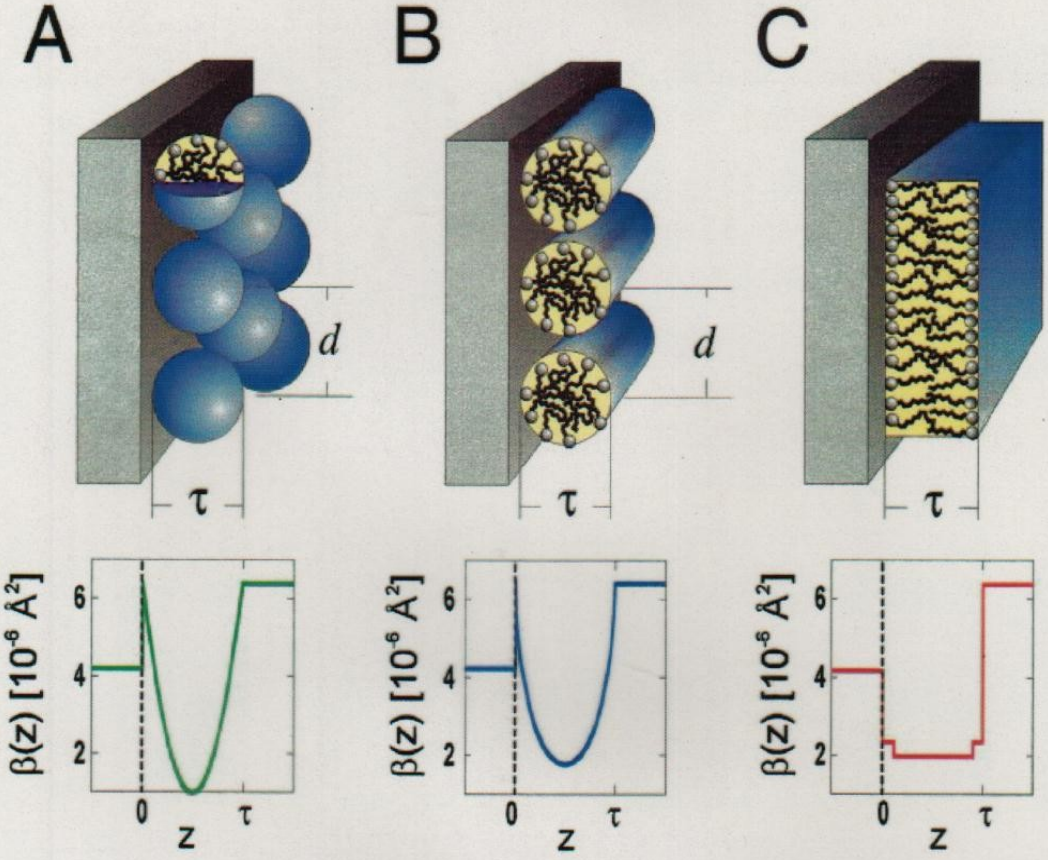

FIG. 1. (Color) Schematic diagram of adsorbed layer structures consisting of (A) spherical micelles, (B) cylindrical micelles, and (C) a bilayer, including the film thickness τ and interaggregate spacing d. Also shown are examples of neutron scattering length density profiles normal to the interface, $\beta(z)$, corresponding to each structure at the quartz/D_2O interface at a fractional surface coverage of 0.55. The head-group and alkyl tails of the surfactants have different scattering length densities, but because of the arrangement of the molecules this is only apparent in the bilayer $\beta(z)$.

single-crystal quartz block and reflected from the quartz-solution interface were recorded as a function of angle of incidence. The off-specular background, including any signal due to scattering from the bulk solution [15], was subtracted to give the reflection coefficient of the surfactant-coated interface. All solutions used were above their critical micelle or aggregation concentration, a condition which leads to a saturated adsorbed film at the solid-solution interface.

The cationic surfactant tetradecyltrimethylammonium bromide (TTAB) forms nearly spherical micellar aggregates consisting of approximately 80 molecules in bulk solution. Small angle neutron-scattering measurements [16] give mi-

FIG. 2. 200×200-nm² AFM tip deflection images of (A) spherical TTAB aggregates adsorbed onto quartz from water solution, (B) cylindrical TTAB aggregates adsorbed onto quartz from an aqueous 200mM NaBr solution, and (C) planar DDAB bilayer adsorbed onto quartz from water solution. Long-wavelength undulations visible in (B) and (C) arise from roughness in the underlying quartz.

THE NEUTRON AS A PLANE WAVE PROPAGATING IN FREE SPACE

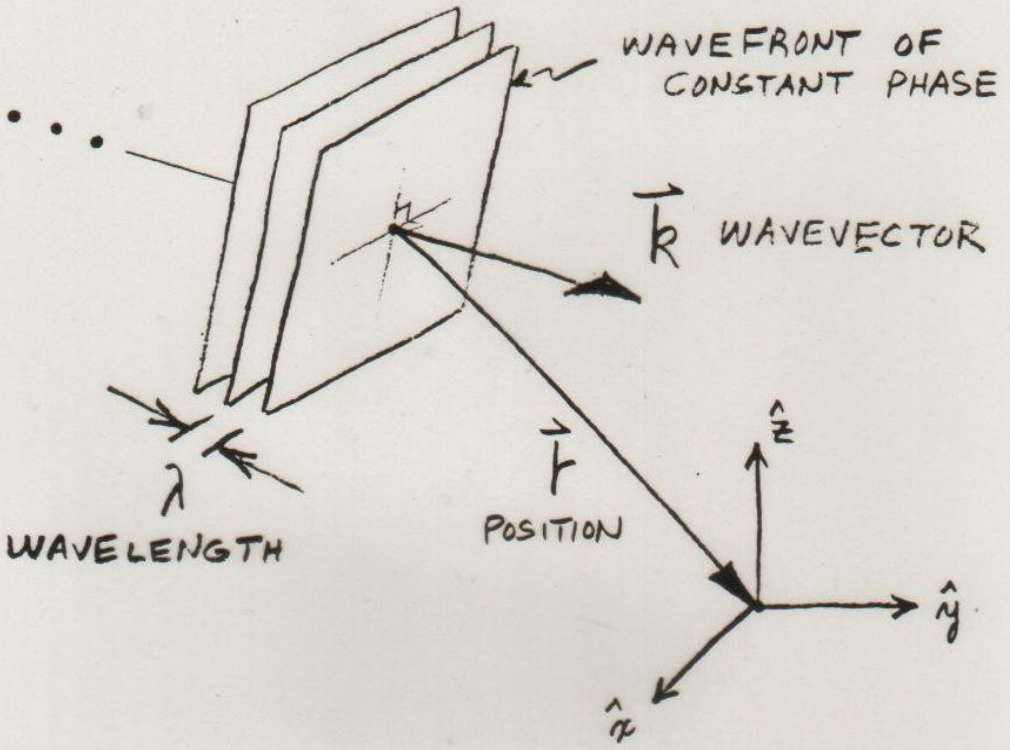

WAVEFUNCTION

$$\Psi \propto e^{i \vec{k}_0 \cdot \vec{r}}$$

$$\begin{cases} \vec{k}_0 = k_{0x}\hat{x} + k_{0y}\hat{y} + k_{0z}\hat{z} \\ \vec{r} = x\hat{x} + y\hat{y} + z\hat{z} \end{cases}$$

FOR $\vec{k}_0$ ALONG $\hat{z}$, FOR EXAMPLE,

$$\Psi \propto \cos(k_{0z} z) + i \sin(k_{0z} z)$$

$$= \left(\frac{2\pi}{\lambda} z\right)$$

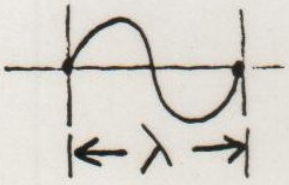

$|\Psi|^2 \propto$ PROBABILITY OF THE NEUTRON BEING THERE

FOR ELASTIC INTERACTIONS
TOTAL ENERGY OF THE
NEUTRON IS CONSTANT

TOTAL ENERGY = KINETIC ENERGY
+ POTENTIAL ENERGY

= CONSTANT

WAVE EQUATION OF MOTION
(SCHROEDINGER EQUATION)

$$\left[\frac{-\hbar^2}{2m}\nabla^2 + V(\vec{r})\right]\Psi = E\Psi$$

K.E. P.E. T.E.

$$\nabla^2 = \frac{\partial^2}{\partial x^2} + \frac{\partial^2}{\partial y^2} + \frac{\partial^2}{\partial z^2}$$

IN VACUUM

$$K.E._0 = \frac{\hbar^2 k_0^2}{2m}$$

IN THE CONTINUUM LIMIT

$$V(\vec{r}) = \frac{2\pi\hbar^2}{m} \sum_{j=1} N_j b_j = \frac{2\pi\hbar^2}{m}\rho$$

N_j: NUMBER OF ATOMS OF TYPE j PER UNIT VOLUME

b_j: COHERENT SCATTERING "LENGTH" OF ATOM j

$(b = Re\,b + i\,Im\,b)$

ρ = "SCATTERING LENGTH DENSITY" (SLD)

IN VACUUM:

$$E_0 = \frac{\hbar^2 k_0^2}{2m} + 0$$

IN A MATERIAL MEDIUM:

$$E = \frac{\hbar^2 k^2}{2m} + \frac{2\pi\hbar^2}{m}\rho$$

CONSERVATION OF ENERGY REQUIRES $E_0 = E$

$$\therefore \quad k^2 = k_0^2 - 4\pi\rho$$

THUS

$$\left[\nabla^2 + k^2\right]\Psi = 0$$

NOTE REFRACTIVE INDEX $n \equiv \frac{k}{k_0}$:

$$n^2 = 1 - \frac{4\pi\rho}{k_0^2}$$

REFLECTION FROM AN IDEAL FILM OR SLAB OF MATERIAL

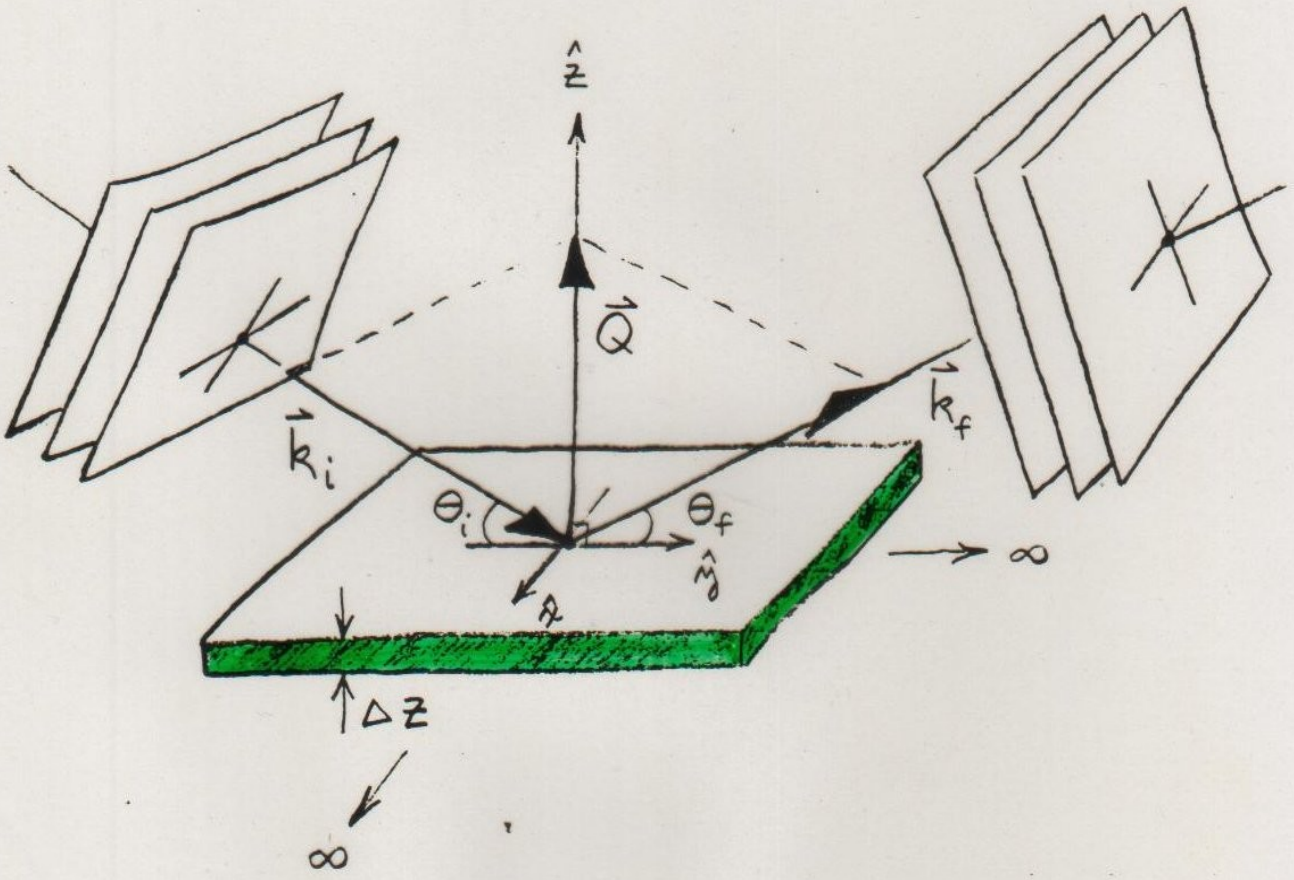

WAVEVECTOR TRANSFER $\vec{Q} = \vec{k}_f - \vec{k}_i$

$\rho = \rho(z)$ ONLY

EXPANDING $k^2 = k_0^2 - 4\pi\rho$,

$$k_x^2 + k_y^2 + k_z^2 + 4\pi\rho = k_{ox}^2 + k_{oy}^2 + k_{oz}^2.$$

NOW IF $\rho = \rho(z)$ ONLY, THEN

$\frac{\partial \rho}{\partial x}$ AND $\frac{\partial \rho}{\partial y}$, WHICH ARE PROPORTIONAL TO THE GRADIENTS OF THE POTENTIAL OR FORCES IN THE RESPECTIVE DIRECTIONS, ARE EQUAL TO ZERO. THUS, NO FORCE ACTS ALONG THESE DIRECTIONS TO CHANGE k_x AND k_y. THEN

$k_x = k_{ox}$ AND $k_y = k_{oy}$ ARE "CONSTANTS OF THE MOTION".

SUBSTITUTING $\Psi(\vec{r}) = e^{ik_{ox}x} e^{ik_{oy}y} \psi(z)$

INTO $[\nabla^2 + k^2]\Psi = 0$ GIVES

$$\left[\frac{\partial^2}{\partial z^2} + k_z^2\right]\psi(z) = 0$$

AND ∴ $k_z^2 = k_{oz}^2 - 4\pi\rho(z)$.

BECAUSE THERE IS NO CHANGE IN THE POTENTIAL IN THE X- OR Y- DIRECTIONS, THERE CAN BE NO MOMENTUM CHANGE IN THESE DIRECTIONS EITHER

THE IDEAL SLAB GEOMETRY WITH $\rho = \rho(z)$ ONLY GIVES RISE TO THE COHERENT "SPECULAR" REFLECTION OF A PLANE WAVE WHICH IS DESCRIBED BY A ONE-DIMENSIONAL WAVE EQUATION :

$$\left[\frac{\partial^2}{\partial z^2} + k_{oz}^2 - 4\pi\rho(z)\right]\psi_{(z)} = 0$$

IN THIS CASE $\theta_i = \theta_f \equiv \theta$,

$|\vec{k}_i| = |\vec{k}_f|$ AND $Q = 2k\sin\theta$

$= 2k_z$

ALSO, $n_z^2 \equiv 1 - \frac{4\pi\rho(z)}{k_{oz}^2}$

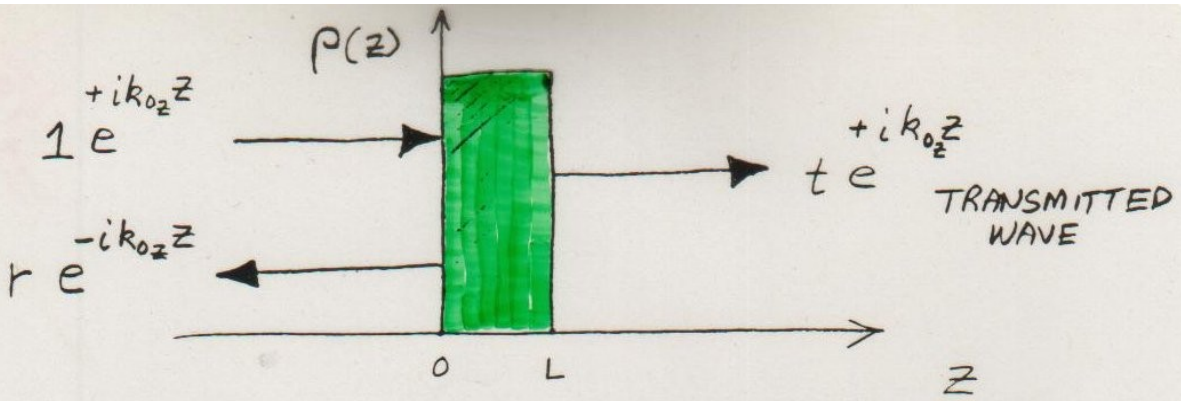

$$Q = 2k_{0z}$$

FROM THE WAVE EQUATION, IT IS POSSIBLE TO FIND A SOLUTION FOR THE REFLECTION AMPLITUDE IN INTEGRAL FORM (SEE ARTICLE PAGES):

$$r(Q) = \frac{4\pi}{iQ} \int_{-\infty}^{+\infty} \psi_{(z)}\, \rho(z)\, e^{+ik_{0z}z}\, dz$$

WHAT IS LOCALIZED AT z IN THE SLD PROFILE $\rho(z)$ IN "REAL" SPACE, IS DISTRIBUTED OVER THE REFLECTION AMPLITUDE $r(Q)$ IN THE RELATED SCATTERING OR "RECIPROCAL" SPACE

$$M_j = \begin{bmatrix} \cos\delta_j & \frac{1}{n_{x_j}}\sin\delta_j \\ -n_{x_j}\sin\delta_j & \cos\delta_j \end{bmatrix} \tag{11}$$

with $\delta_j = k_{ox}n_{xj}\Delta_j$, with n_{sx} and n_{ox} corresponding to the substrate and incident medium, respectively. The jth matrix M_j corresponds to the jth slab of thickness Δ_j wherein the scattering density is assumed to be constant and equal to ρ_j. The amplitude of the incident wave is assumed to be unity. The transmission and reflectivity are $T^*T = |T|^2$ and $R^*R = |R|^2$, respectively, and can be obtained directly from Equation (9).

Thus, for a given model potential, it is straightforward to calculate the expected reflectivity. Unfortunately, the converse of this statement is not necessarily true, as will be discussed in more detail in Section 4.

At this point it is useful to consider an alternate derivation of the reflectivity from which the Born approximation (corresponding to the kinematic limit which is discussed below) and other useful results can be directly obtained. Suppose that there exist two arbitrary but different density profiles $\rho_1(x)$ and $\rho_2(x)$ for which the corresponding, separate reflectivities are to be calculated. In each case we take the incident wave to propagate from left to right. We then have to solve the following pair of equations (derived from equations 6 and 7):

$$\psi_j''(x) + [k_{o_x}^2 - 4\pi\rho_j(x)]\,\psi_j(x) = 0 \qquad j = 1,2 \tag{12}$$

for $-\infty < x < \infty$ where $\psi_1(x)$ and $\psi_2(x)$ are the exact solutions in each case. From these we can construct the Wronskian function

$$W(x) \equiv W[\psi_1(x), \psi_2(x)] = \psi_1(x)\psi_2'(x) - \psi_1'(x)\psi_2(x). \tag{13}$$

Differentiating both sides of eq. (13) and using eq. (12) we obtain

$$W'(x) = -\psi_1(x)4\pi\rho_{12}(x)\psi_2(x) \tag{14}$$

where

$$\rho_{12}(x) \equiv \rho_1(x) - \rho_2(x) \tag{15}$$

Equation (14) tells us that W(x) is a constant over intervals where the two density profiles coincide, $\rho_1(x) = \rho_2(x)$, which is a property we will exploit to obtain a formula relating the reflectivities for each profile. First, assume that $\rho_1 \neq \rho_2(x)$ only within an interval $\ell_1 < x < \ell_2$. We allow subintervals of (ℓ_1, ℓ_2) where $\rho_1(x) = \rho_2(x)$, but we demand finite ℓ_1 and ℓ_2 such that $\rho_1(x) = \rho_2(x)$ for all $x < \ell_1$ and for all $x > \ell_2$. We also assume that the wave is incident in vacuum so for $x < \ell_1$, $\rho_1(x) = \rho_2(x) = 0$. The wavefunctions for $x < \ell_1$ are then

$$\psi_j(x) = e^{ik_{o_x}x} + R_j e^{-ik_{o_x}x} \tag{16}$$

where R_1 and R_2 are the reflection amplitudes for each problem. Similarly, we assume that each density profile has a common substrate so that for $x > \ell_2$, $\rho_1(x) = \rho_2(x) = \rho(\infty)$. The wavefunctions for $x > \ell_2$ are then

$$\psi_j(x) = T_j\, e^{iKx} \tag{17}$$

where

$$K = \sqrt{k_{o_x}^2 - 4\pi\rho(\infty)} \tag{18}$$

and T_1 and T_2 are the transmission amplitudes in each problem. Now we see that for the given pair of profile functions $\rho_1(x)$ and $\rho_2(x)$, $W(x)$ is uniquely determined everywhere and varies with x only in (ℓ_1, ℓ_2), where $\rho_1(x)$ and $\rho_2(x)$ can differ. Substituting (17) into (13) we obtain

$$W(x) = 0 \tag{19}$$

for all $x \geq \ell_2$, since $\psi_1(x)$ and $\psi_2(x)$ are proportional to one another (linearly dependent) in this region. However, substituting (16) into (13) we get

$$W(x) = 2ik_{o_x}(R_1 - R_2) \tag{20}$$

for all $x \leq \ell_1$, which is a complex constant. Finally, for $\ell_1 < x < \ell_2$ we integrate both sides of equation (14) to obtain

$$\int_{\ell_1}^{\ell_2} W'(x)dx = W(\ell_2) - W(\ell_1) = -\alpha_{12} \tag{21}$$

where

$$\alpha_{12} = \int_{\ell_1}^{\ell_2} \psi_1(x) 4\pi\rho_{12}(x)\psi_2(x)dx \quad . \tag{22}$$

Now $W(x)$ is continuous everywhere since $\psi_j(x)$ and $\psi_j'(x)$ are. Thus, evaluating (19) and (20) at $x = \ell_2$ and $x = \ell_1$, respectively, we find $W(\ell_2) = 0$ and $W(\ell_1) = 2ik_{ox}(R_1 - R_2)$. Thus, from equation (21) we get

$$R_1 = R_2 + \frac{\alpha_{12}}{iQ} \tag{23}$$

where again $Q = 2k_{ox}$ is the wavevector transfer. Equation (23) is the general formula we set out to derive and is a handy starting point for exact treatments as well as approximation schemes.

For example, consider any $\rho(x)$ which vanishes identically for $x < \ell_1$ and for $x > \ell_2$. Then, in equation (23) we can set $\rho_1(x) = \rho(x)$, $\psi_1(x) = \psi(x)$, and $R_1 = R$ whereas for the "other" density profile we take $\rho_2(x) = 0$ everywhere so that $\psi_2(x) = \exp(ik_{ox}x)$ and $R_2 = 0$. Combining equations (22) and (23) then gives the <u>exact</u> solution of the reflectivity for an arbitrary scattering density profile $\rho(x)$:

$$R = \frac{4\pi}{iQ} \int_{-\infty}^{+\infty} \psi(x)\rho(x)e^{ik_{o_x}x}dx \tag{24}$$

where we have formally extended the integration over all x, though only the region where $\rho(x) \neq 0$ contributes. Although it may not be obvious from the derivation, equation (24) also holds if we allow $\rho(x)$ to be nonzero as $x \to \infty$, as long as the integral exists. Note that (24) requires, to be exact, the exact wavefunction $\psi(x)$ wherever $\rho(x) \neq 0$. The corresponding expression for the reflectivity $|R|^2$, is

$\psi(z)$ INSIDE THE MEDIUM IS GENERALLY UNKNOWN:

BORN APPROXIMATION REPLACES $\psi(z)$ WITH THE INCIDENT WAVE FUNCTION $e^{+ik_{oz}z}$ BASED ON THE ASSUMPTION THAT $\psi(z)$ IS NOT SIGNIFICANTLY DISTORTED FROM THE FREE SPACE FORM (WEAK INTERACTION): THEN

FOURIER TRANSFORM

$$r(Q) \simeq \frac{4\pi}{iQ} \int_{-\infty}^{+\infty} \rho(z)\, e^{iQz}\, dz$$

FOR A REAL POTENTIAL $\rho(z)$

$$\mathrm{Re}\; r(Q) \simeq \frac{4\pi}{Q} \int_{-\infty}^{+\infty} \rho(z) \sin(Qz)\, dz$$

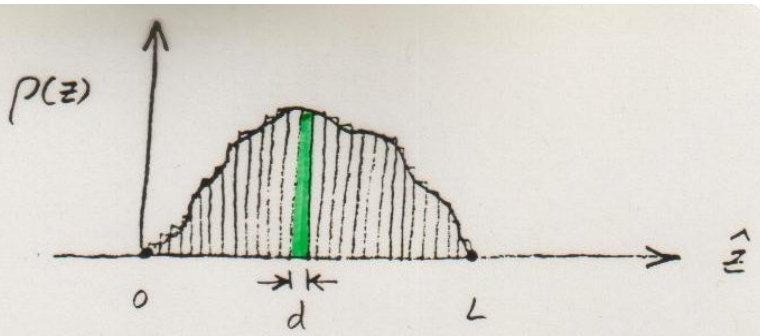

ARBITRARY POTENTIAL DIVIDED INTO RECTANGULAR SLABS OF WIDTH d AND CONSTANT ρ

THEN

(BORN APPROX.)

$$\mathrm{Re}\, r(Q) \simeq \frac{4\pi}{Q} \int_0^L \rho(z) \sin(Qz)\, dz$$

BECOMES

$$\mathrm{Re}\, r(Q_j) \simeq \frac{4\pi}{Q_j} \sum_{\ell=1}^{N} \int_{(\ell-1)d}^{\ell d} \rho_\ell \sin(Q_j z)\, dz$$

$$= -\frac{4\pi}{Q_j^2} \sum_{\ell=1}^{N} \rho_\ell \left[\cos(Q_j z)\right]_{(\ell-1)d}^{\ell d}$$

SET OF $\mathrm{Re}\, r$ FOR DIFFERENT VALUES OF Q OR θ

$$\mathrm{Re}\, r_1 = C_{11}\rho_1 + C_{12}\rho_2 + \cdots + C_{1N}\rho_N$$
$$\mathrm{Re}\, r_2 = C_{21}\rho_1 + C_{22}\rho_2 + \cdots + C_{2N}\rho_N$$
$$\vdots$$
$$\mathrm{Re}\, r_N = C_{N1}\rho_1 + C_{N2}\rho_2 + \cdots + C_{NN}\rho_N$$

SOLVE SIMULTANEOUS EQUATIONS FOR ρ's GIVEN $\mathrm{Re}\, r$'s

e.g., SVD, EIGENVALUE PROBLEM FORMULATION, ...

$$\underbrace{\mathrm{Re}\; r_{BA}(Q)\left[\frac{Q^2}{8\pi \sin\left(\frac{Qd}{2}\right)}\right]}_{\equiv \mathcal{I}(Q)} = \sum_{j=1}^{N} \rho_j \sin\left[\frac{(2j-1)Qd}{2}\right]$$

$$\int_0^{\pi} \sin m\theta \sin n\theta \, d\theta = \begin{cases} 0 & m, n \text{ INTEGERS}, \; m \neq n \\ \frac{\pi}{2} & m, n \text{ INTEGERS}, \; m = n \end{cases}$$

ORTHOGONALITY

$$\rho_j = \frac{d}{4\pi^2} \int_0^{\frac{\pi}{d}} Q^2 \, \mathrm{Re}\, r_{BA}(Q) \frac{\sin\left[\frac{(2j-1)Qd}{2}\right]}{\sin\left(\frac{Qd}{2}\right)} \, dQ$$

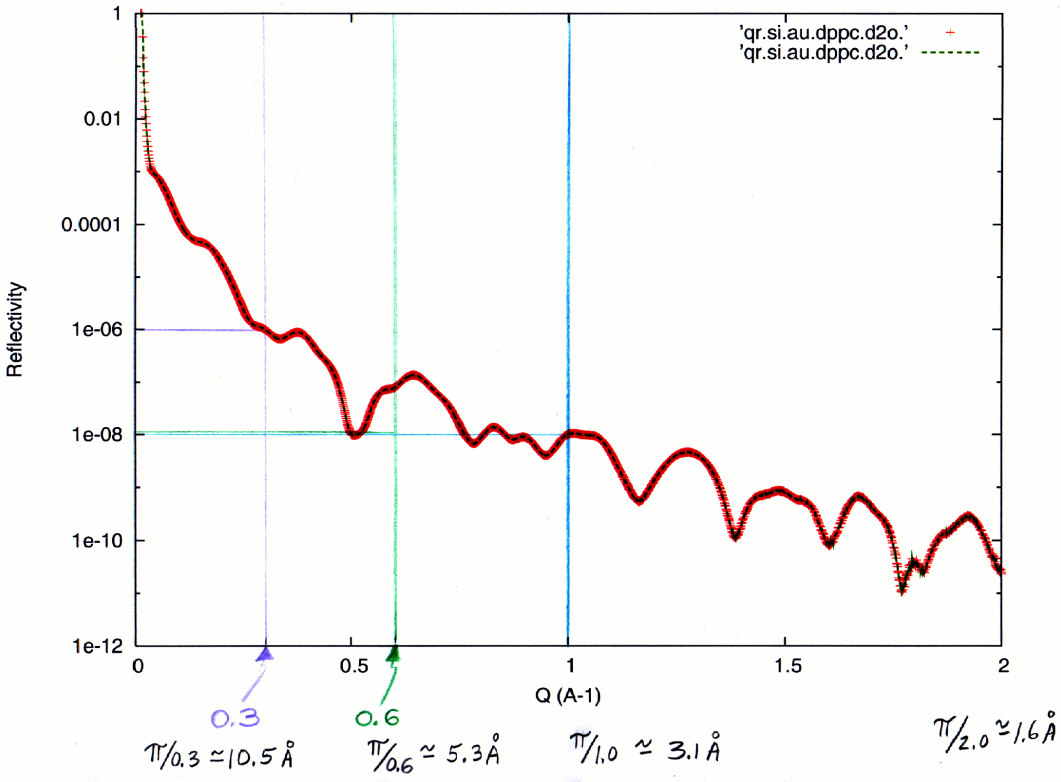
'qr.si.au.dppc.d2o.'
'qr.si.au.dppc.d2o.'
Reflectivity
1
0.01
0.0001
1e-06
1e-08
1e-10
1e-12
0
0.5
1
1.5
2
Q (A-1)
0.3
0.6
π/0.3 ≃ 10.5 Å
π/0.6 ≃ 5.3 Å
π/1.0 ≃ 3.1 Å
π/2.0 ≃ 1.6 Å

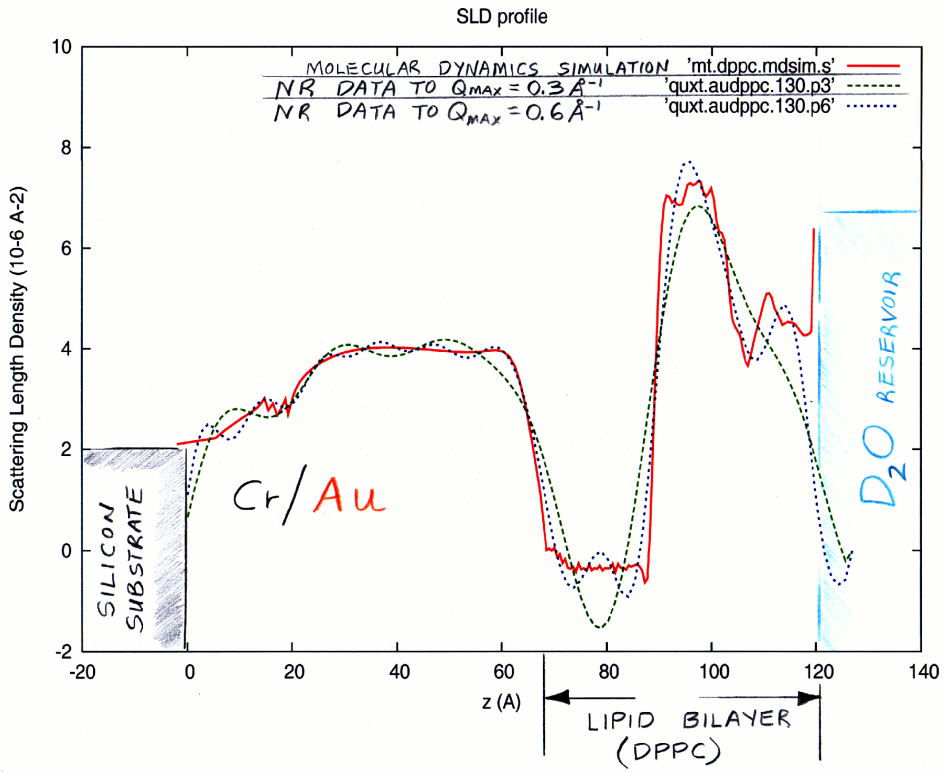
SLD profile
MOLECULAR DYNAMICS SIMULATION 'mt.dppc.mdsim.s'
NR DATA TO QMAX = 0.3 Å-1 'quxt.audppc.130.p3'
NR DATA TO QMAX = 0.6 Å-1 'quxt.audppc.130.p6'
Scattering Length Density (10-6 A-2)
10
8
6
4
2
0
-2
-20
0
20
40
60
80
100
120
140
z (A)
SILICON SUBSTRATE
Cr/Au
D2O RESERVOIR
LIPID BILAYER
(DPPC)

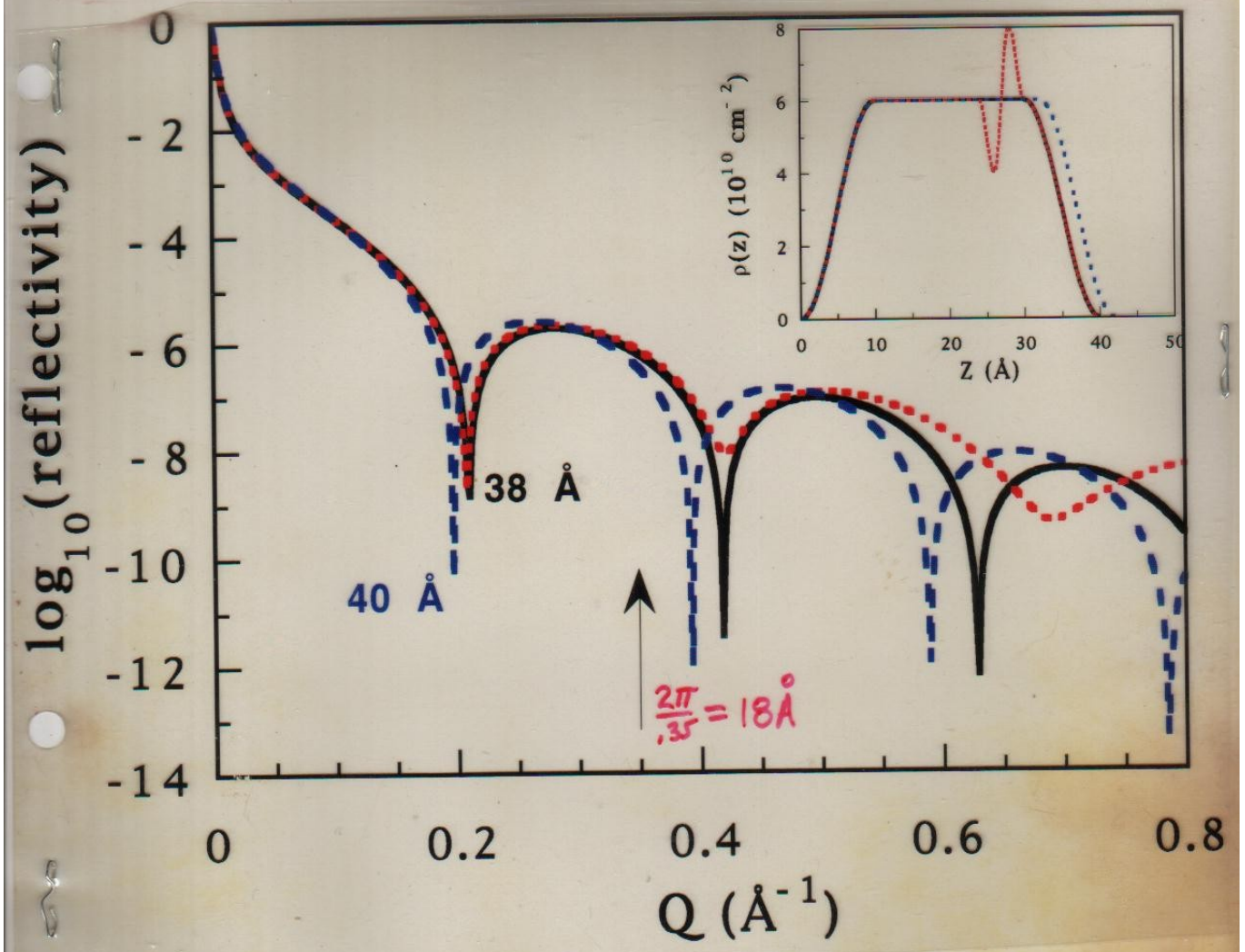

Solid, long-dash, and short-dash neutron reflectivity curves corresponding to their respective scattering length density profiles shown in the inset. This series of curves and profiles illustrates the sensitivity of the reflectivity to the overall film thickness at reflectivities approaching 10-7 whereas detailed features such as the oscillation in the long-dash profile can only be accurately discerned at reflectivities an order of magnitude or so lower, at Q-values corresponding to 2 pi/ width of the feature.

"REFLECTIVITY" REGIME

CRYSTAL "DIFFRACTION" REGIME

LOW Q : HIGHER SENSITIVITY FOR COMPOSITION PROFILE

HIGH Q : HIGHER SENSITIVITY FOR STRAIN OR SPACING LATTICE PROFILE

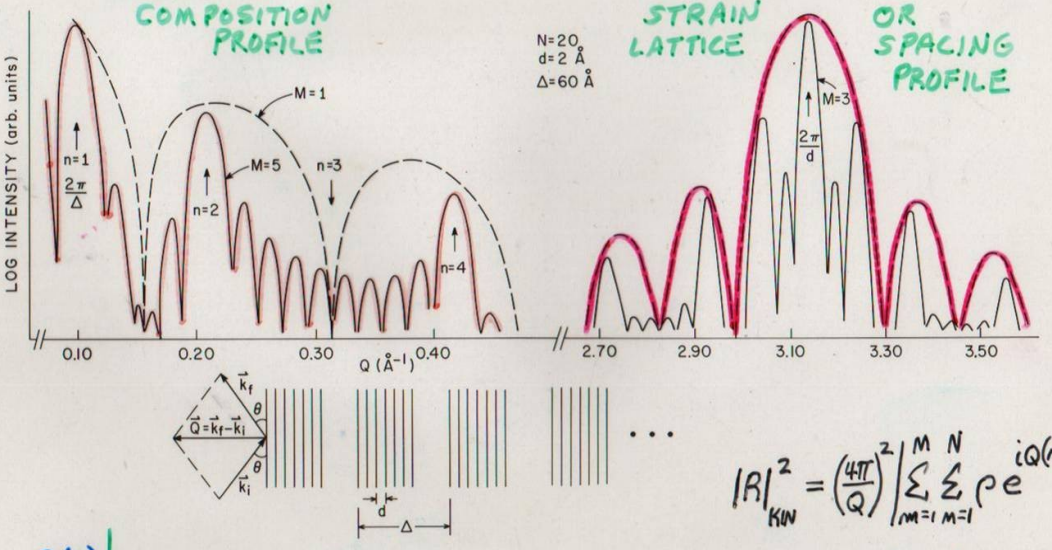

$$|R|^2_{KIN} = \left(\frac{4\pi}{Q}\right)^2 \left| \sum_{m=1}^{M} \sum_{n=1}^{N} \rho e^{iQ(nd+m\Delta)} \right|^2$$

$$= \left(\frac{4\pi}{Q}\right)^2 \rho^2 \left| \frac{\sin(NQd/2)}{\sin(Qd/2)} \right|^2 \left| \frac{\sin(MQ\Delta/2)}{\sin(Q\Delta/2)} \right|^2$$

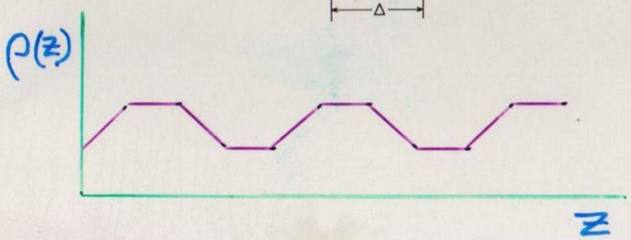

PROBLEM: BORN APPROXIMATION FAILS AT SUFFICIENTLY SMALL Q — MUST THEN USE EXACT THEORY

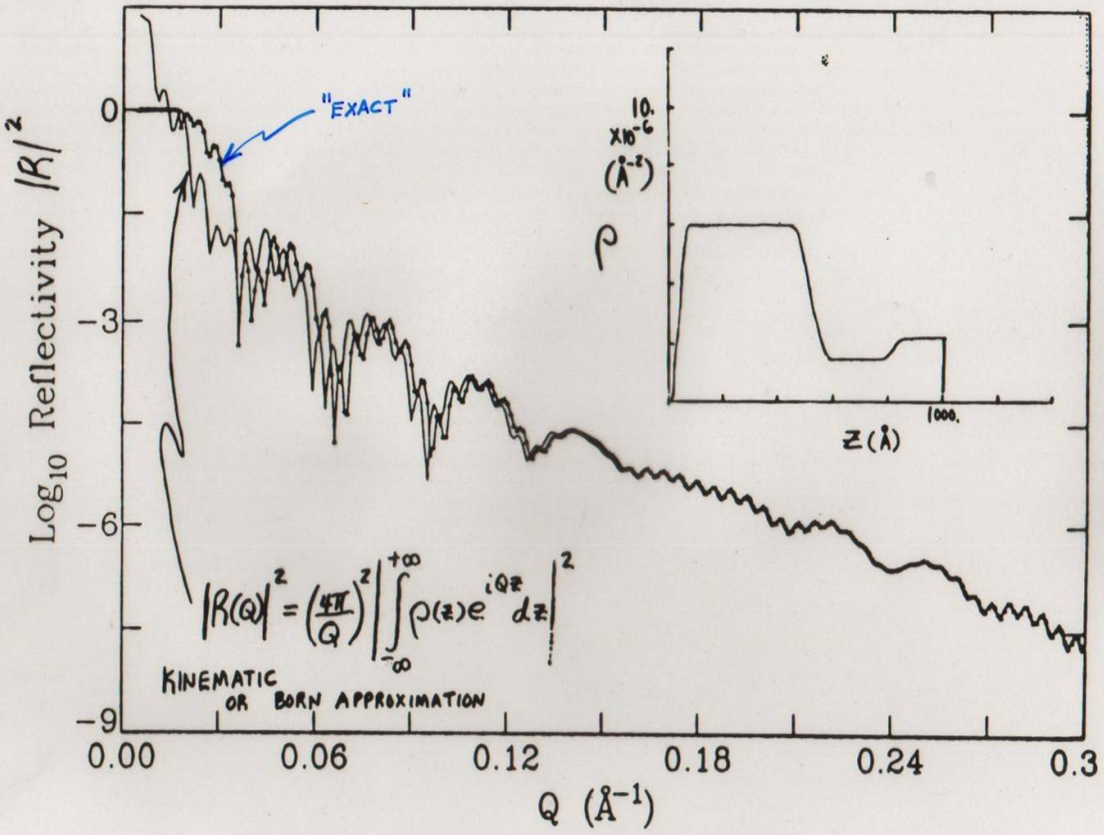

Fig.

Comparison between kinematic (line) and dynamic (triangle + line) plus-state reflectivities for a density profile similar to that of Fig.2 as described in the text.

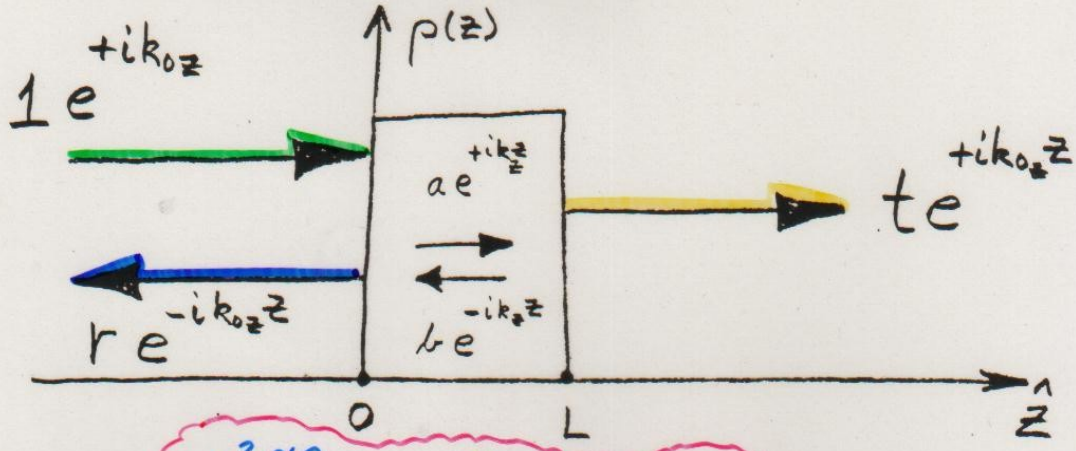

$$\frac{\partial^2 \psi(z)}{\partial z^2} + k_z^2 \psi(z) = 0$$

CONSERVATION OF MOMENTUM AND PARTICLE NUMBER REQUIRE THAT $\frac{\partial \psi(z)}{\partial z}$ AND $\psi(z)$ BE CONTINUOUS AT THE BOUNDARIES $z=0$ & $z=L$

$$\begin{pmatrix} t \\ it \end{pmatrix} e^{ik_{0z}L} = \begin{pmatrix} A & B \\ C & D \end{pmatrix} \begin{pmatrix} 1+r \\ i(1-r) \end{pmatrix}$$

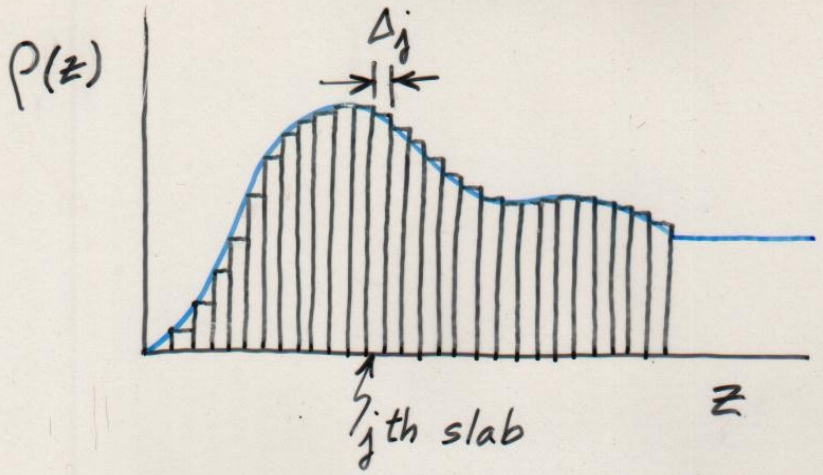

$$\begin{pmatrix} A & B \\ C & D \end{pmatrix} = \begin{pmatrix} a_N & b_N \\ c_N & d_N \end{pmatrix} \begin{pmatrix} a_{N-1} & b_{N-1} \\ c_{N-1} & d_{N-1} \end{pmatrix} \cdots \begin{pmatrix} a_2 & b_2 \\ c_2 & d_2 \end{pmatrix} \begin{pmatrix} a_1 & b_1 \\ c_1 & d_1 \end{pmatrix}$$

$$\begin{pmatrix} a_j & b_j \\ c_j & d_j \end{pmatrix} = \begin{pmatrix} \cos\delta_j & \frac{1}{n_{z_j}} \sin\delta_j \\ -n_{z_j} \sin\delta_j & \cos\delta_j \end{pmatrix}$$

$$\delta_j = k_{0z} n_{z_j} \Delta_j$$
$$= k_{z_j} \Delta_j$$

free film

Then, once we know $\mathbf{M}_k(L)$*:*

$z=L$ $\qquad\qquad$ $z=0$

$$\begin{pmatrix}1\\ \mathrm{i}\end{pmatrix} t(k)\mathrm{e}^{\mathrm{i}kL} = \begin{pmatrix}A_k(L) & B_k(L)\\ C_k(L) & D_k(L)\end{pmatrix}\begin{pmatrix}1+r(k)\\ \mathrm{i}[1-r(k)]\end{pmatrix}$$

$$\boxed{r = \frac{B+C+\mathrm{i}(D-A)}{B-C+\mathrm{i}(D+A)}}$$

$$t = \frac{2\mathrm{i}\mathrm{e}^{-\mathrm{i}kL}}{B-C+\mathrm{i}(D+A)}$$

$$R = |r|^2 = \frac{\Sigma-2}{\Sigma+2}, \quad \Sigma = \mathrm{A}^2 + \mathrm{B}^2 + \mathrm{C}^2 + \mathrm{D}^2$$

Fresnel Reflectivity

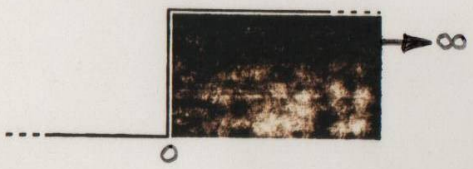

$$|r_F|^2 \equiv R_F(Q_z) = \frac{1-\sqrt{1-\frac{Q_{zc}^2}{Q^2}}}{1+\sqrt{1-\frac{Q_{zc}^2}{Q^2}}}$$

For $Q_z < Q_{zc}$, $R_F = 1$.

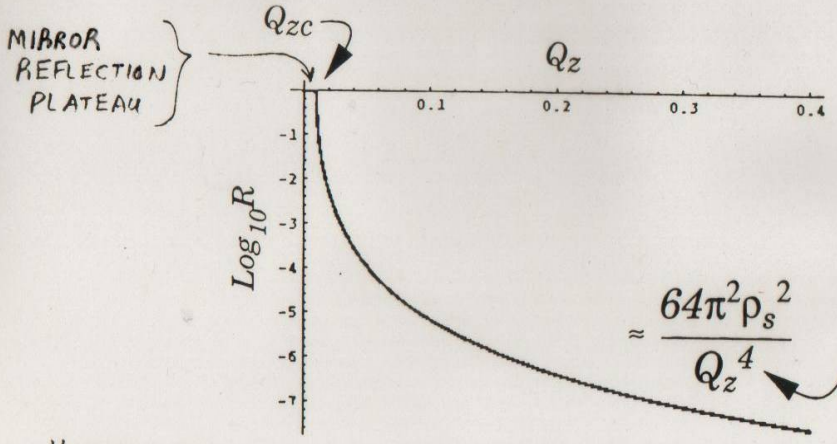

$$\approx \frac{64\pi^2\rho_s^2}{Q_z^4}$$

Analogue of SANS Porod's Law: effect of sharp edges.

"CRITICAL Q"

$Q_c^2 = 16\pi\rho$

(N.F. BERK)

"Soft" substrate

Smooth transition:
interlayer diffusion
roughness

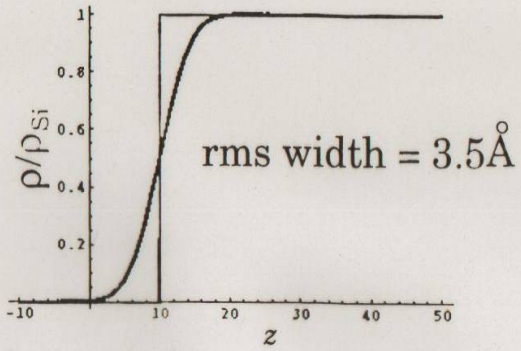

rms width = 3.5Å

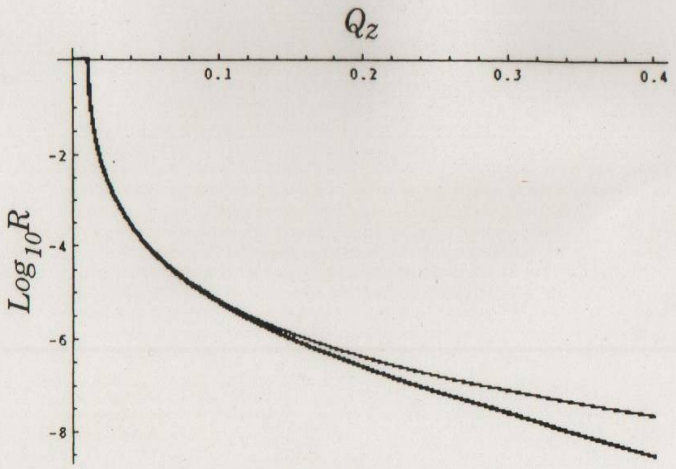

(N.F. BERK)

Uniform slab

$\rho = 2.07\ 10^{-6}\text{Å}^{-2}$

$z=0$ $z=200\text{Å}$

$R(0) = 1$

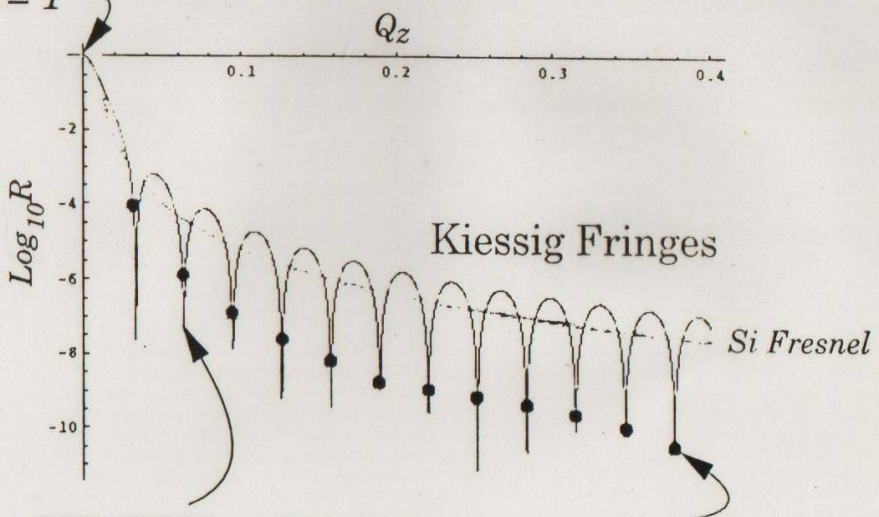

$\sqrt{Q_z^2 - 16\pi\rho} = \frac{2\pi}{L}\text{m=1,2,...}$

$\frac{2\pi}{L}\text{m=1,2,...}$

(Kinematical)

(N.F. BERK)

Multilayer on Si

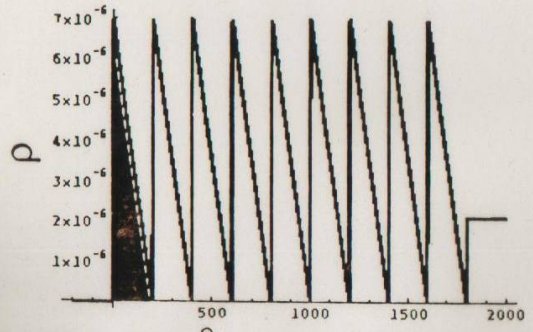

$D = 200\text{Å}$ $L = 9 \times 200\text{Å}$

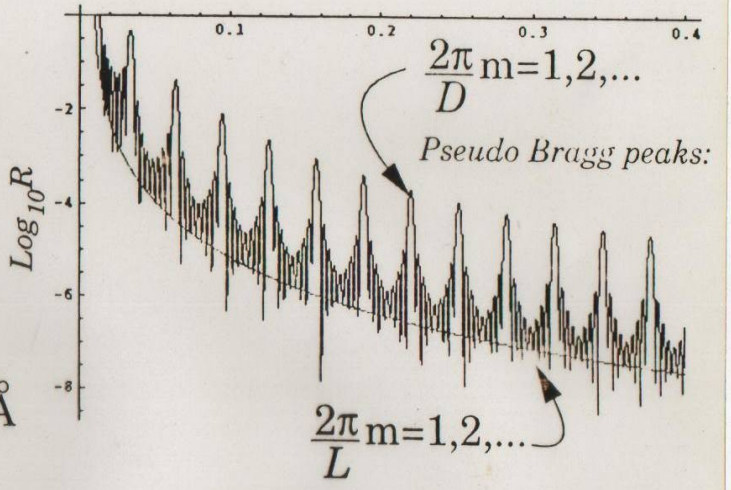

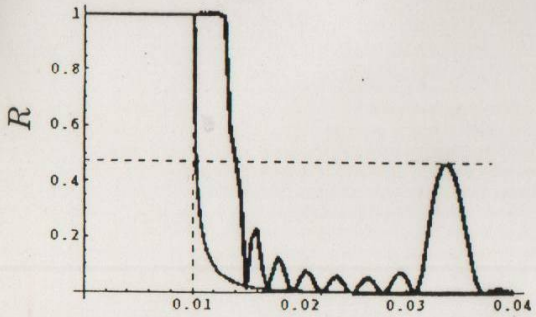

$L = 18 \times 200\text{Å}$

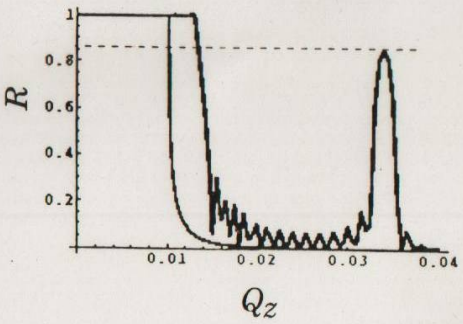

(N.F.BERK)

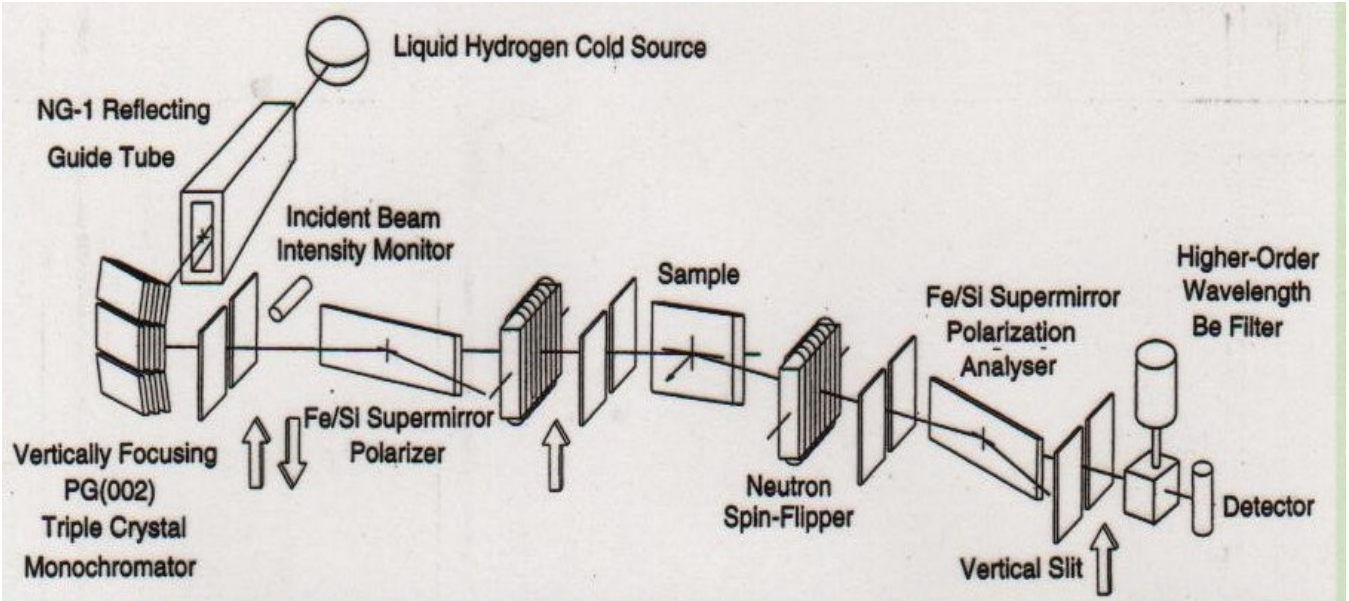
Liquid Hydrogen Cold Source
NG-1 Reflecting
Guide Tube
Incident Beam
Intensity Monitor
Sample
Higher-Order
Wavelength
Be Filter
Fe/Si Supermirror
Polarization
Analyser
Fe/Si Supermirror
Polarizer
Vertically Focusing
PG(002)
Triple Crystal
Monochromator
Neutron
Spin-Flipper
Detector
Vertical Slit

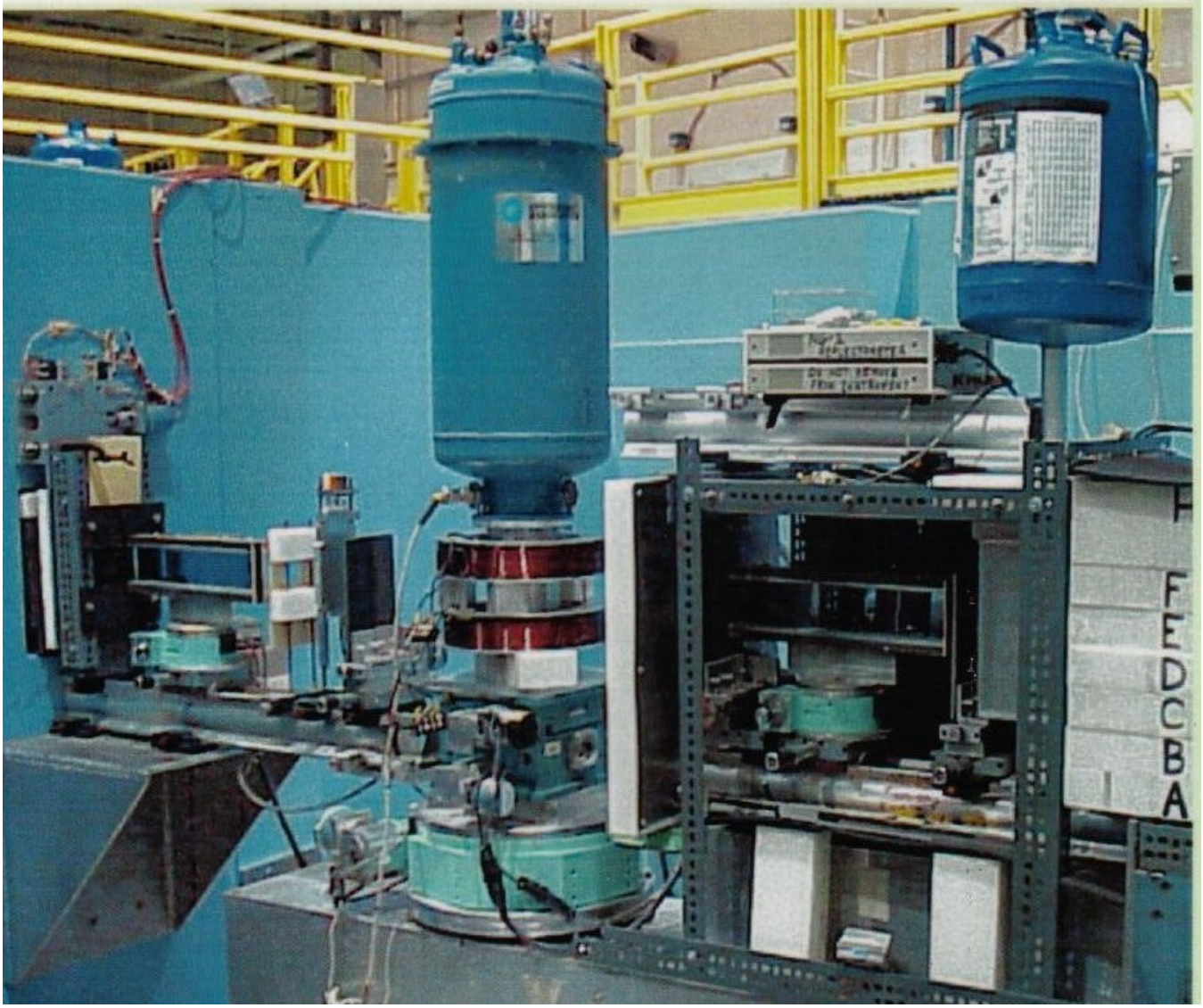
F
E
D
C
B
A

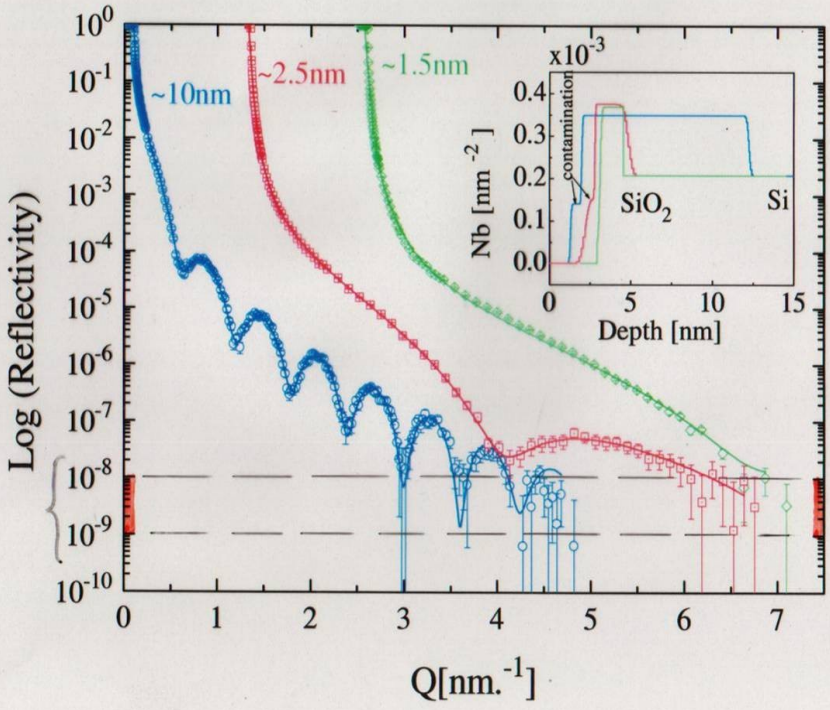
~10nm
~2.5nm
~1.5nm
Log (Reflectivity)
Q[nm.-1]
x10-3
Nb [nm-2]
contamination
SiO2
Si
Depth [nm]

J. DURA et al.

IF ρ IS NOT EXACTLY $\rho(z)$,
i.e., SOME VARIATIONS EXIST IN
THE (x,y)- PLANE, THEN

$$r_{BORN} \simeq \frac{4\pi}{iQ} \int_{-\infty}^{+\infty} \langle \rho(x,y,z) \rangle_{x,y} \, e^{iQz} \, dz$$

ON SPECULAR "RIDGE" WHERE $\vec{Q} = Q_z \hat{z}$

WHERE

$$\langle \rho(x,y,z) \rangle_{x,y} = \frac{1}{A} \iint_{-\infty -\infty}^{+\infty +\infty} \rho(x,y,z) \, dx dy$$

$$= \bar{\rho}(z) \text{ ONLY}$$

& $\bar{A}$ = NORMALIZING AREA OF THE (X,Y)- PLANE

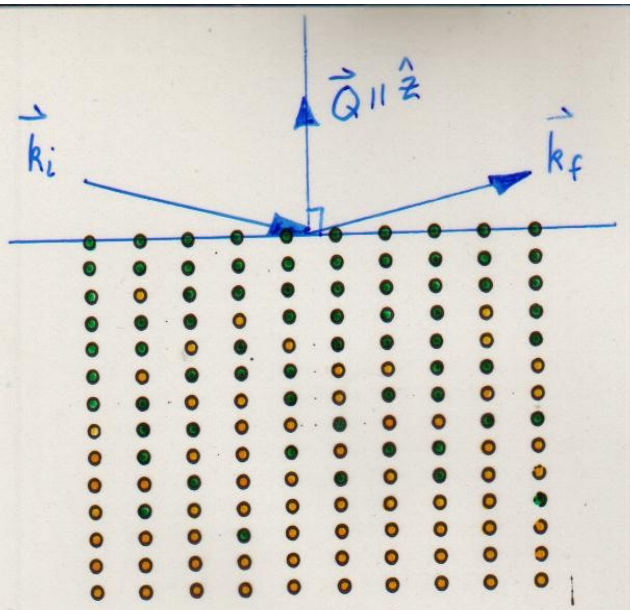

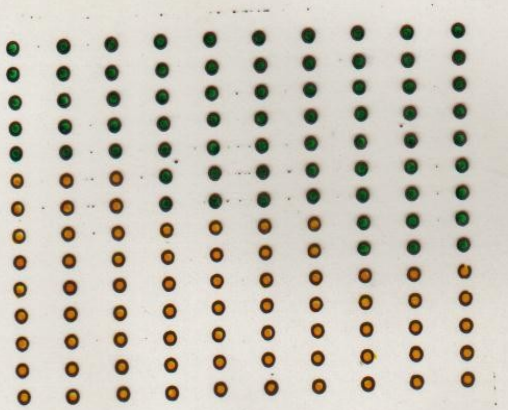

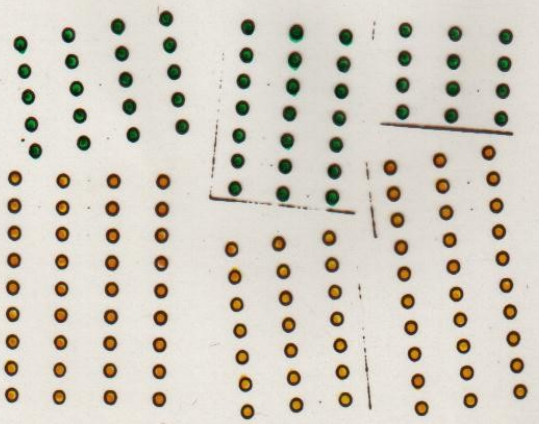

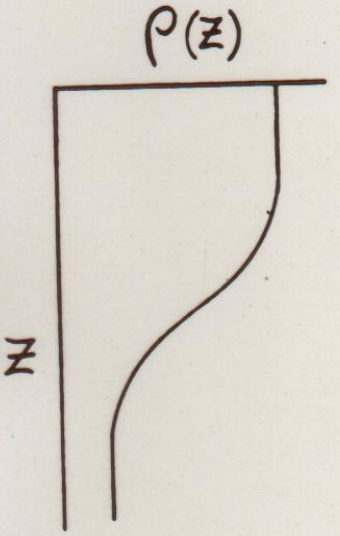

POSSIBLE MICROSTRUCTURES CORRESPONDING TO INTERFACIAL ROUGHNESS

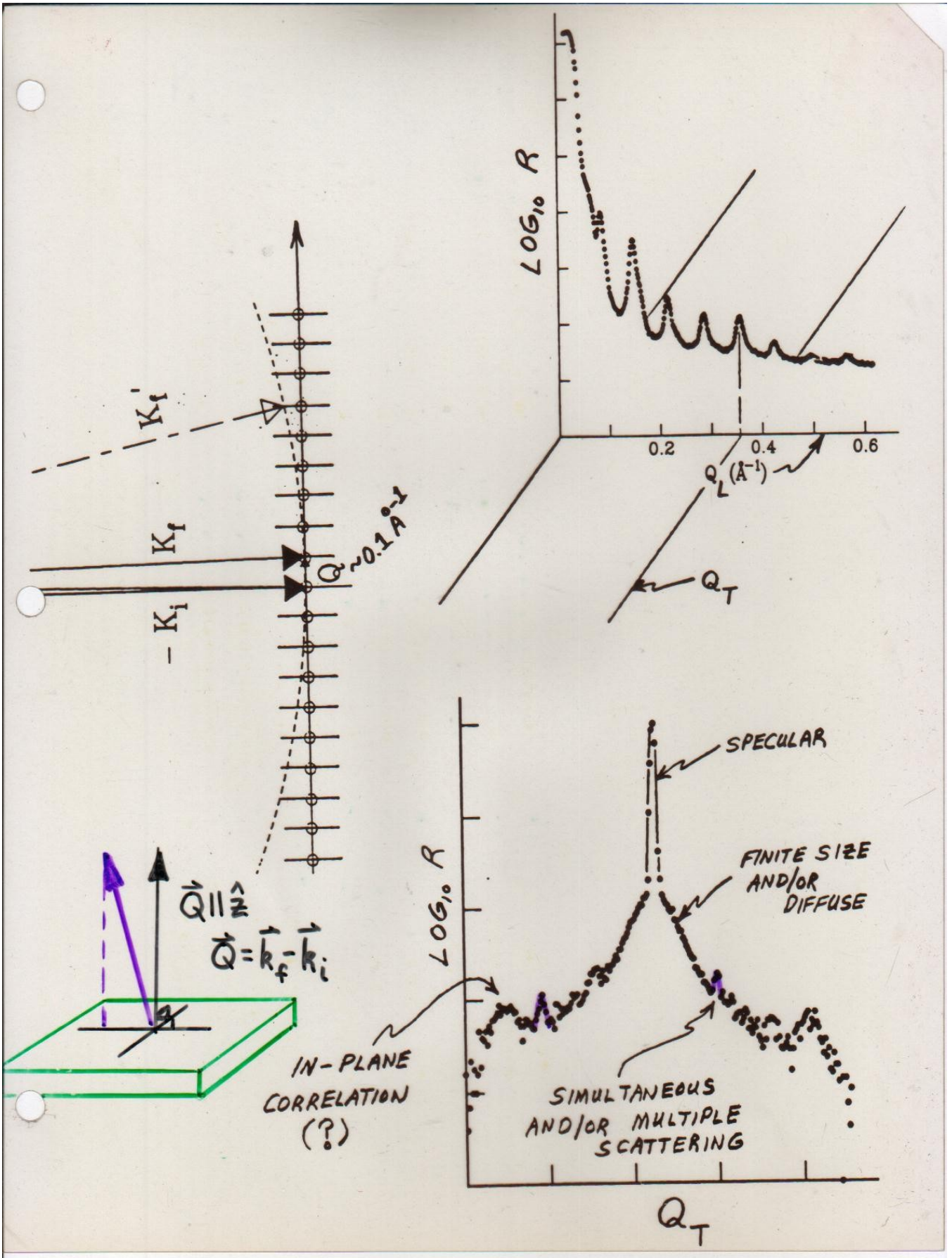
K_f'
K_f
$-K_i$
$Q \sim 0.1 \text{ Å}^{-1}$
$\vec{Q} \parallel \hat{z}$
$\vec{Q} = \vec{k}_f - \vec{k}_i$
LOG$_{10}$ R
0.2
0.4
0.6
Q_L (Å^{-1})
Q_T
SPECULAR
FINITE SIZE AND/OR DIFFUSE
IN-PLANE CORRELATION (?)
SIMULTANEOUS AND/OR MULTIPLE SCATTERING
Q_T

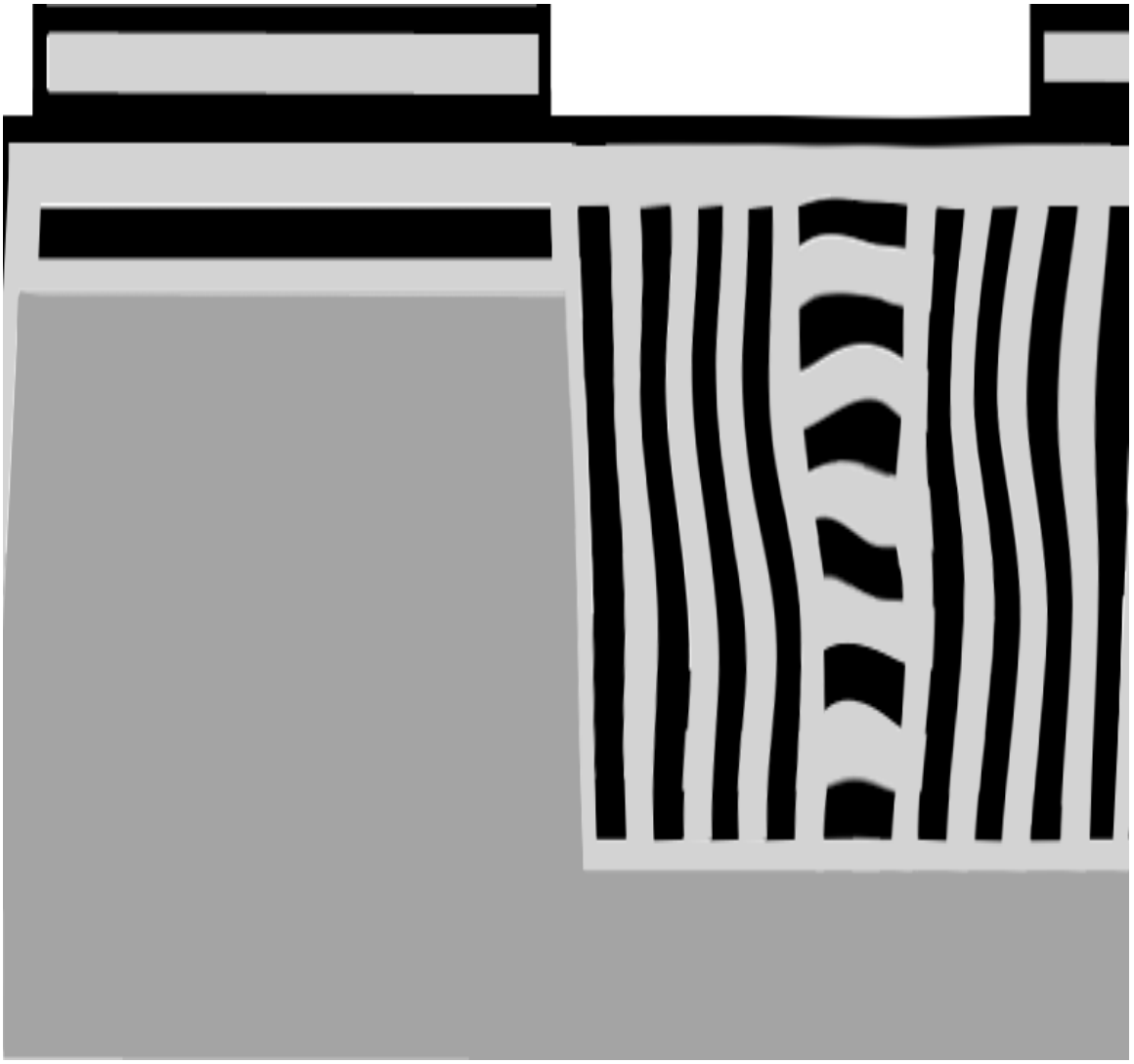

Fig 2. Diagram of expected orientation of lan
Silicon substrate with etched channels is disp
corresponding to the two polymer component

Diblock copolymer lamellar nanostructures – R.Jones, B.Berry, and K.Yager (NIST Polymer Division) and S.Satija, J.Dura, B.Maranville et al. (NCNR).

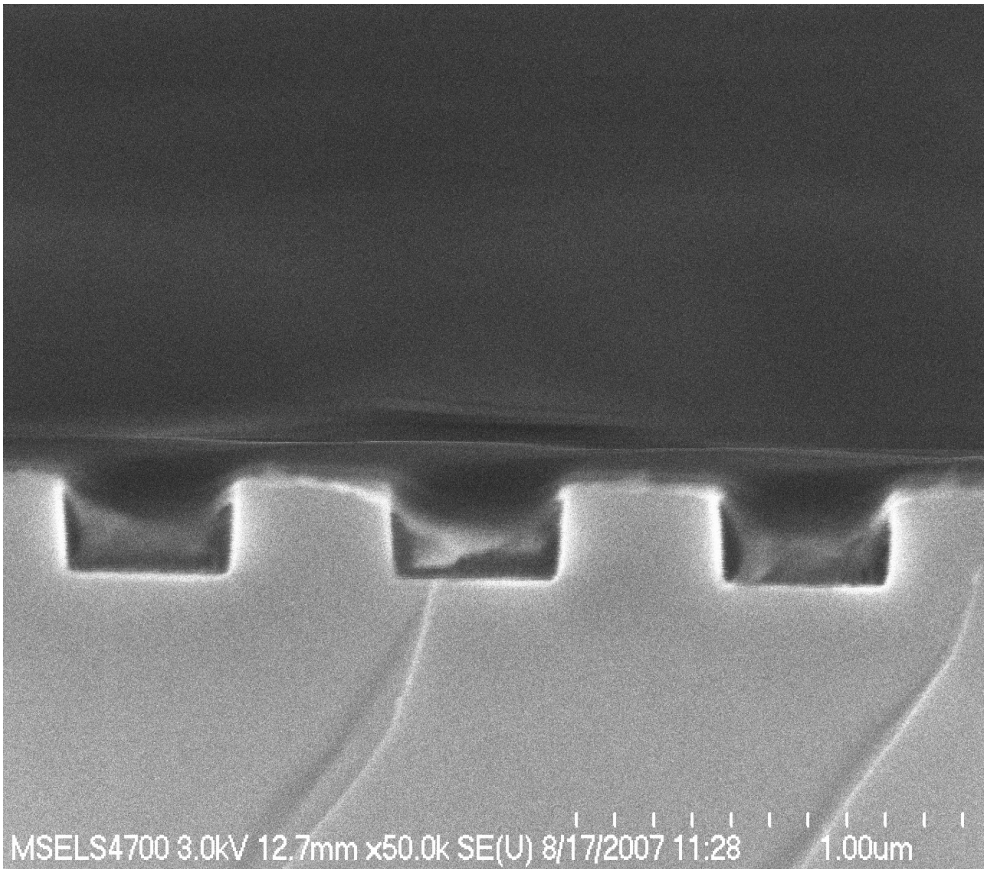

Fig 1. Side-view scanning-electron micrograph of laser-interfe
with 400 nm channels, spaced by 400 nm for a total repeat dis

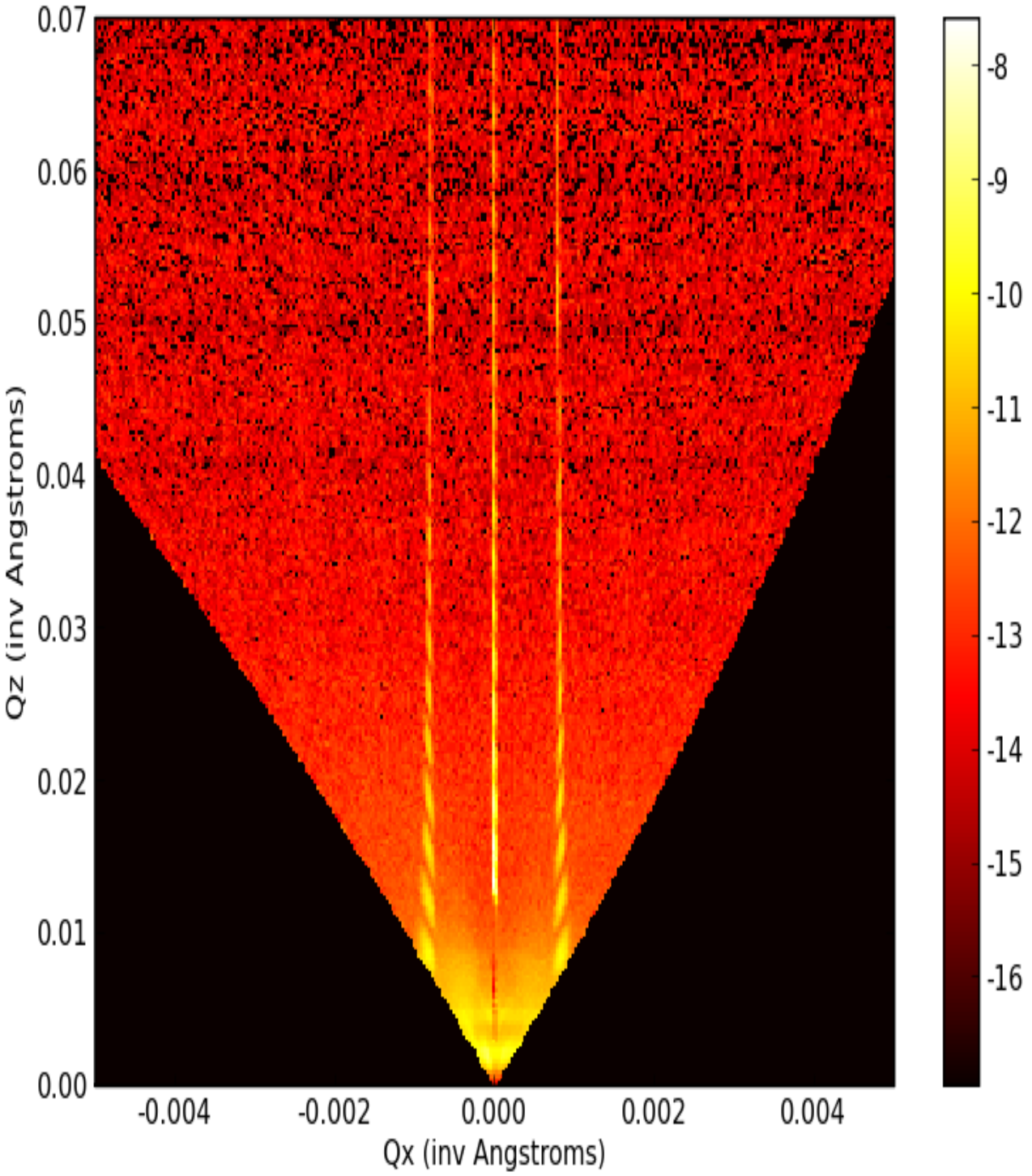

Neutron diffraction from silicon with channels but without polymer.

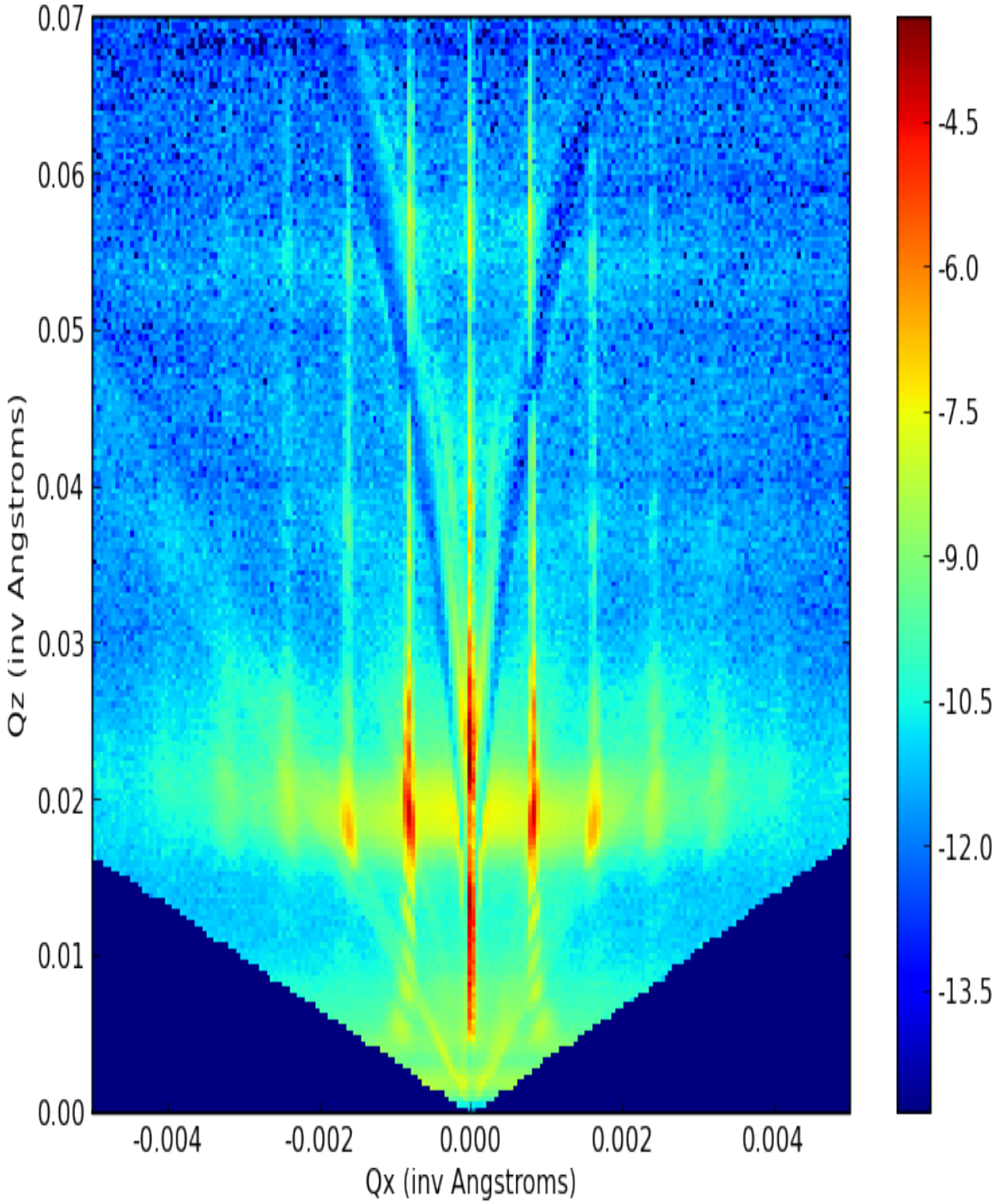

Neutron diffraction from Si channels filled with ordered diblock copolymer.

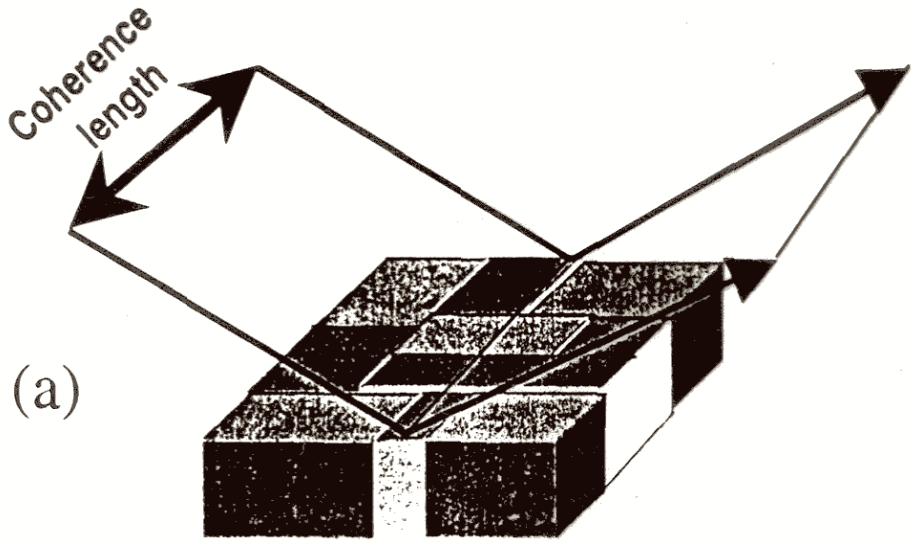

small-scale *heterogeneity* laterally averages SLD profile

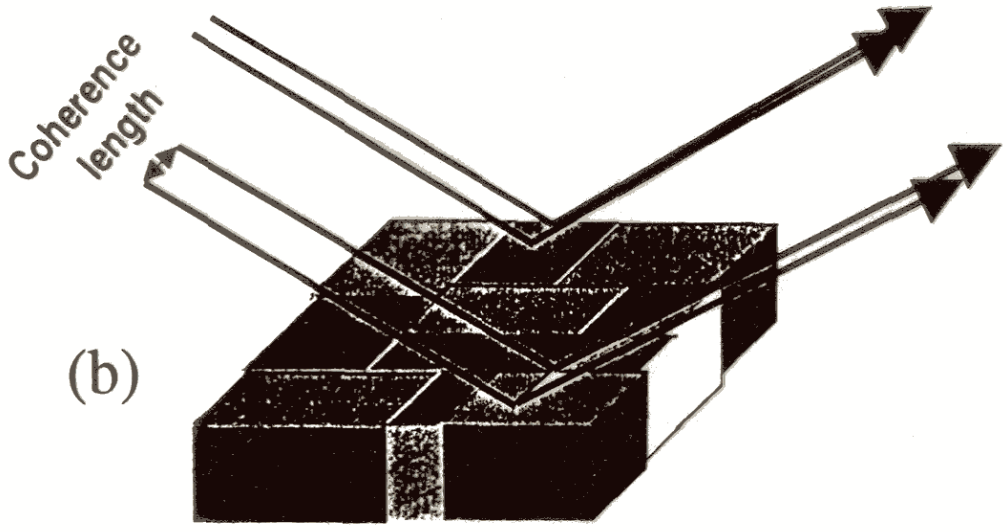

large-scale *heterogeneity* laterally averages reflectivity

$$Q = \frac{4\pi \sin\theta}{\lambda}$$

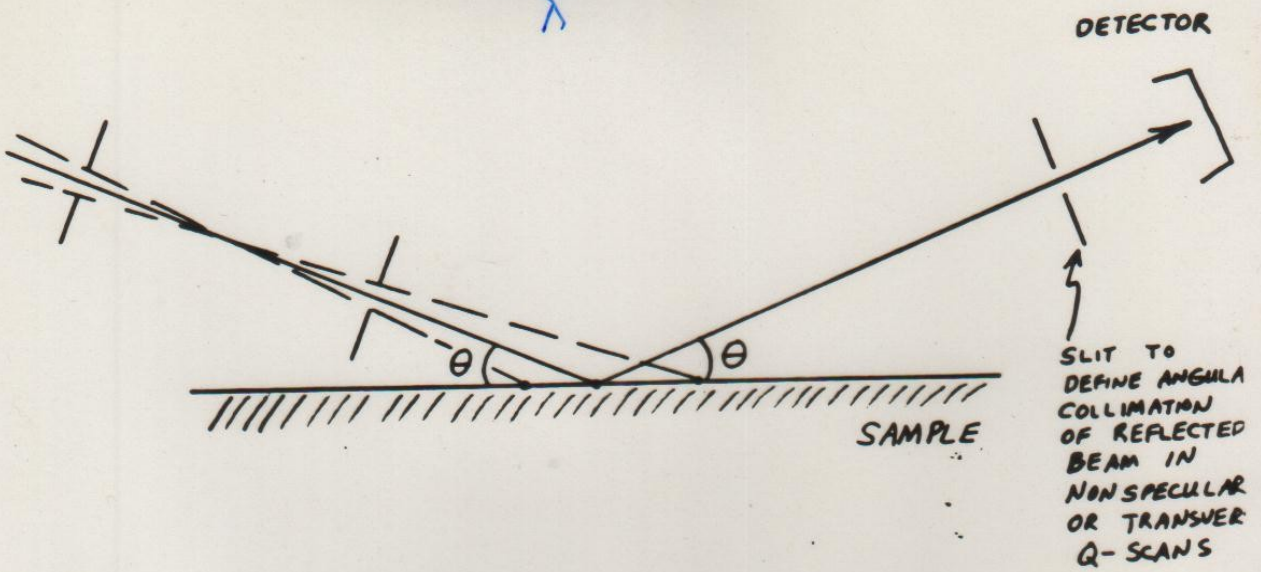

$$\Delta Q_{\text{LONGITUDINAL}} \simeq \frac{\Delta\lambda}{\lambda} Q + \sqrt{\left(\frac{4\pi}{\lambda}\right)^2 - Q^2}\ \Delta\theta$$

TYPICAL VALUES

$$\frac{\Delta\lambda}{\lambda} \simeq 0.01$$

$$\Delta\theta \simeq 1 \text{ min of arc}$$

KEEP $\dfrac{\Delta Q}{Q} \simeq$ CONSTANT

$$R_{OBS.}(Q_0) \simeq \left(\frac{0.9394}{\Gamma}\right) \int_{-\Gamma}^{+\Gamma} R_{ACT.}(Q)\, e^{-\left(\frac{2.7725}{\Gamma^2}\right)(Q-Q_0)^2}\, dQ$$

(ASSUMING A GAUSSIAN DISTRIBUTION OF Q-VALUES)

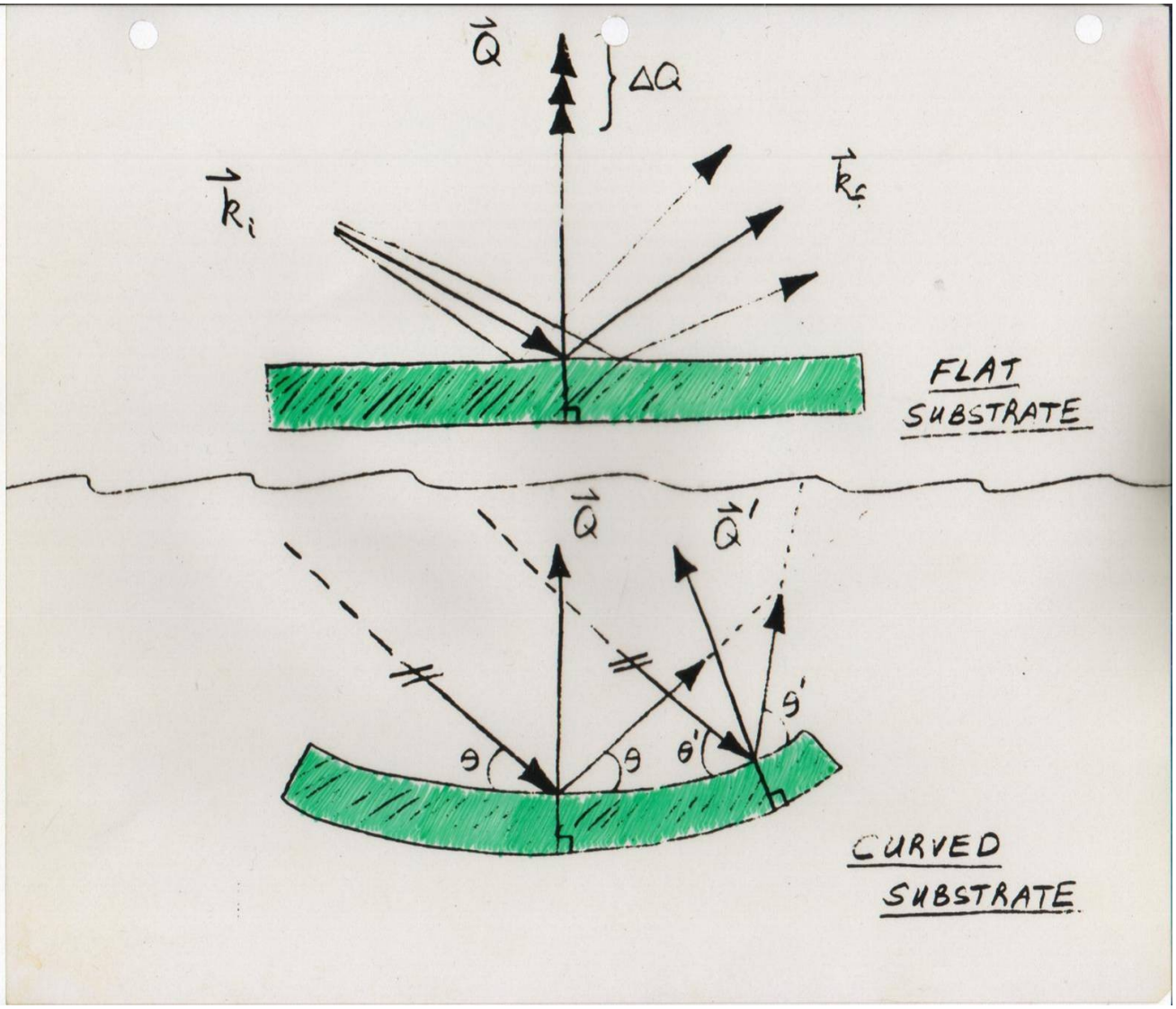
$\vec{Q}$
ΔQ
$\vec{k}_i$
$\vec{k}_f$
FLAT SUBSTRATE
$\vec{Q}$
$\vec{Q}'$
ϑ
ϑ
ϑ'
ϑ'
CURVED SUBSTRATE

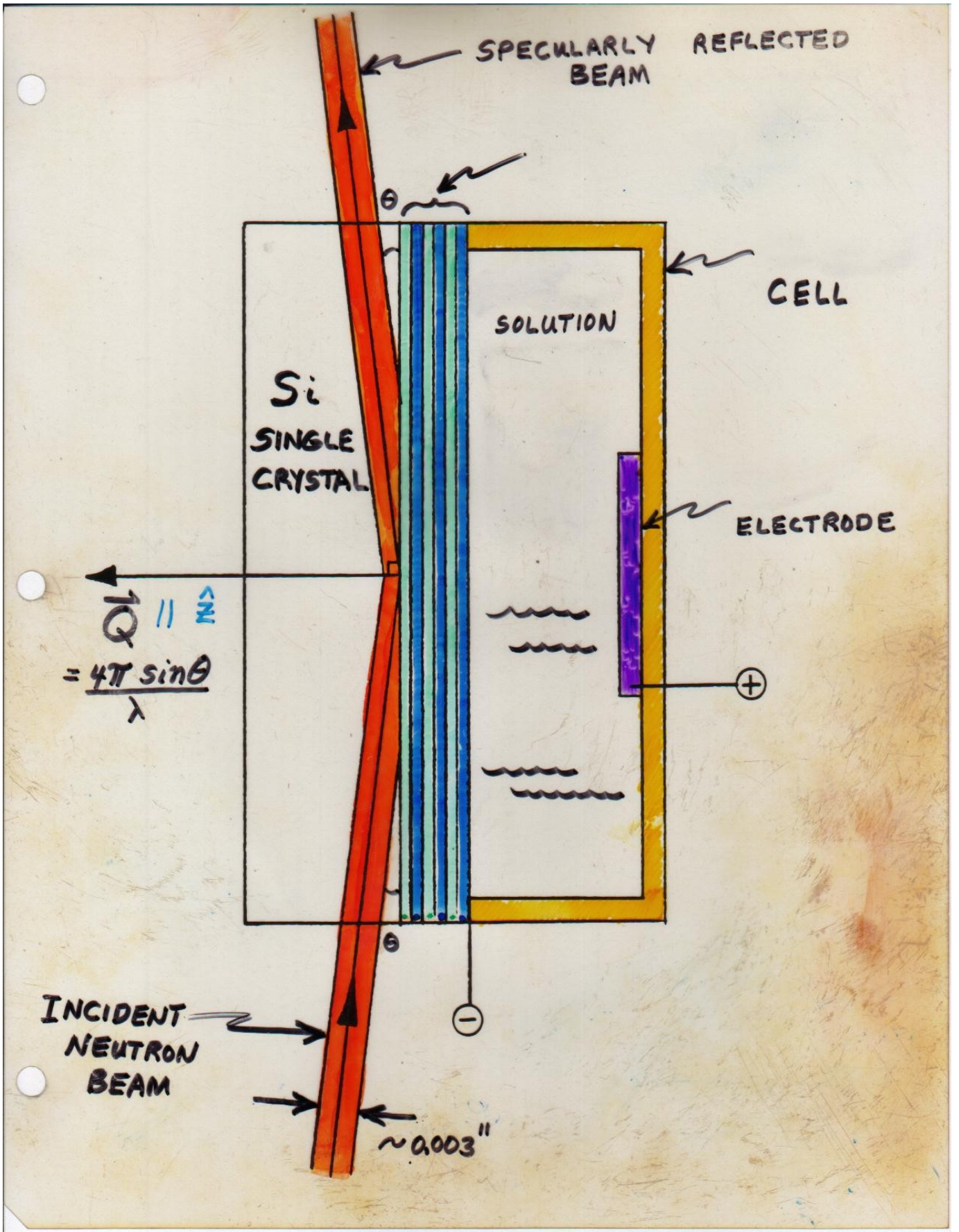
SPECULARLY REFLECTED BEAM
θ
CELL
SOLUTION
Si
SINGLE CRYSTAL
ELECTRODE
Q ∥ ẑ
= 4π sinθ / λ
θ
INCIDENT NEUTRON BEAM
~0.003"

Structure of symmetric polyolefin block copolymer thin films

Mark D. Foster,[a] Mohan Sikka, Navjot Singh, and Frank S. Bates
Department of Chemical Engineering and Materials Science, University of Minnesota, Minneapolis, Minnesota 55455

Sushil K. Satija and Charles F. Majkrzak
National Institute of Standards and Technology, Reactor Radiation Division, Gaithersburg, Maryland 20899

(Received 5 February 1992; accepted 27 February 1992)

The microstructure of thin films of nearly symmetric poly(ethylene–propylene)–poly(ethylethylene) (PEP-PEE) diblock copolymers ($f = 0.55$, where f is the volume fraction of PEP) was characterized by neutron reflectometry (NR). A symmetric film structure in which the PEE block segregates preferentially to both interfaces is observed above and below the bulk order–disorder transition (ODT). Measurements at room temperature for several chain lengths, N, provide a real-space picture of the change in interdomain interfacial profiles associated with the crossover between the strong and weak segregation limits. The polymer/air and substrate/polymer interfaces are observed to induce an ordered microstructure even when the center of the film is disordered. The characteristic dimension of this near surface microstructure is larger than the corresponding bulk value for values of χN lying between those of the bulk Gaussian-to-stretched-coil and order–disorder transitions, where χ is the segment–segment interaction parameter. This behavior is attributed to the correlation of large amplitude composition fluctuations in the film with the interfaces. A mean-field behavior prevails for $\chi N < (\chi N)_{\mathrm{GST,bulk}}$, where some preferential segregation occurs at the interfaces, but the characteristic dimension once again matches that in the bulk.

I. INTRODUCTION

In recent years interest has grown rapidly in understanding how the presence of symmetry breaking interfaces affects the microstructure and transitions of systems that n undergo order–order and order–disorder transitions. Two types of systems where considerable study has already

ly linked at one point. The overall degree of polymerization, N, the fraction of block A in the chain, f, the A–B segment–segment (Flory–Huggins) interaction parameter χ, are generally assumed to dictate the phase behavior of bulk block copolymers. At equilibrium the melt microstructure is that which minimizes the overall free energy and the transition

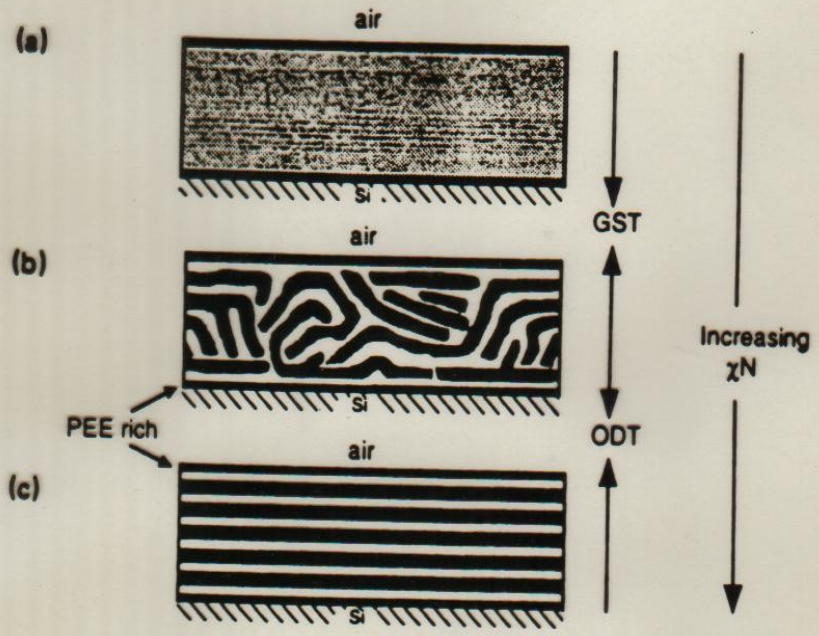

FIG. 5. Thin film morphologies for symmetric PEP–PEE diblock copolymers. (a) Interfacial segregation of PEE occurs for $\chi N < (\chi N)_{GST}$. The center of the film is spatially homogeneous. (b) For $(\chi N)_{GST} < (\chi N) < (\chi N)_{ODT}$ the film contains a microstructured morphology that is oriented at the film interfaces. The range of the orientational correlation increases with increasing (χN). (c) A lamellar microstructure that is highly oriented with the film interfaces exists when $(\chi N) > (\chi N)_{ODT}$.

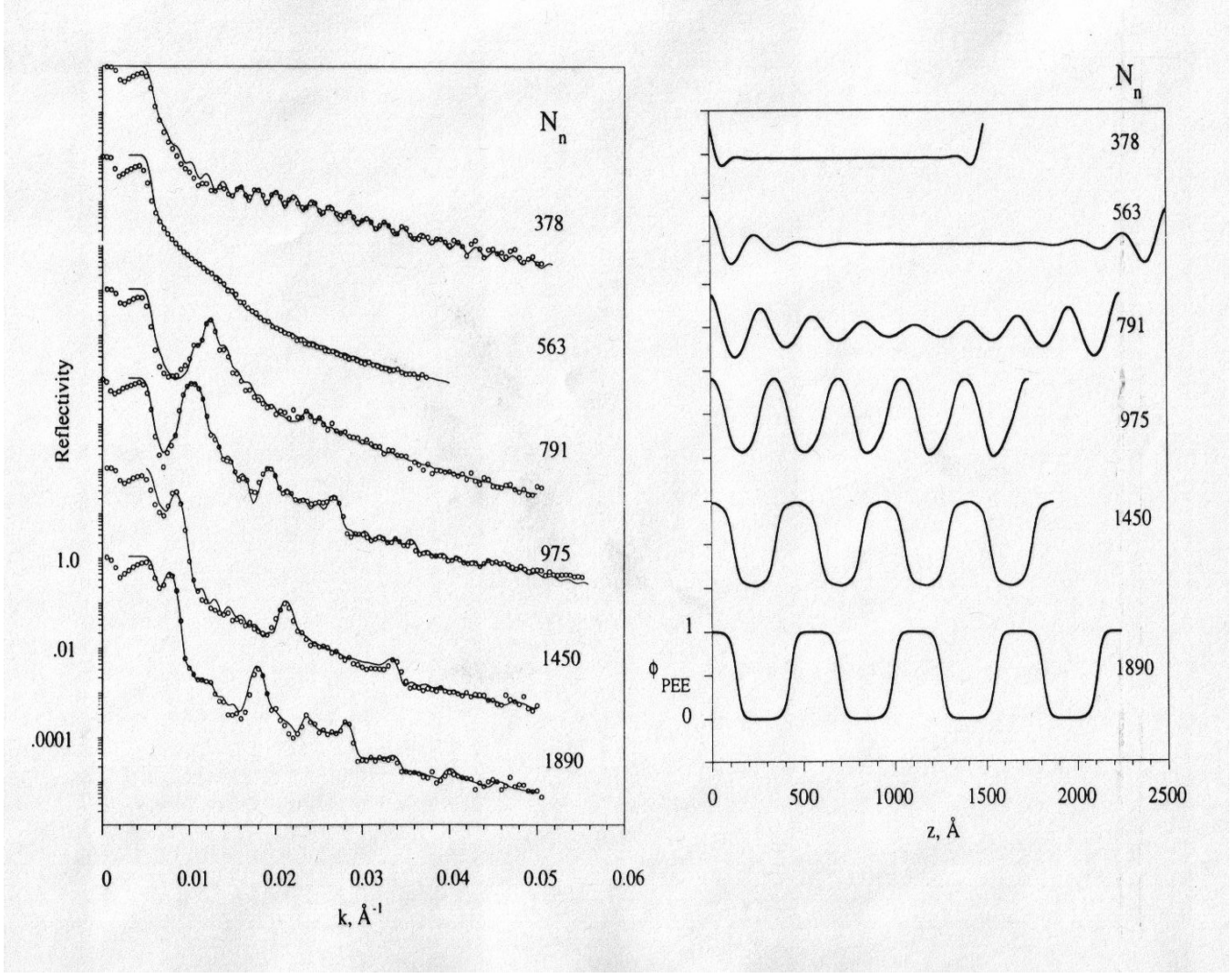
N_n
378
563
791
975
1450
1890
Reflectivity
1.0
.01
.0001
0
0.01
0.02
0.03
0.04
0.05
0.06
k, Å^-1
N_n
378
563
791
975
1450
1890
1
φ PEE
0
0
500
1000
1500
2000
2500
z, Å

Neutron Reflectivity Studies of Surfactants at Electrode Surfaces

Knowledge of the forces that control the assembly of surfactant molecules at the solid-liquid interface is vital for traditional fields such as detergency, flotation, oil recovery and tribology [1]. Thin organic films deposited at solid surfaces also find application in the fabrication of optoelectronic devices, sensors, biosensors, and chemically modified electrodes [2]. It has long been established that the assembly of surfactants at the solid-liquid interface depends on the charge at the solid surface [3, 4]. For example, the spreading of vesicles into a phospholipid bilayer requires that the surface of the solid be negatively charged and hydrophilic.

However, the present understanding of the role played by charge on the interaction of a surfactant molecule with the electrified solid surface is far from being complete. Electrochemistry provides a unique opportunity to study the effect of the charge on the properties of amphiphilic and ionic surfactants at the charged solid-liquid interface [5]. When an organic film is deposited on a gold electrode, the charge density at the metal surface may be varied from about 30 $\mu C/cm^2$ to about 40 $\mu C/cm^2$. This magnitude of charge generates electric fields on the order of 10^{10} V/m. Such a field interacts with polar molecules in the membrane. By changing the sign of the charge one can use attractive or repulsive forces. In this manner, by turning a knob on a control instrument one can force phase transitions in the film of organic molecules or force surfactants to desorb or re-adsorb on the surface.

We have recently employed electrochemical techniques, atomic force microscopy, and neutron reflectivity to study the field driven transformations of thin films formed by a model anionic surfactant, sodium dodecyl sulfate (SDS), at the surface of a gold electrode [6]. Figure 1 shows how the surface concentration of SDS at the Au electrode surface changes with the electrode potential. A convenient way to interpret these data is to look at the electrode potential as an operational variable that can be easily adjusted using a control instrument.

Figure 1 shows that the character of SDS adsorption is strongly influenced by the charge on the metal. At sufficiently negative potentials SDS molecules are totally desorbed from the electrode surface. At moderate negative

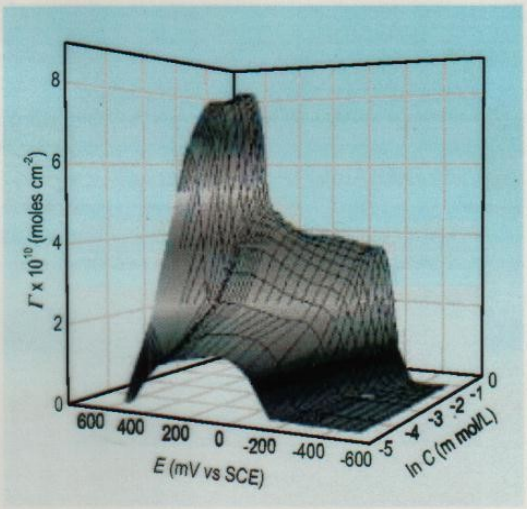

FIGURE 1. Three dimensional plots of the surface concentration of SDS as a function of electrode potential measured versus the calomel reference electrode (SCE) and the logarithm of the bulk SDS concentration.

charge densities SDS forms a film characterized by a limiting surface concentration 4.0×10^{-10} mol cm^{-2}. When the metal surface is positively charged the surface concentration of SDS increases to 8.1×10^{-10} mol cm^{-2}.

Neutron reflectivity experiments carried out on the NG-7 reflectometer were employed to determine the structure of the film formed by SDS at different charge densities at the gold surface. Thin layers of chromium (≈ 20 Å) and gold (≈ 80 Å) were sputtered onto the crystal quartz substrate. After cleaning, the crystal was mounted on a specially constructed Teflon® cell [7]. The cell had ports for the counter (gold foil) and reference electrodes (Ag/AgCl, $E \approx -40$ mV versus SCE). D_2O (99.9 % molecular fraction) was used as a solvent in reflectivity studies.

Figure 2a shows the neutron reflectivity data determined for SDS adsorption at various electrode potentials, and Fig. 2b shows the scattering length density profiles calculated from the reflectivity curves. The neutron reflectivity data are consistent with electrochemical measurements. They show that at very negative potentials the gold solution interface is free from hydrogenated species. When

I. Burgess, V. Zamlynny, G. Szymanski, and J. Lipkowski
Department of Chemistry and Biochemistry
University of Guelph
Guelph, ONT N1G 2W1, Canada

J. Majewski and G. Smith
Los Alamos National Laboratory
Los Alamos, NM 87545

S. Satija and R. Ivkov
NIST Center for Neutron Research
National Institute of Standards and Technology
Gaithersburg, MD 20899-8562

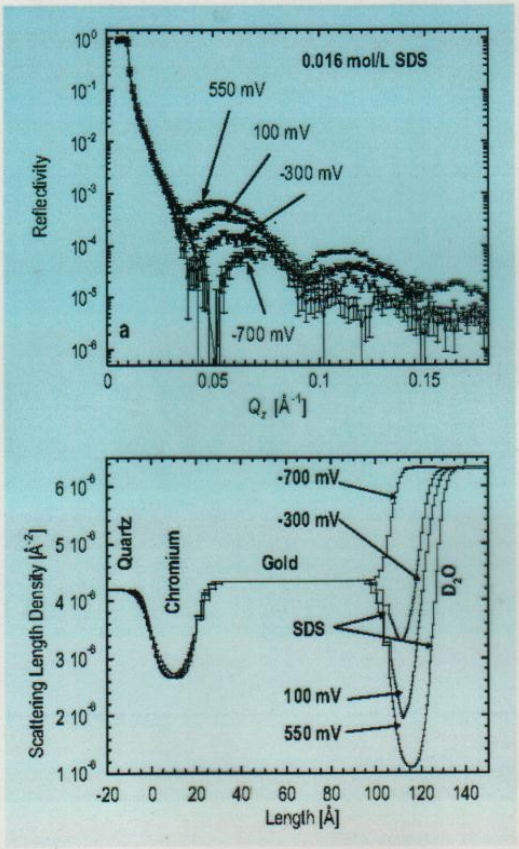

FIGURE 2. (a) Normalized neutron reflectivity curves for a Au/Cr-coated quartz substrate in 0.016 mol/L SDS in D_2O. (b) Scattering length density profiles of the interface as determined from the fitting procedure.

the potential increases, the film of hydrogenated species appears at the electrode surface. The thickness of this film increases, and the scattering length density progressively decreases, with increasing potential. When combined with the results of electrochemical measurements and atomic force imaging, the neutron reflectivity data allow the determination of the structure of the film formed at different charge densities. At small or moderate negative charge densities SDS molecules form a hemimicellar film that consists of hemicylindrical stripes, as first observed by Manne [4]. The packing of SDS molecules in a cross section of that hemicylinder is shown schematically in Fig. 3 (top). At positive charge densities the hemimicellar state is transformed into the interdigitated bilayer schematically shown in Fig. 3 (bottom).

The results of this study demonstrate the need for the use of neutron reflectometry to study adsorption and phase transitions in films of surfactants adsorbed at the solid-solution interface. Specifically, they show that when neutron reflectivity measurements are combined with electrochemical studies and atomic force microscopy, they provide unique opportunities to study different stages involved in the interaction of surfactants with solid surfaces.

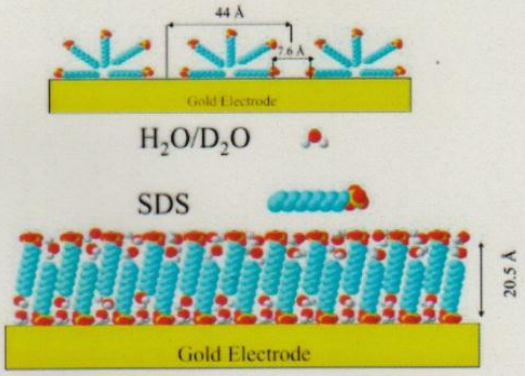

FIGURE 3. Models of SDS adsorption at the Au-solution interface: (top) cross section of hemicylindrical aggregates observed at moderately negative charge densities; (bottom) interdigitated bilayer observed at positive charge densities.

References

[1] A.W. Adamson, Physical Chemistry of Surfaces, 5th ed., John Wiley & Sons, New York (1990).

[2 E. Sackmann, Science **271**, 43 (1996).

[3] P. Chandar, P. Somasundaran, N. J. Turro, J. Colloid Interface Sci. **117**, 31 (1987).

[4] S. Manne, Progr. Colloid Polym. Sci. **103**, 226 (1997).

[5] D. Bizzotto, J. Lipkowski, J. Electroanal. Chem. **409**, 33 (1996).

[6] V. Zamlynny, I. Burgess, G. Szymanski, J. Lipkowski, J. Majewski, G. Smith, S. Satija, and R. Ivkov, Langmuir **16**, 9861(2000).

[7] I. Burgess, V. Zamlynny, G. Szymanski, J. Lipkowski, J. Majewski, G. Smith, S. Satija, and R. Ivkov, Langmuir **17**, 3355 (2001).

Phase Sensitive Neutron Reflectometry on a Water-Cushioned Biomembrane-Mimic

Biomimetic membranes have been developed as models of living cell membranes, and this has applications in the quest for biocompatibility of inorganic materials in biologically active mediums, such as coatings for artificial organs. A membrane consists of a lipid bilayer (two lipid layers) where hydrophobic carbon chains form the inside of the membrane and their polar head groups the interface with the aqueous surrounding medium. A supported membrane-mimic consists of a lipid-like bilayer, typically attached to a single-crystal substrate, with access to water only at the top surface [1, 2]. Here we use neutron reflectometry to study a system in which water has access to both sides of a membrane-mimic attached to such a substrate, thus making the system a closer mimic to a real cell membrane.

The system devised by Liu *et al.* [3] consists of a water-swellable polyelectrolyte that electrostatically binds to the substrate and acts as a "cushion" for the membrane, not unlike the cytoskeletal support found in actual mammalian cell membranes. The lower half of the membrane-mimic is a terpolymer that attaches to the polyelectrolyte. A phospholipid layer forms on top of the terpolymer and the bilayer is finally chemically crosslinked for added stability. The system is shown schematically in Fig. 1.

Neutron reflectivity measurements were performed at the NG-1 vertical stage reflectometer to obtain the compositional profile at every step of the assembling process of the membrane-mimic which consisted of three stages: a) polyelectrolyte multilayer (PE), b) polyelectrolyte multilayer plus terpolymer (PE+TER), and c) polyelectrolyte multilayer plus terpolymer plus phospholipid layer (PE+TER+PC) [4]. The spatial resolution attained was approximately 10 Å, about half the thickness of a membrane bilayer, making it possible to distinguish the two layers of a membrane but not the structure of a single layer.

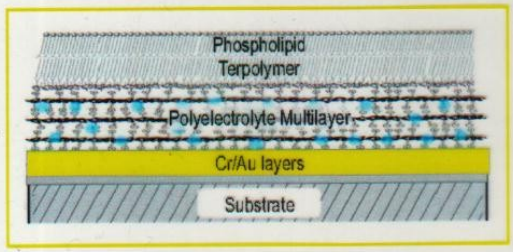

Fig. 1. Schematic diagram of a biomimetic membrane. The phospholipid layer at the top combines with the terpolymer layer to form a membrane-mimic that in turn resides on the water (blue dots) permeable "cushion" polyelectrolyte multilayer. The latter attaches electrostatically to the Au-capped substrate.

A unique compositional profile of the biomimetic film with no a priori knowledge of the sample's composition is obtained by measuring the reflectivity of equivalent samples made onto two substrates [5]. The substrates used were single crystal silicon (Si) and sapphire (Al_2O_3) coated with chromium (Cr) and then a gold (Au) layer to allow the polyelectrolytes to bind to a similar surface on both wafers.

Figure 2 shows the compositional profiles for the PE, PE+TER and PE+TER+PC assemblies in a D_2O atmosphere at 92 % relative humidity. The figure shows that the hydration of the PE layer is almost unaffected by the addition of the terpolymer and the phospholipid layer. Also, upon the addition of the phospholipid layer to the PE+TER assembly, the composite PE+TER+PC assembly shows an increase in thickness of approximately 30 Å, consistent with the formation of a single phospholipid layer at the surface. It is also clear that the addition of a phospholipid layer onto the terpolymer layer rearranges this region

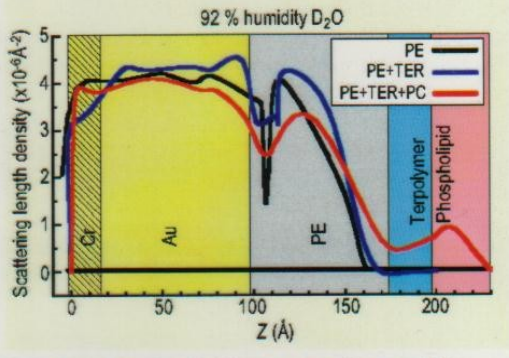

Fig. 2. Compositional profile of biomimetic membrane in a D_2O atmosphere at 92 % relative humidity at various stages of assembly on Au-capped substrate: only polyelectrolyte (PE), polyelectrolyte and terpolymer (PE+TER), polyelectrolyte, terpolymer and phospholipid (PE+TER+PC). The compositional profile is given by the scattering length density, SLD, profile when using neutrons.

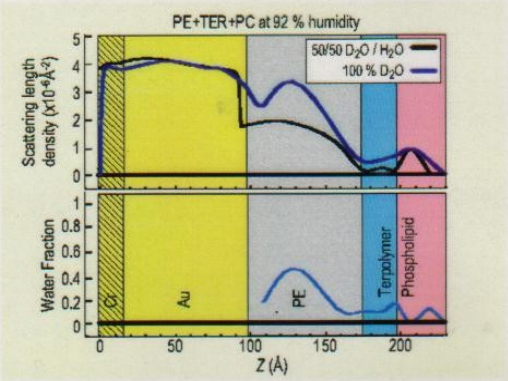

Fig. 3. Scattering length density profiles (top) and water fraction (bottom) for PE+TER+PC under indicated conditions.

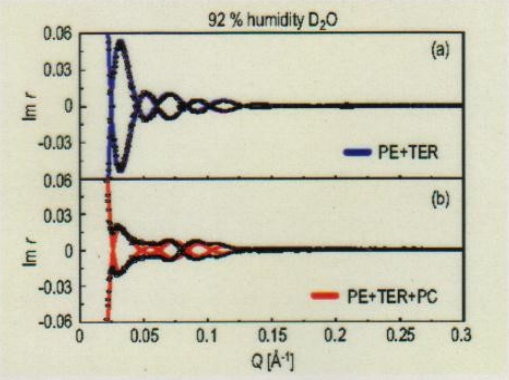

Fig. 4. Imaginary part of the complex reflectivity, Im $r(Q)$, data (symbols) and calculated curves (lines) obtained from the SLD profiles for the PE+TER and the PE+TER+PC assemblies shown in Fig. 2.

significantly, since the terpolymer layer only becomes apparent after the phospholipid layer is added. It is possible to verify with an independent technique (contact angle) that the terpolymer was in fact deposited because it forms a hydrophobic outer layer. The outer surface becomes hydrophilic once the phospholipid layer is deposited onto the terpolymer layer.

Figure 3 (top) shows the profile for the PE+TER+PC assembly under 92 % relative humidity in 100 % D_2O and in 50/50 D_2O/H_2O. The overall thickness change due to the intake of water, in going from dry (not shown) to 92 % relative humidity, was found to be 20 Å. Figure 3 (bottom) shows the water fraction in the assembly under 92 % relative humidity. This is obtained by assuming that the distribution of each component in the layers is unaffected by having either D_2O or 50/50 D_2O/H_2O. From the figure it can be seen that the polyelectrolyte multilayer has a 40 % water uptake. This is a significant amount of water, which suggests that the polyelectrolyte multilayer can work as a "cushion" for membrane-mimetic systems. The terpolymer and the phospholipid layers contain an average of 10 % water, which is also significant, suggesting that these layers are not tightly packed.

The method of making equivalent samples on two substrates to obtain a unique compositional profile has a built-in congruency test, particularly useful in checking the reproducibility of the samples as well as the quality of the films. The test is to compare the calculated imaginary part of the complex reflectivity from the obtained profile with the corresponding data, as is shown in Fig. 4 for the PE+TER and PE+TER+PC assemblies. From Fig. 4 it is concluded that the PE+TER samples are homogenous and essentially identical while for the PE+TER+PC assembly, the absence of true zeros, as indicated by the calculated curve, is suggestive of a small degree of sample inhomogeneity.

The system from Liu *et al.* has many characteristics desirable in a biomimetic membrane. It is a single membrane-mimic attached to a significantly hydrated soft "cushion" support that allows some membrane proteins to function. Thrombomodulin, a membrane protein relevant to blood-clotting, is being studied in this membrane-mimic environment to further develop biocompatible coatings for artificial organs [6].

References

[1] E. Sackmann, Science **271**, 43 (1996).

[2] A. L. Plant, Langmuir **15**, 5128 (1999).

[3] H. Liu, K. M. Faucher, X. L. Sun, J. Feng, T. L. Johnson, J. M. Orban, R. P. Apkarian, R. A. Dluhy, E. L. Chaikof, Langmuir **18**, 1332 (2002).

[4] U. A. Perez-Salas, K. M. Faucher, C. F. Majkrzak, N. F. Berk, S. Krueger, E. L. Chaikof, Langmuir **19**, 7688 (2003).

[5] C. F. Majkrzak, N. F. Berk, U. A. Perez-Salas Langmuir **19**, 1506 (2003).

[6] J. Feng, P. Y. Tseng, K. M. Faucher, J. M. Orban, X. L. Sun, E. L. Chaikof, Langmuir **18**, 9907 (2002).

U. A. Perez-Salas
NIST Center for Neutron Research
National Institute of Standards and Technology, Gaithersburg, MD 20899-8562

K. M. Faucher
Emory University School of Medicine, Atlanta, GA 30322

C. F. Majkrzak, N. F. Berk, S. Krueger
NIST Center for Neutron Research
National Institute of Standards and Technology
Gaithersburg, MD 20899-8562

E. L. Chaikof
Emory University School of Medicine
Atlanta, GA 30322

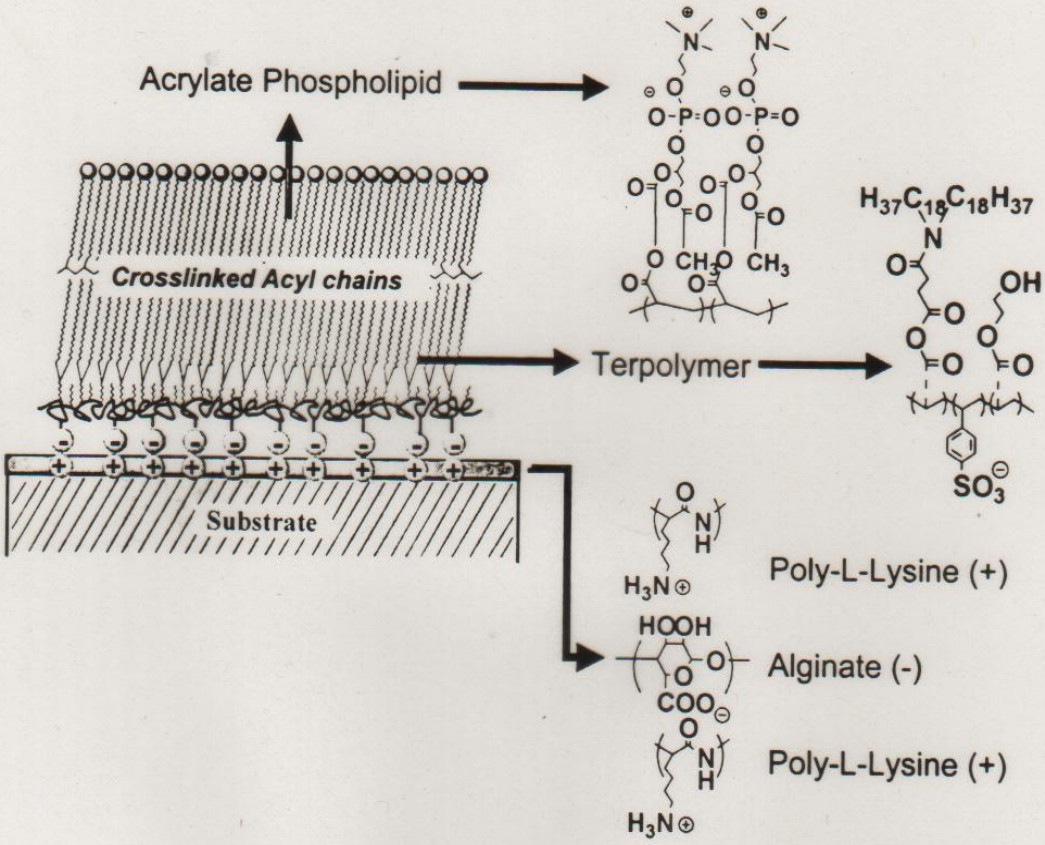

Figure 1:

1 Schematic representation the terpolymer (TER)-acrylate phospholipid (PC) membrane mimic supported on a polyelectrolyte multilayer(PE) "cushion". . . . . .

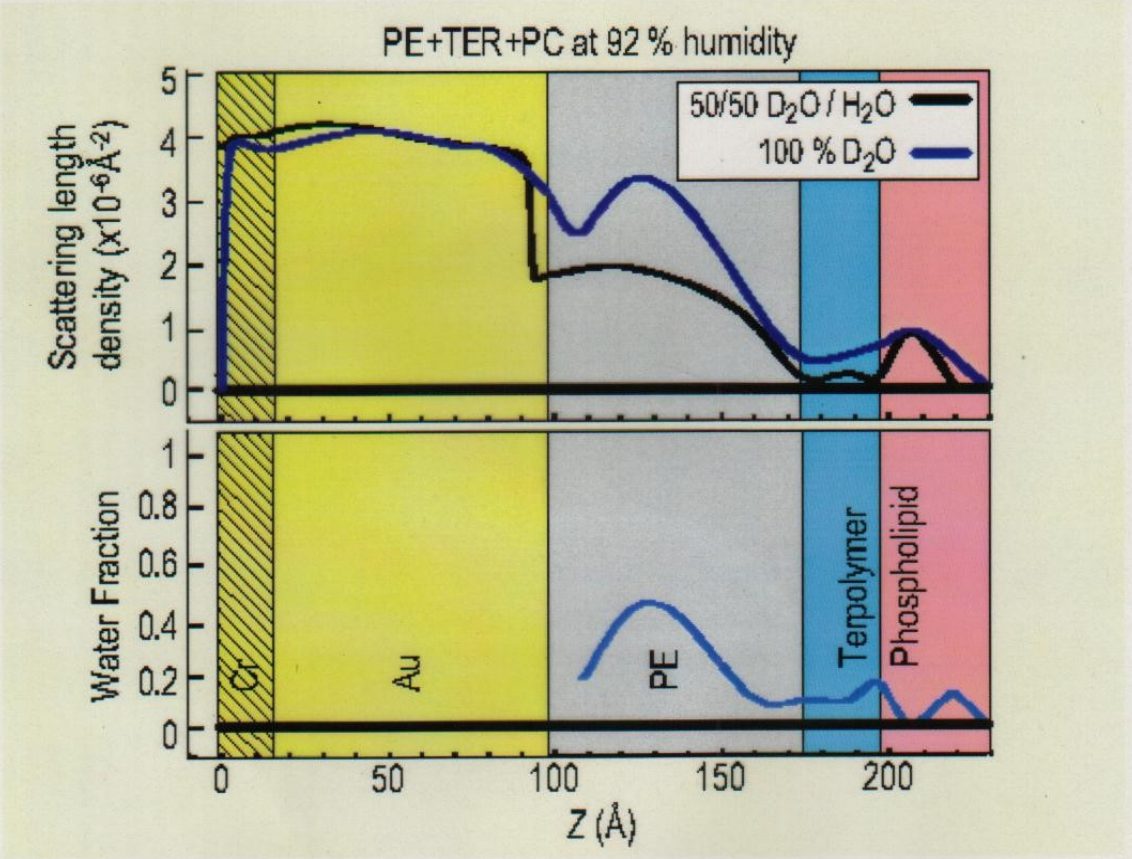

Fig. 3. Scattering length density profiles (top) and water fraction (bottom) for PE+TER+PC under indicated conditions.

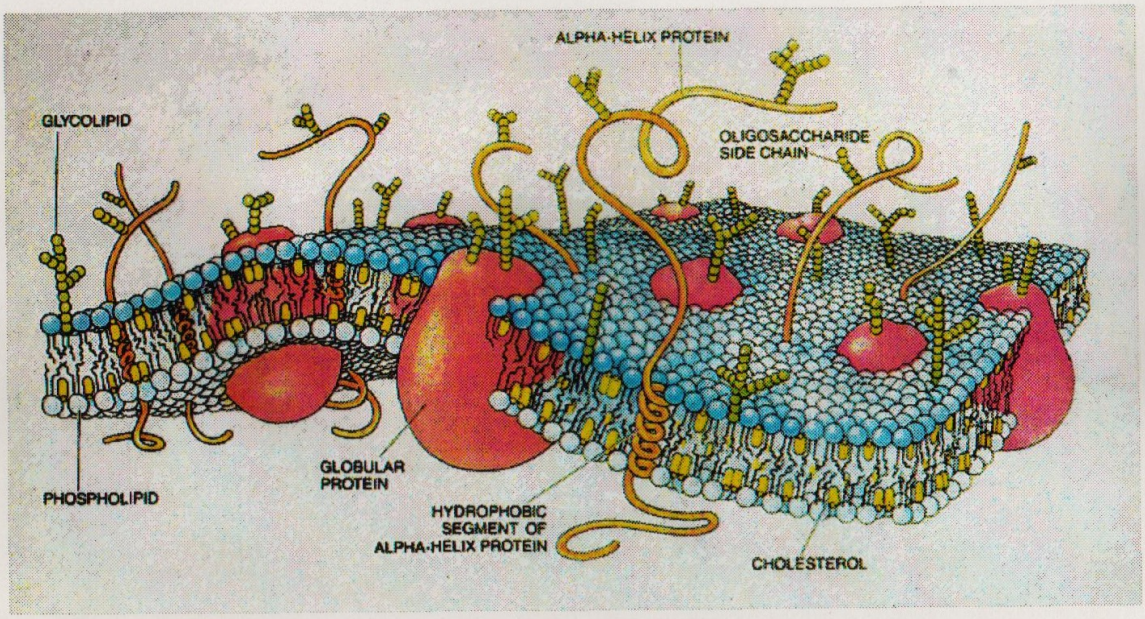

BORROWED FROM SCIENTIFIC AMERICAN

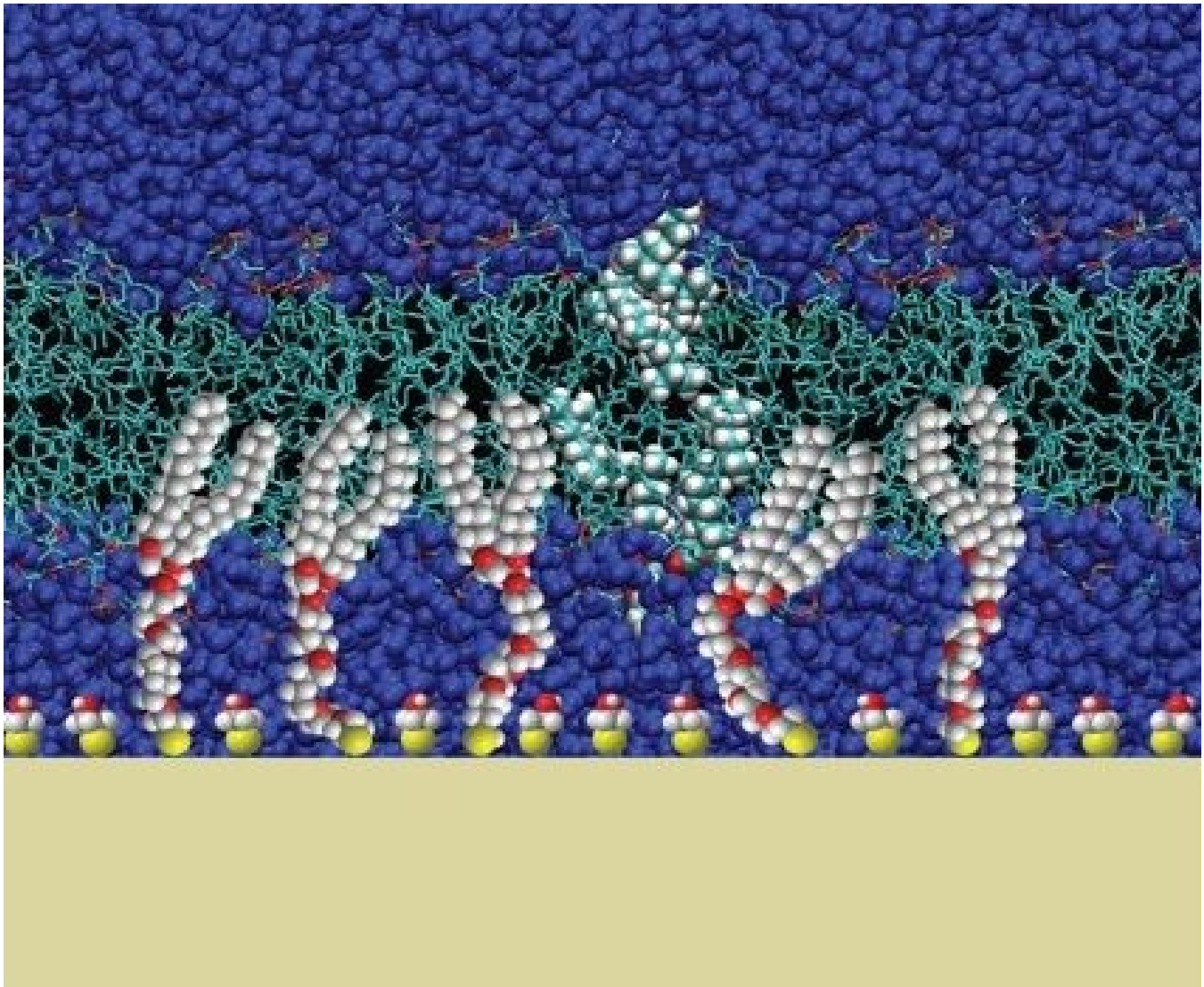

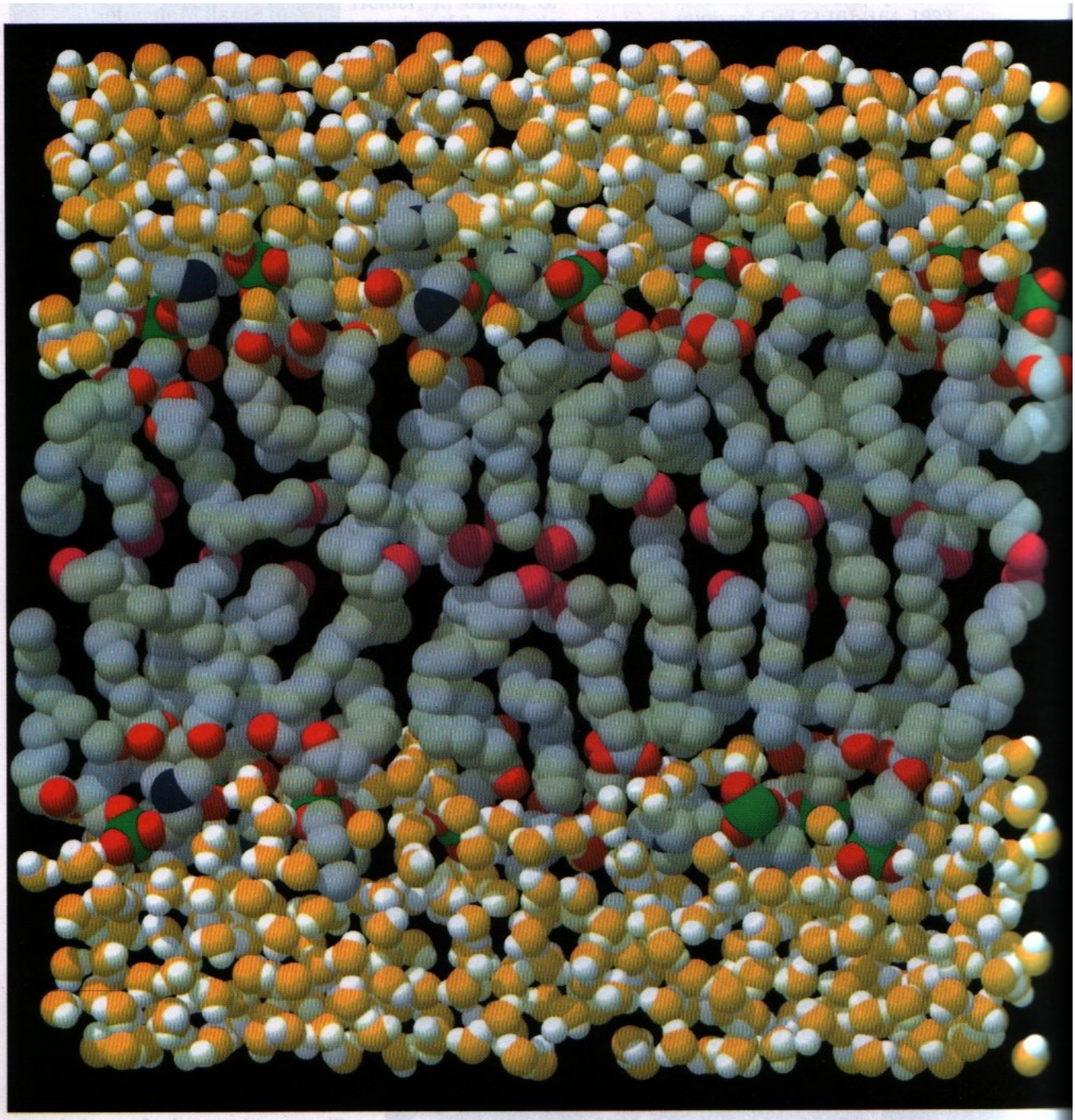

A computer simulation of a 0.8-nm slab of a phospholipid bilayer in water. Phosphorus atoms are shown in *green,* nitrogen atoms in *dark blue,* lipid oxygen atoms in *red,* terminal-chain groups in *magenta,* and other carbon atoms in *gray;* the carbon hydrogen atoms are omitted. The water molecules are shown in *yellow* (oxygen) and *white* (hydrogen). (From R.M. Venable, Y. Zhang, B.J. Hardy, and R.W. Pastor, *Science* 262, 223–228, 1993.)

Lipid Phase Transitions

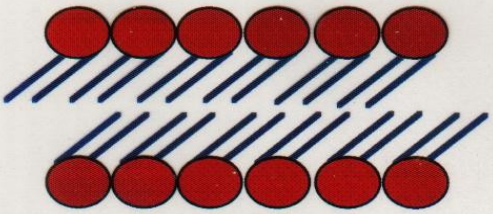

L_{β}' Crystalline
"Gel" State

Increasing Temperature

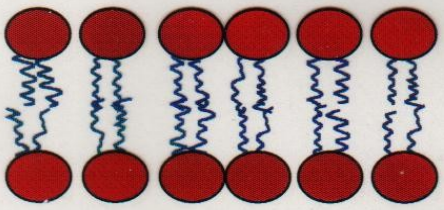

L_{α} Liquid Crystalline
Fluid State (thinner)

Transition State P_{α}
Surface Effect ?

DMPC	24 (14) °C
DPPC	42 (35) °C
DSPC	54 (49) °C

(S. KRUEGER ET AL.)

Effect of Temperature on the Neutron Reflectivity of DPPC in Si-Matched H_2O/D_2O

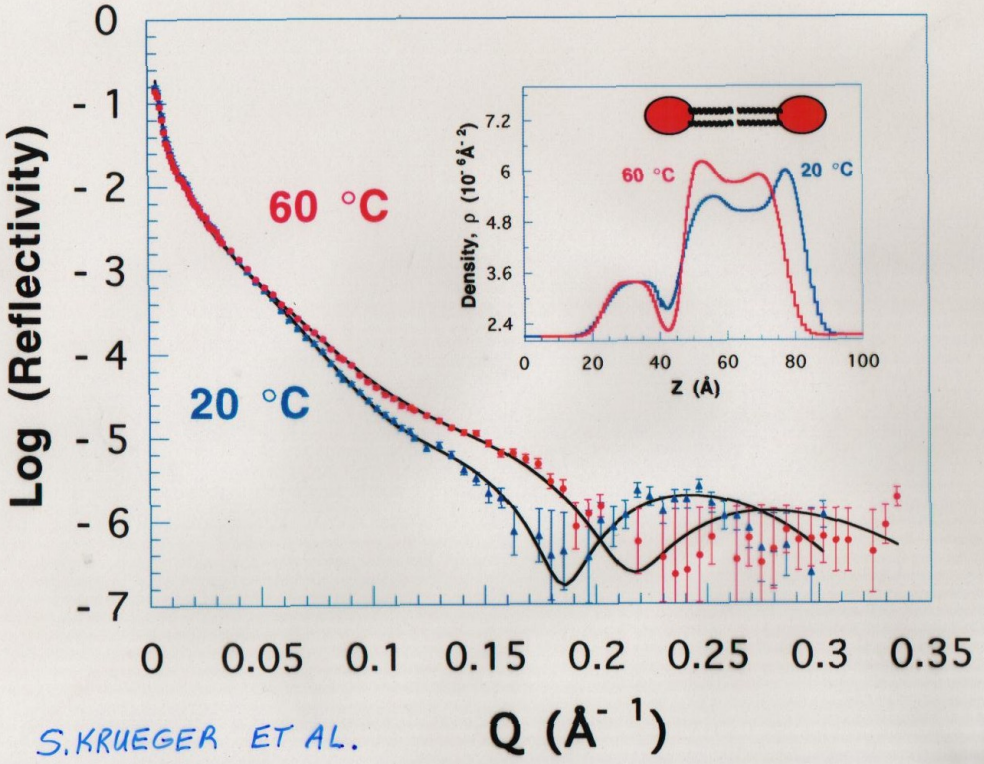

S. KRUEGER ET AL.

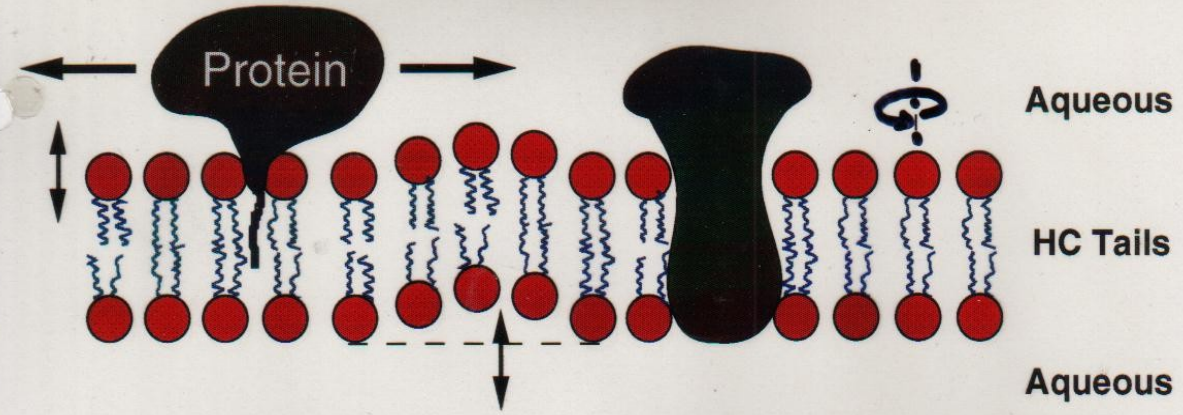

Supported Lipid Bilayers

A model system to mimic the structure and dynamics of cell membranes.

Proteins in Lipid Bilayers

- **Difficult to characterize by traditional x-ray crystallography.**
- **Play a crucial role in cell function**
  - **regulate ion and nutrient transport**
  - **engage in binding, signalling and cell recognition**
  - **participate in cell fusion events.**

Biosensors (Anne Plant & coworkers)

Melittin in Hybrid Bilayer Membranes

S. Krueger, A. Plant, et al., NIST (Langmuir)

- pore-forming toxin
- used as model membrane peptide
- active in HBMs

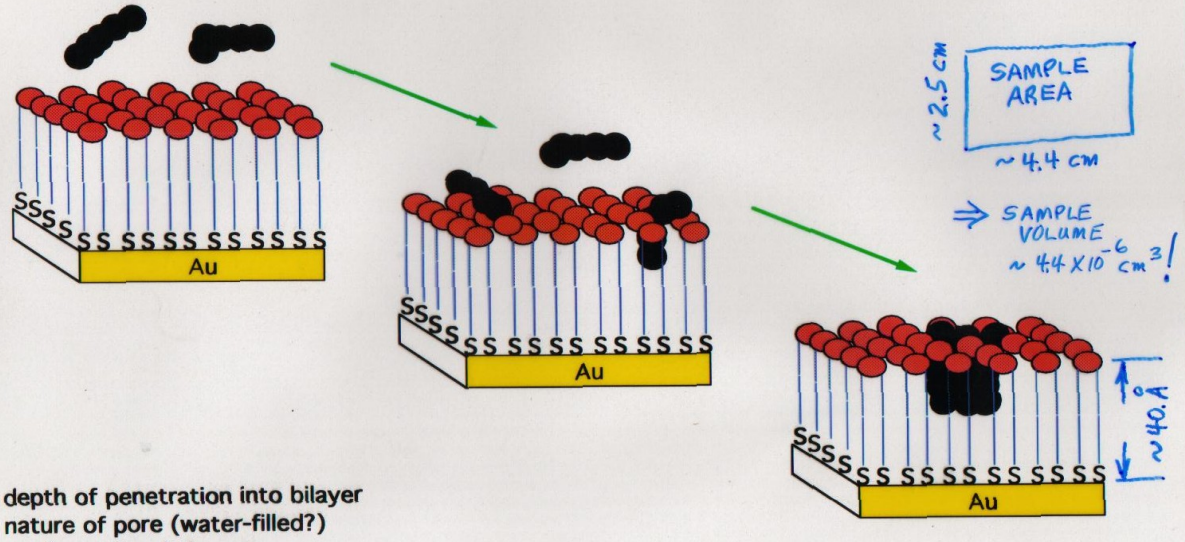

- depth of penetration into bilayer
- nature of pore (water-filled?)
- conformational changes
- random or ordered distribution?
- influence on surrounding lipids (location,conformation)

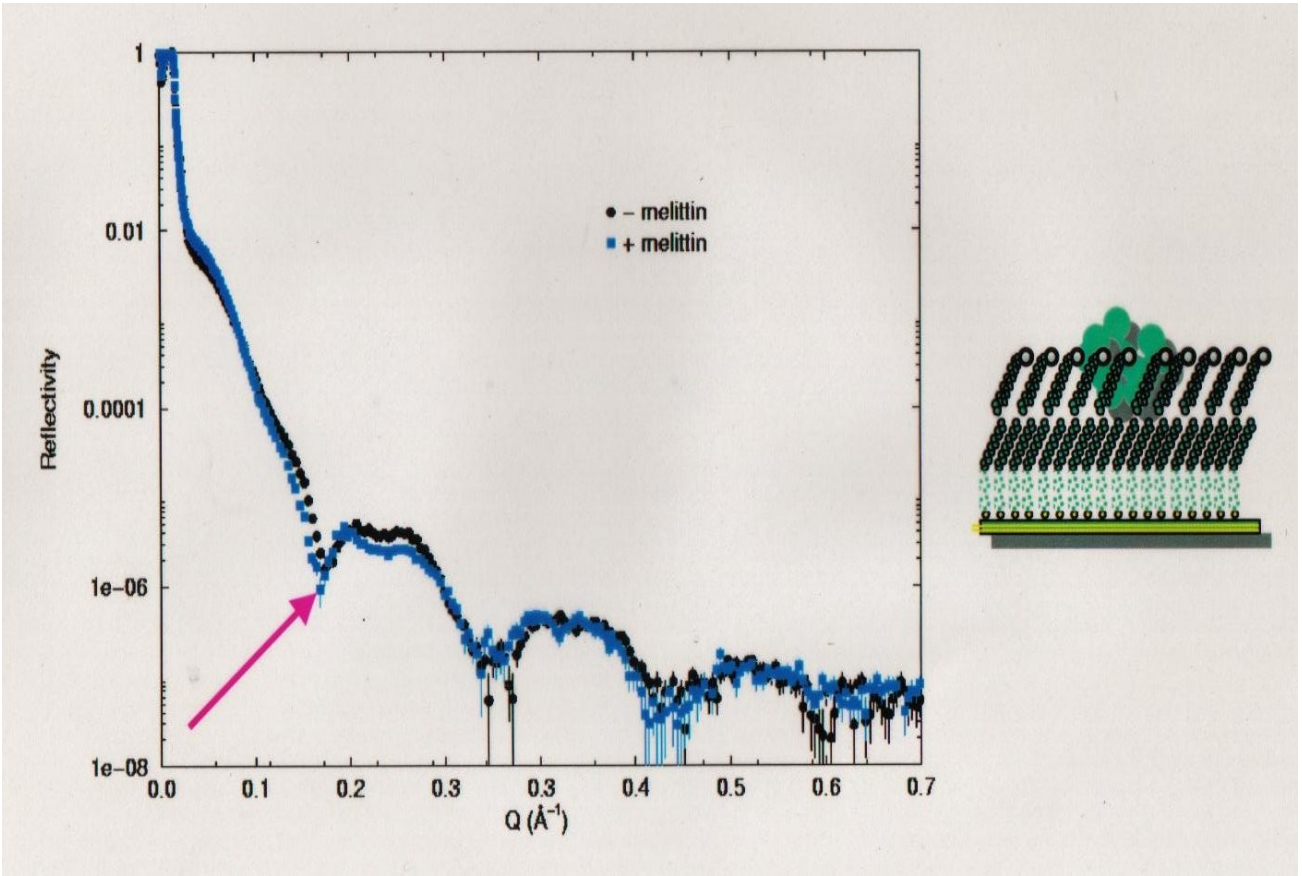
1
0.01
0.0001
1e–06
1e–08
Reflectivity
0.0
0.1
0.2
0.3
0.3
0.4
0.5
0.6
0.7
Q (Å^{-1})
– melittin
+ melittin

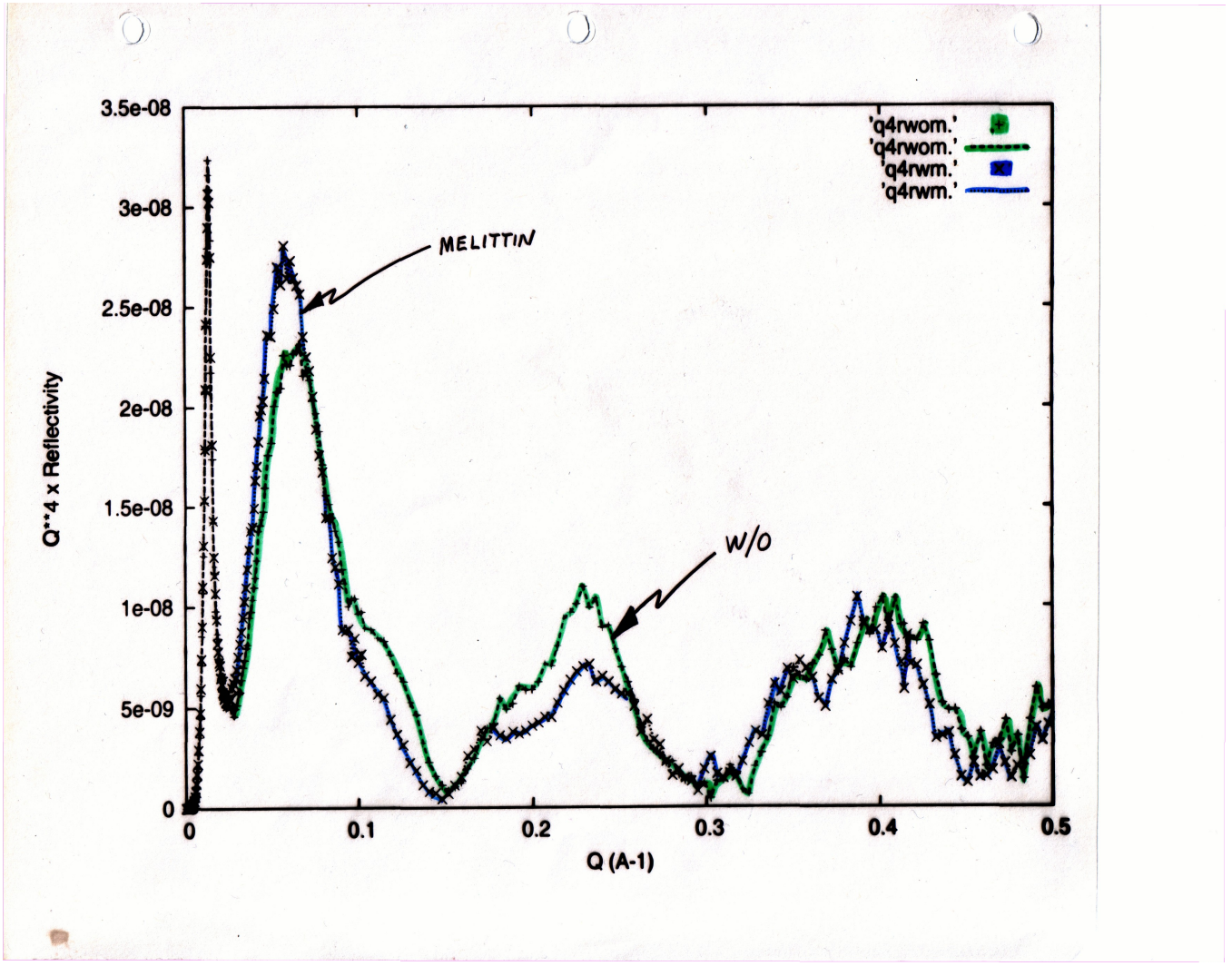
'q4rwom.'
'q4rwom.'
'q4rwm.'
'q4rwm.'
MELITTIN
W/O
Q**4 x Reflectivity
Q (A-1)
3.5e-08
3e-08
2.5e-08
2e-08
1.5e-08
1e-08
5e-09
0
0
0.1
0.2
0.3
0.4
0.5

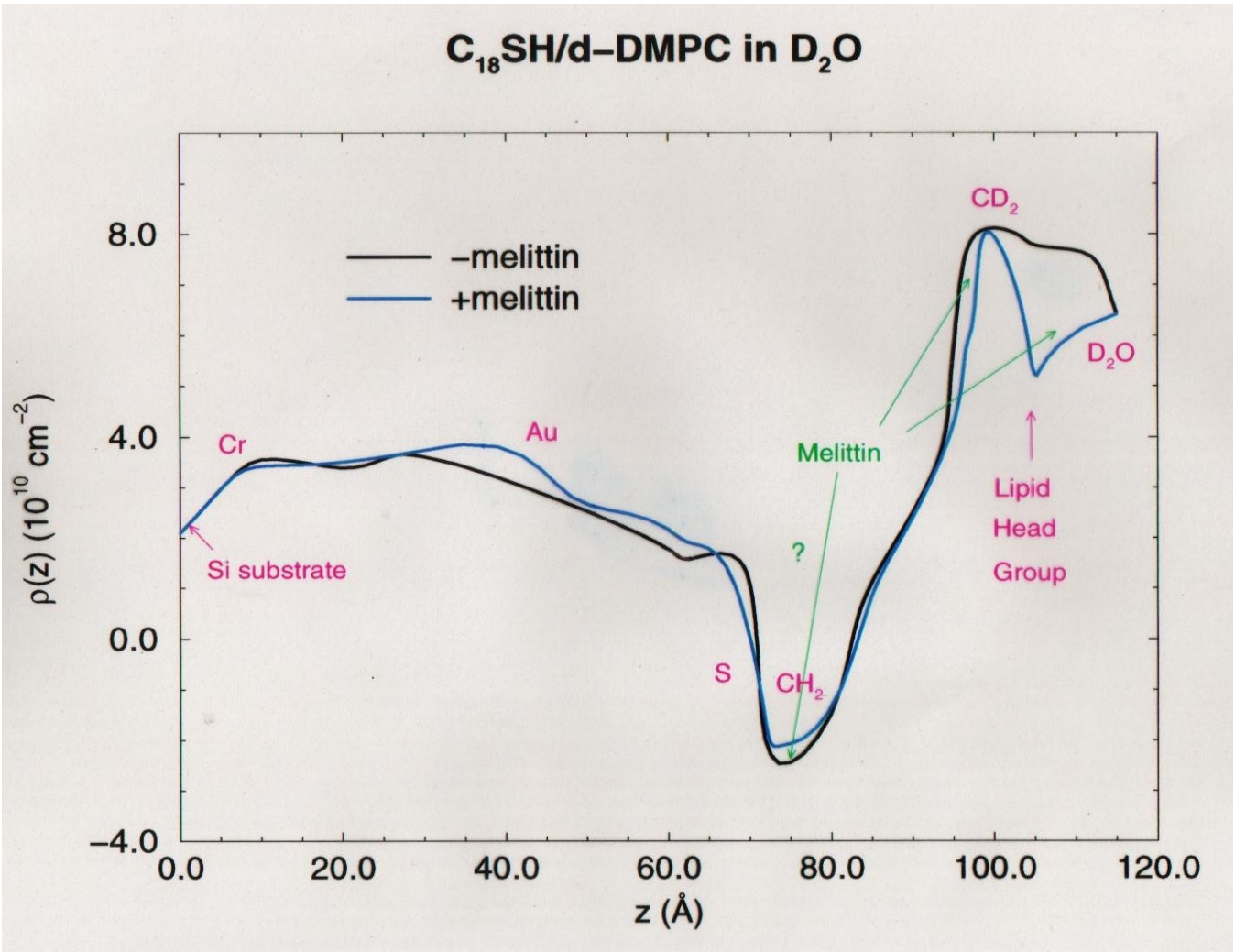
C18SH/d–DMPC in D2O
–melittin
+melittin
CD2
D2O
Cr
Au
Melittin
?
Lipid
Head
Group
Si substrate
S
CH2
8.0
4.0
0.0
–4.0
0.0
20.0
40.0
60.0
80.0
100.0
120.0
z (Å)
ρ(z) (10^10 cm^-2)

S. KRUEGER, C.F. MAJKRZAK, N.F. BERK, M. TAREK, D. TOBIAS,
V. SILIN, J.A. DURA, C.W. MEUSE, J. WOODWARD, A.L. PLANT
(Langmuir)

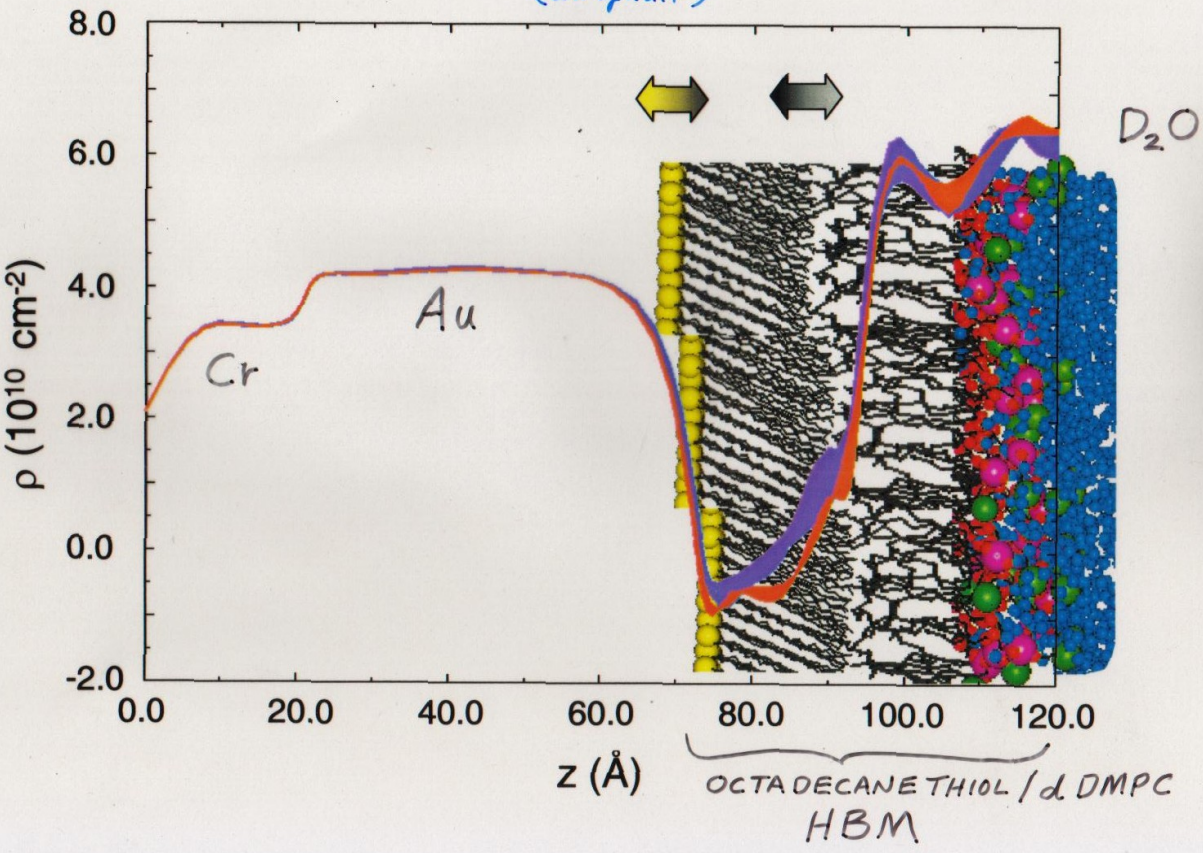

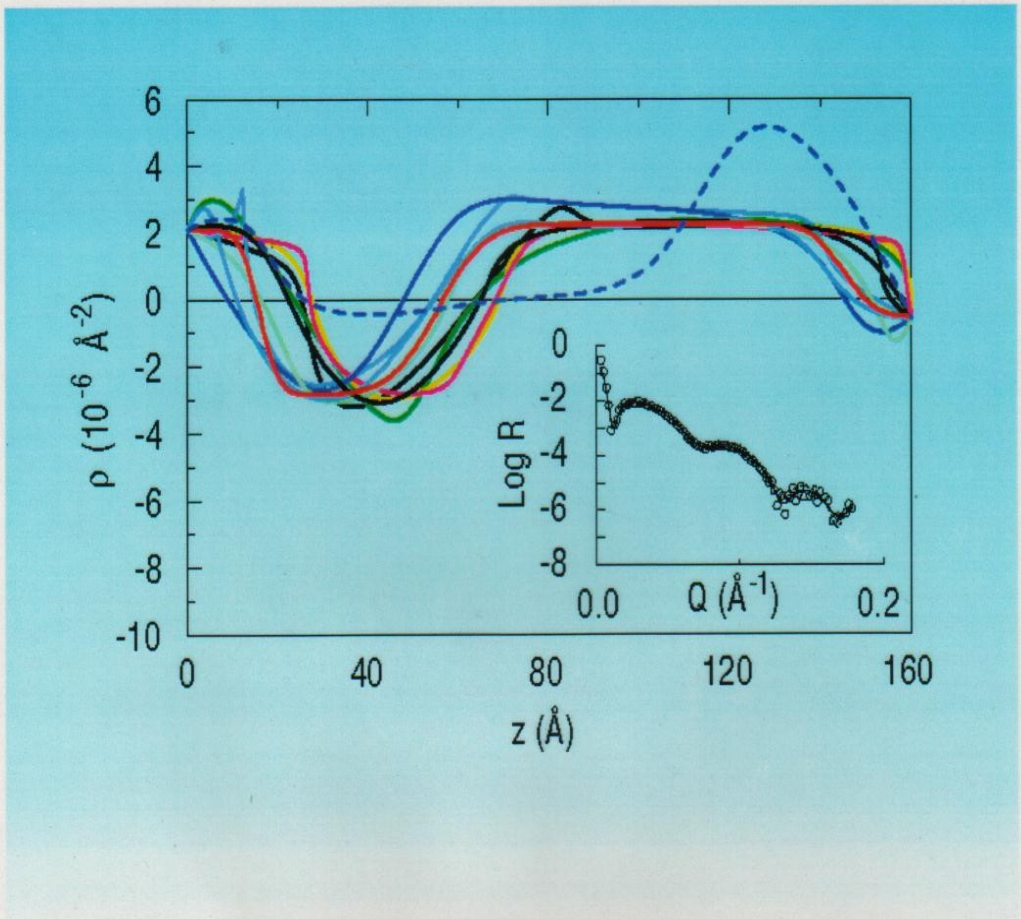

FIGURE 1. Family of scattering length density profiles obtained by model-independent fitting of the reflectivity data in the inset. The profile represented by the blue dashed line is unphysical for this Ti/TiO film system yet generates a reflectivity curve that fits the data with essentially equivalent goodness-of-fit (all the reflectivity curves corresponding to the SLD's shown are plotted in the inset but are practically indistinguishable from one another).

Inverting reflectivity

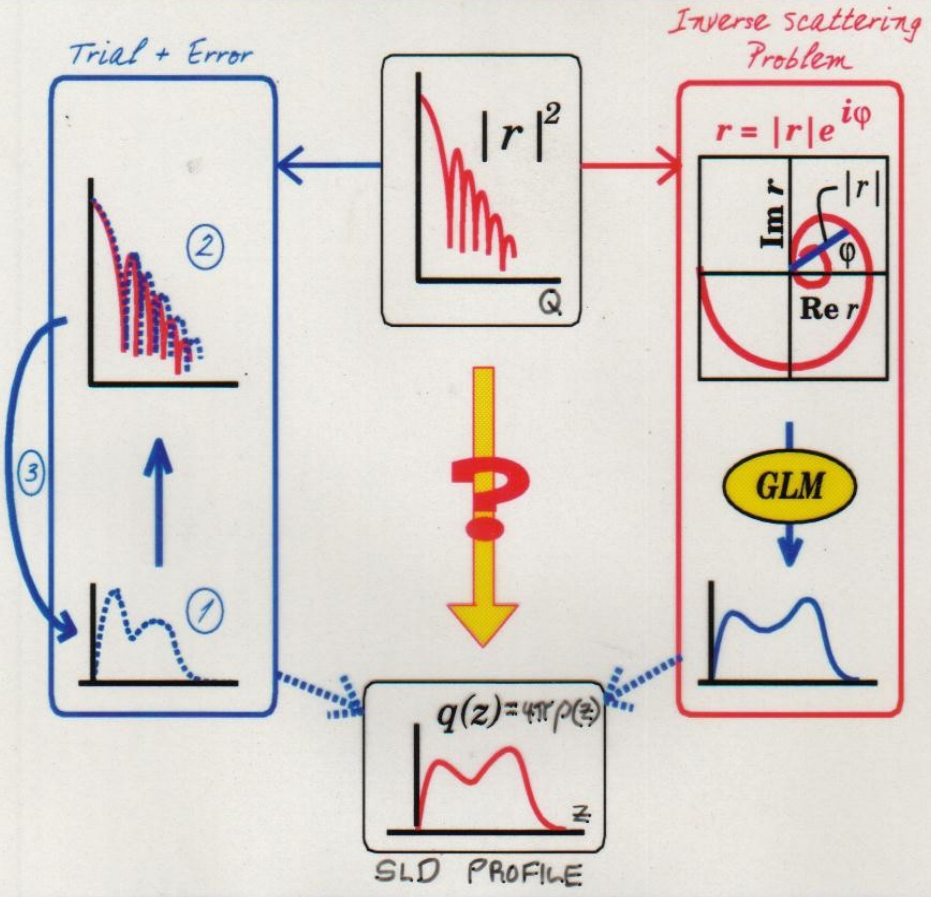

Phase determination

C.F. Majkrzak and N.F. Berk, Phys. Rev. B **52**, 10827 (1995).
V.–O. de Haan, et al., Phys. Rev. B **52**, 10830 (1995).
↳ A.A. van Well, S. Adenwalla, & G.P. Felcher
H. Leeb, H.R. Lipperheide and G. Reiss, this conference.

Logarithmic dispersion

W.L. Clinton, Phys. Rev. B **48**, 1 (1993).

Tunneling times

H. Fiedeldey, H.R. Lipperheide, et al., Phys. Lett. A **170**, 347 (1992).

Pseudo–inversion

S.K. Sinha, et al., *Surface X–Ray and Neutron Scattering*, 85 (Springer, 1992).
C.F. Majkrzak, N.F. Berk, et al., SPIE Proc. **1738**, 282 (1992).

NIST

Phase Determination with 3 References

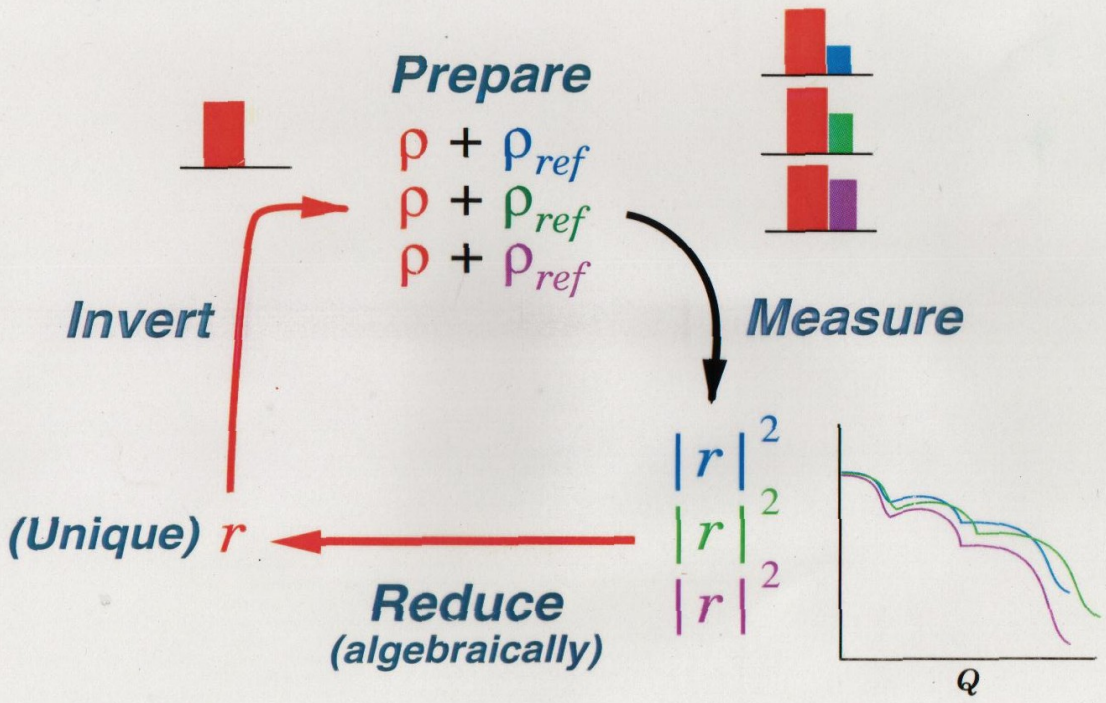

Majkrzak & Berk, 1995
de Haan, et al., 1995

UNIQUE DETERMINATION OF BIOMIMETIC MEMBRANE PROFILES BY NEUTRON REFLECTIVITY

New biomimetic membrane materials, of fundamental importance in understanding such key biological processes as molecular recognition, conformational changes, and molecular self-assembly, can be characterized using neutron reflectometry. In particular, scattering length density (SLD) depth profiles along the normal to the surface of a model biological bilayer, which mimics the structure and function of a genuine cell membrane, can be deduced from specular neutron reflectivity data collected as a function of wavevector transfer Q. Specifically, this depth profile can be obtained by numerically fitting a computed to a measured reflectivity. The profile generating the best fitting reflectivity curve can then be compared to cross-sectional slices of the film's chemical composition predicted, for example, by molecular dynamics simulations [1]. However, the uniqueness of a profile obtained by conventional analysis of the film's reflectivity alone cannot be established definitively without additional information. In practice, significantly different SLD profiles have been shown to yield calculated reflectivity curves with essentially equivalent goodness-of-fit to measured data [2], as illustrated in Fig. 1.

The existence of multiple solutions, only one of which can be physical, is especially problematic in cases where a key additional piece of structural or compositional information is lacking as can happen in the investigation of these biological membrane systems.

Why this inherent uncertainty? The neutron specular reflection amplitude for a model SLD can be computed exactly from first principles; the square of its modulus gives the measurable reflectivity. It is firmly established, however, that the complex amplitude is necessary and sufficient for a unique solution of the inverse problem, that of recovering the SLD from reflection measurements. Unambiguous inversion requires both the magnitude and phase of reflection. Once these are known, practical methods [3] exist for extracting the desired SLD.

In fact, considerable efforts were made about a quarter century ago to solve the analogous "phase problem" in X-ray crystallography using known constraints on the scattering electron density [4] and by the technique of isomorphic substitution [5]. Variations of the latter approach have been applied to reflectivity, using a known reference layer in a composite film in place of atomic substitutions. These

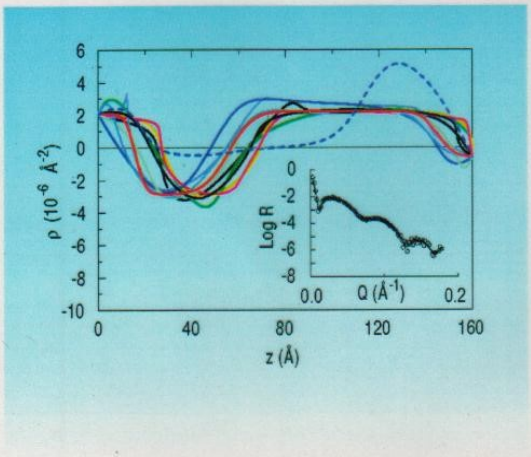

FIGURE 1. Family of scattering length density profiles obtained by model-independent fitting of the reflectivity data in the inset. The profile represented by the blue dashed line is unphysical for this Ti/TiO film system yet generates a reflectivity curve that fits the data with essentially equivalent goodness-of-fit (all the reflectivity curves corresponding to the SLD's shown are plotted in the inset but are practically indistinguishable from one another).

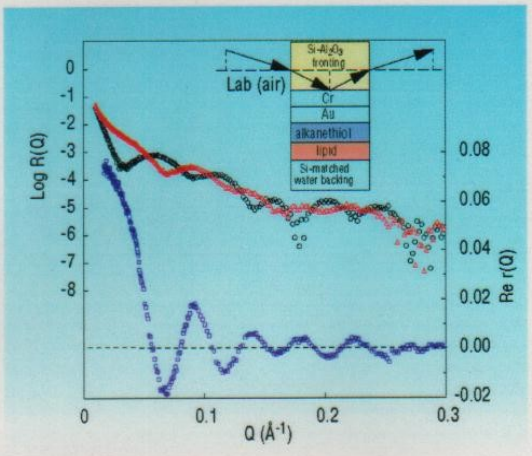

FIGURE 2. Reflectivity curves for the thin film system depicted schematically in the inset, one for a Si fronting (red triangles), the other for Al_2O_3 (black circles). The curve in the lower part of the figure (blue squares) is the real part of the complex reflection amplitude for the films obtained from the reflectivity curves by the method described in the text.

C. F. Majkrzak, N. F. Berk, S. Krueger, J. A. Dura
NIST Center for Neutron Research
National Institute of Standards and Technology
Gaithersburg, MD 20899-8562

C. W. Meuse, V. Silin, J. Woodward, A. L. Plant
NIST Biotechnology Division
National Institute of Standards and Technology
Gaithersburg, MD 20899-8311

M. Tarek
Department of Chemistry
University of Pennsylvania
Philadelphia, PA 19103

solution methods, however, were tied to the Born approximation, which generally is valid in crystal structure determination but which fails catastrophically at low Q (low glancing angles) in reflection from slab-shaped samples such as thin films. Exact inversion requires accurate knowledge of the reflection amplitude over the entire Q-range, especially at low Q.

In this decade the reflection phase problem has been exactly solved using a protocol of three reflectivity measurements on composite films consisting of the film of interest in intimate contact with each of three known reference layers [6, 7]. Subsequently, variations using only two measurements have been shown to partially solve the phase problem, an additional procedure being required to choose between two solution branches, only one of which is physical [8, 9]. In the past year [10], an exact solution has been found for a two measurement strategy in which the film surround, either the fronting (incident) or backing (transmitting) medium, is varied. This new approach is simpler to apply than reference layer methods and is adaptable to many experiments. Surround variation neutron reflectometry has been successfully applied to the challenging type of biological membrane depth profiling described earlier.

In Fig. 2 are plotted a pair of neutron reflectivity curves measured for the layered film structure schematically depicted in the upper right inset, one with Si and the other with Al_2O_3 as the fronting medium. The lower part of Fig. 2 shows the real part of the complex reflection amplitude for the multilayer as extracted from the reflectivity data, according to the method described above, and which was subsequently used to perform the inversion to obtain the SLD shown in Fig. 3. For comparison, the SLD predicted by a molecular dynamics simulation is also shown in Fig. 3, in a slightly distorted version, corresponding to a truncated reflectivity data set, which indicates the spatial resolution of an SLD obtainable in practice. This latter SLD was obtained by inversion of the reflection amplitude computed for the exact model SLD, but using values only up to the same maximum Q value (0.3 $Å^{-1}$) over which the actual reflectivity data sets were collected. Overall, agreement between the experimentally determined profile and the theoretical prediction is remarkable, essentially limited only by the Q-range of the measurement. Surround variation neutron reflectivity thus makes it possible to measure complicated thin film structures without the ambiguity associated with curve fitting. The veridical SLD profile is obtained directly by a first principles inversion.

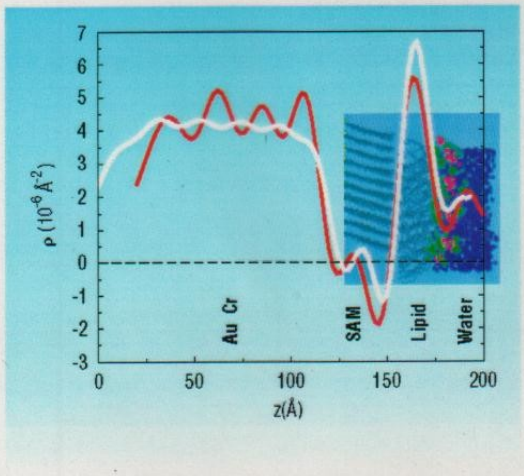

FIGURE 3. SLD profile (red line) resulting from a direct inversion of the Re r of Fig. 2 compared with that predicted by a molecular dynamics simulation (white line) as discussed in the text. The headgroup for the Self-Assembled-Monolayer (SAM) at the Au surface in the actual experiment was ethylene oxide and was not included in the simulation but, rather, modelled separately as part of the Au. Also, the Cr-Au layer used in the model happened to be 20 Å thicker than that actually measured in the experiment.

REFERENCES:

[1] M. Tarek, K. Tu, M.L. Klein, and D. J. Tobias, Biophys. J. **77**, 964 (1999).
[2] N. F. Berk and C. F. Majkrzak, Phys. Rev. B **51**, 11296 (1995).
[3] P. E. Sacks, Wave Motion **18**, 21 (1993).
[4] H. A. Hauptman, Science **233**, 178 (1986).
[5] J. M. Cowley, *Diffraction Physics*, 2nd Ed., (North Holland, Amsterdam, 1990), p. 131.
[6] C. F. Majkrzak and N. F. Berk, Phys. Rev. B **52**, 10825 (1995).
[7] V.O. deHaan, A. A. van Well, S. Adenwalla, and G.P. Felcher, Phys. Rev. B **52**, 10830 (1995).
[8] T. Aktosun and P. E. Sacks, Inverse Problems **14**, 211 (1998).
[9] C. F. Majkrzak and N. F. Berk, Physica B **267-268**, 168 (1999).
[10] C. F. Majkrzak and N. F. Berk, Phys. Rev. B **58**, 15416 (1998).

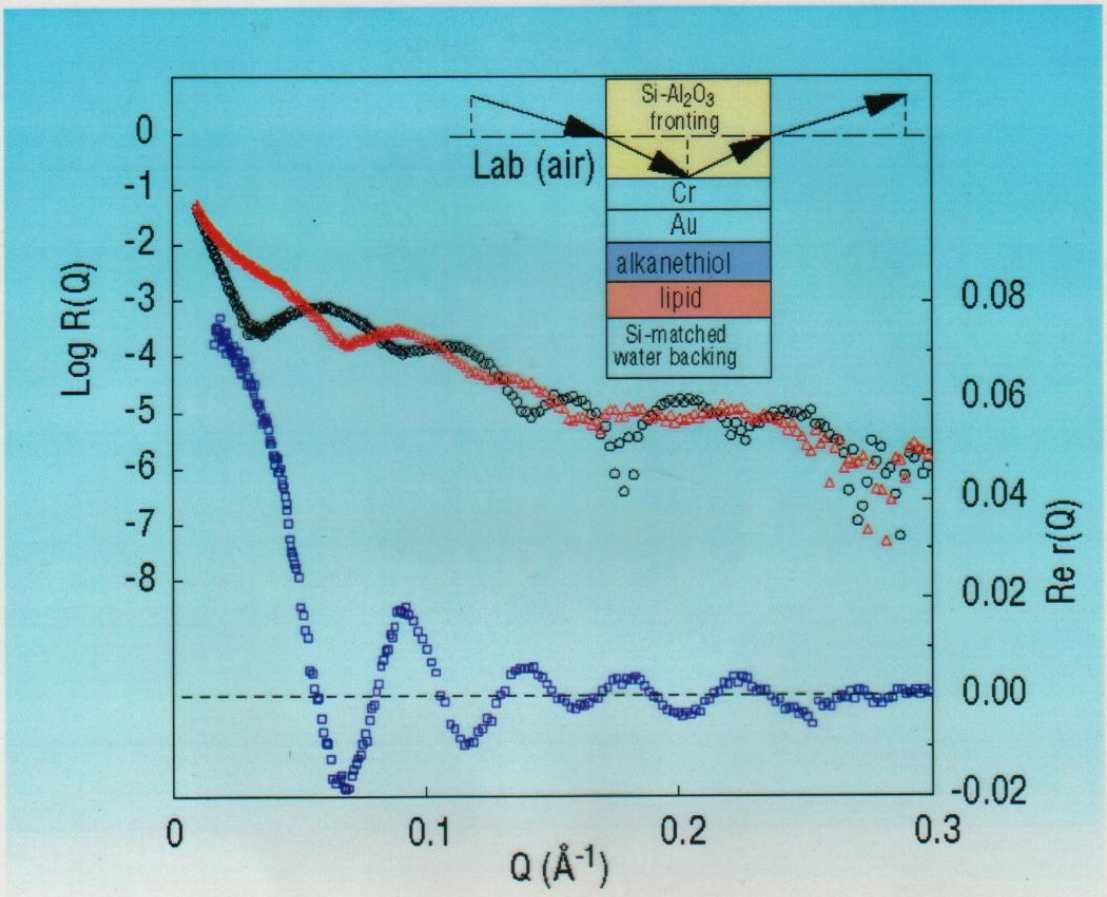

FIGURE 2. Reflectivity curves for the thin film system depicted schematically in the inset, one for a Si fronting (red triangles), the other for Al_2O_3 (black circles). The curve in the lower part of the figure (blue squares) is the real part of the complex reflection amplitude for the films obtained from the reflectivity curves by the method described in the text.

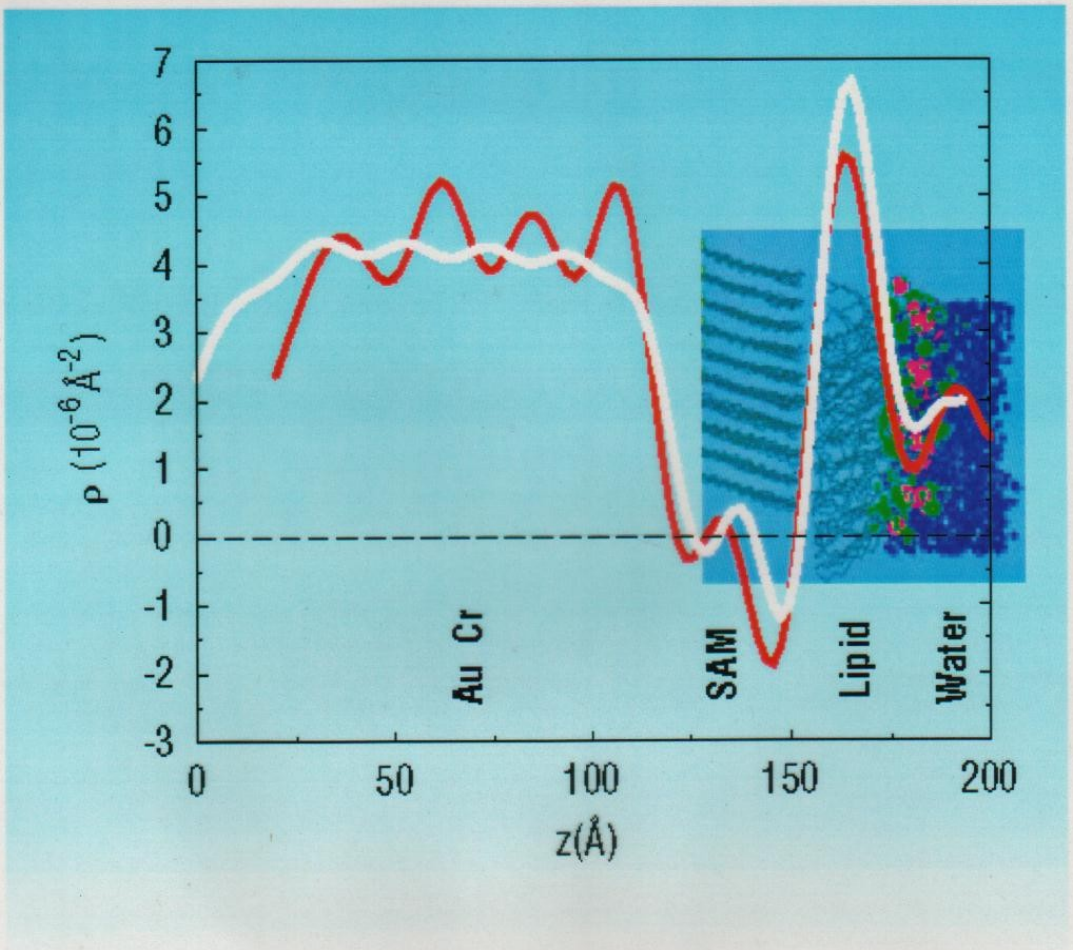

FIGURE 3. SLD profile (red line) resulting from a direct inversion of the Re r of Fig. 2 compared with that predicted by a molecular dynamics simulation (white line) as discussed in the text. The headgroup for the Self-Assembled-Monolayer (SAM) at the Au surface in the actual experiment was ethylene oxide and was not included in the simulation but, rather, modelled separately as part of the Au. Also, the Cr-Au layer used in the model happened to be 20 Å thicker than that actually measured in the experiment.

$$F^{\pm\pm} \propto \sum_{j=1}^{N} \left[b_{s_j} \pm P_{s_j} \cos\phi_j \right] e^{iQu_j}$$

$$F^{\pm\mp} \propto \sum_{j=1}^{N} P_{s_j} \sin\phi_j \, e^{iQu_j}$$

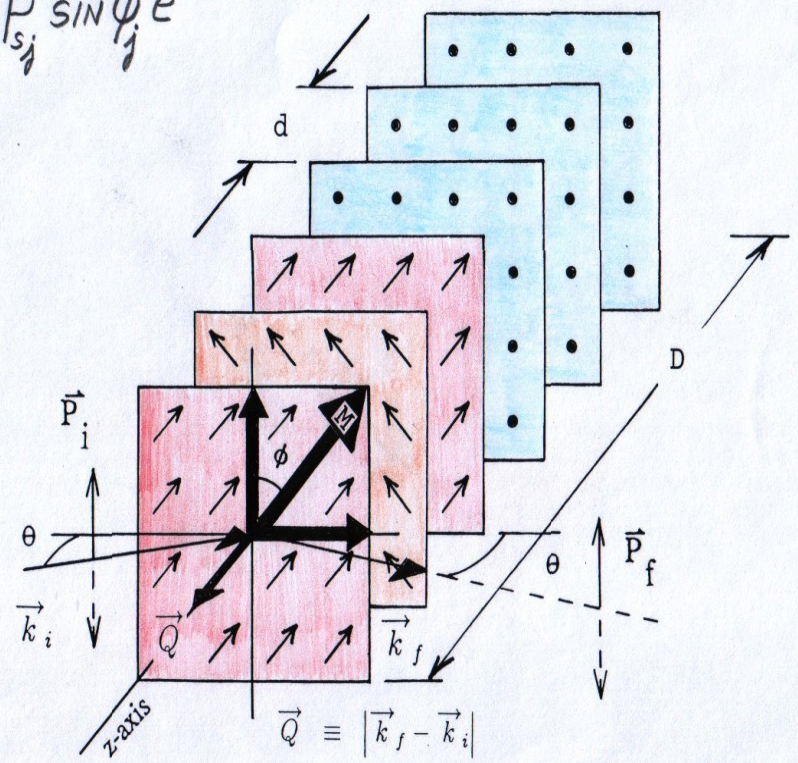

Epitaxial Growth of Superlattices

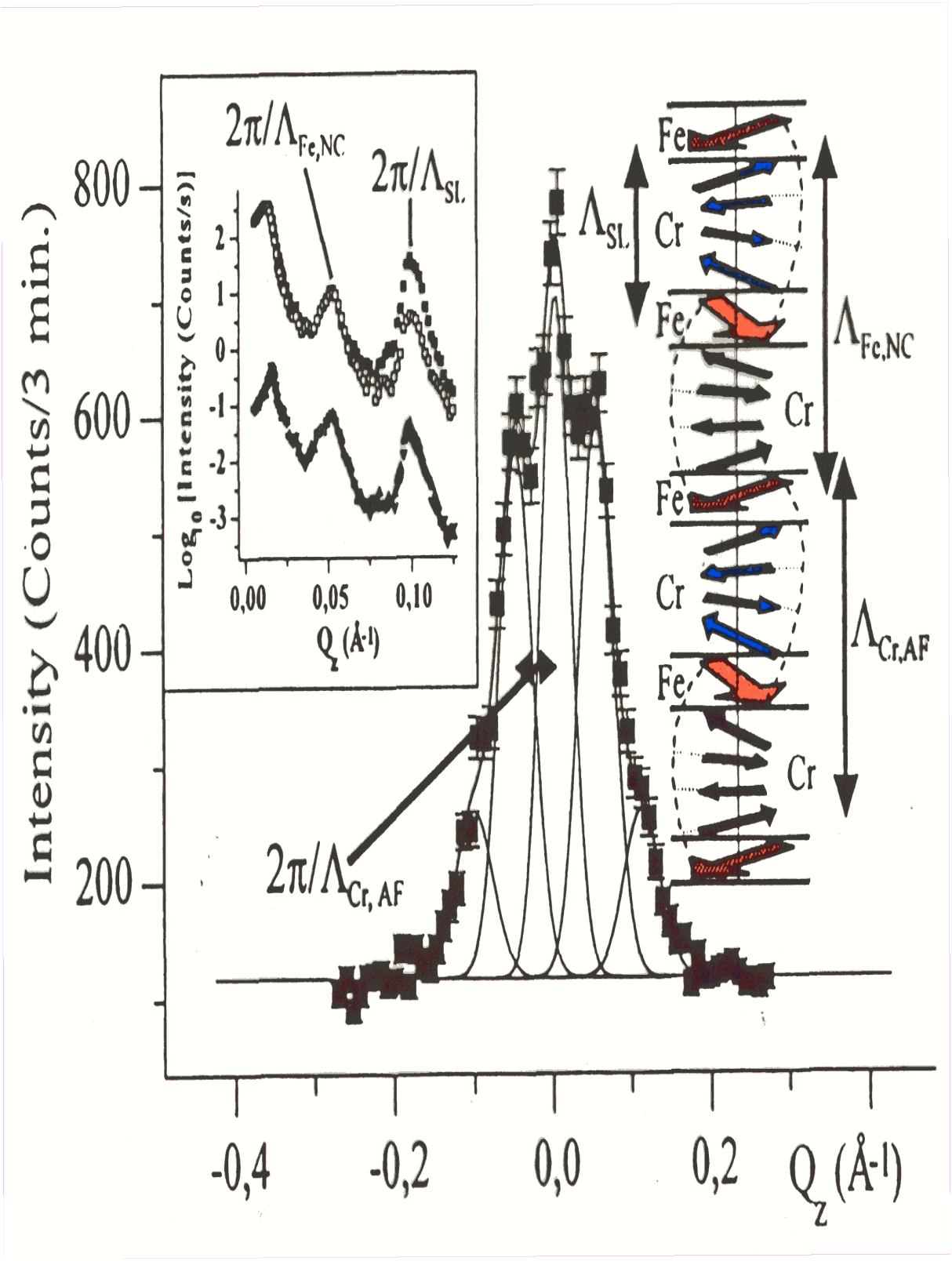

(Andreas Schreyer et al. - polarized neutron reflection/diffraction)

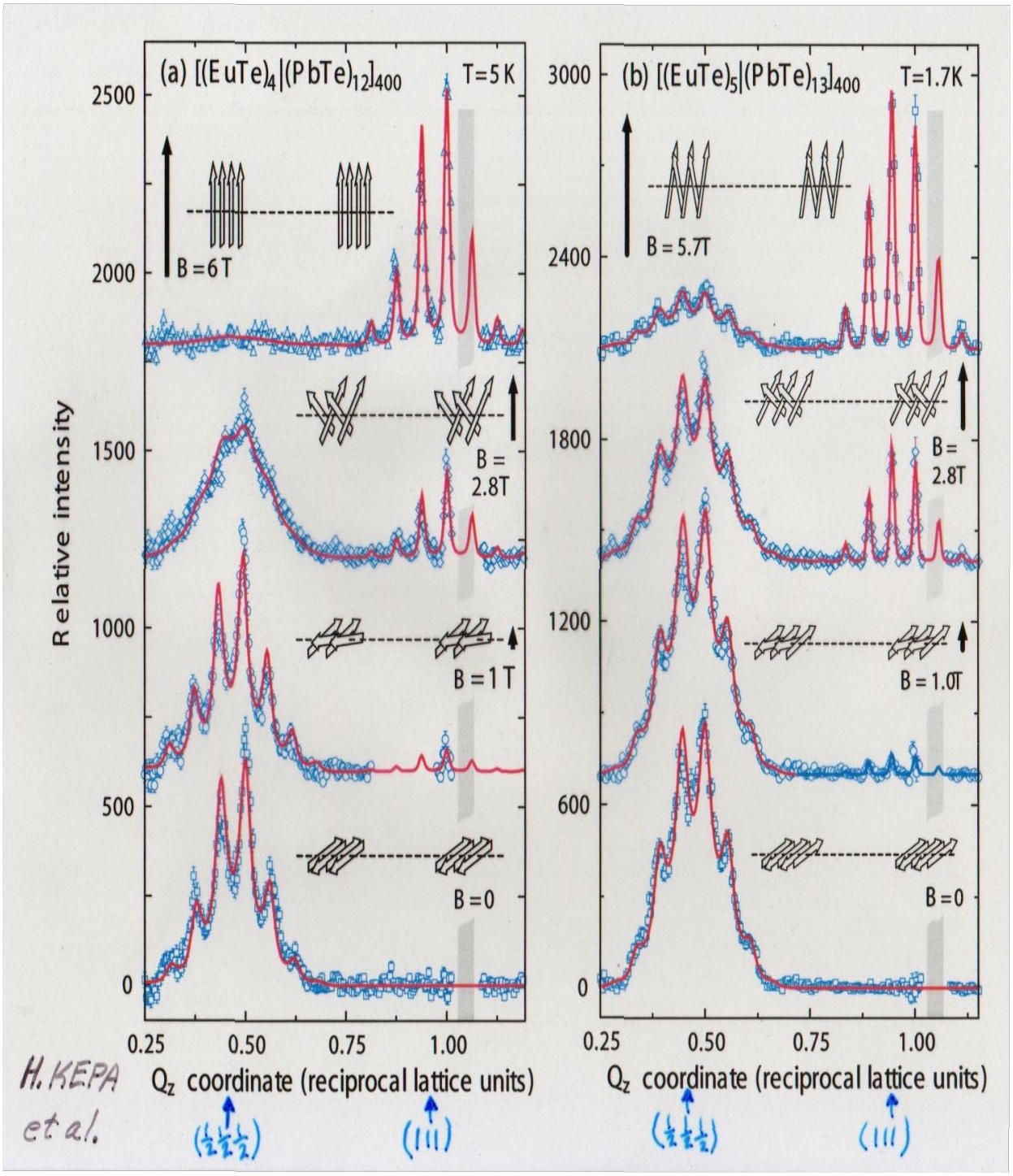
(a) [(EuTe)4|(PbTe)12]400
T=5 K
B = 6 T
B = 2.8T
B = 1 T
B = 0
(b) [(EuTe)5|(PbTe)13]400
T=1.7K
B = 5.7T
B = 2.8T
B = 1.0T
B = 0
Relative intensity
Qz coordinate (reciprocal lattice units)
0.25
0.50
0.75
1.00
(111)
H. KEPA
et al.

REFERENCES

* Optics, 3rd Ed., by E.Hecht, Addison Wesley, 1998.

* Neutron Optics, by V.F.Sears, Oxford University Press, 1989.

* Principles of Optics, 6th Ed., by M.Born and E.Wolf, Pergamon Press, 1987.

* Quantum Mechanics, 2nd Ed., by E.Merzbacher, Wiley, 1970.

* Magnetic Multilayers, Ed. by L.H.Bennett and R.E.Watson; article on "Neutron and X-Ray Diffraction Studies of Magnetic Multilayers" by C.F.Majkrzak, J.F.Ankner, N.F.Berk, and D.Gibbs, World Scientific, 1994, p.299 (contains introductory material on neutron and x-ray reflectometry not specific to magnetic materials alone)

* Neutron Reflectometry Studies of Thin Films and Multilayered Materials, C.F.Majkrzak, Acta Physica Polonica A 96, 81(1999) -- this article can also be found at the website: http://www.ncnr.nist.gov -- along with some additional information on analysing neutron reflectivity data (click on "Summer School Course Materials")

“Structural Investigations of Membranes in Biology by Neutron Reflectometry”, C.F.Majkrzak, N.F.Berk, S.Krueger, and U.A.Perez-Salas, Chapter 12 in *Neutron Scattering in Biology*, Edited by J.Fitter, T.Gutberlet, and J.Katsaras, (Springer, Berlin, 2006) p.225-263.

“Polarized Neutron Reflectometry”, C.F.Majkrzak, K.V.O'Donovan, and N.F.Berk, Chapter 9 in *Neutron Scattering from Magnetic Materials*, Edited by T.Chatterji, (Elsevier, Amsterdam, 2006) p.397-471.

“Phase-Sensitive Neutron Reflectometry”, C.F.Majkrzak, N.F.Berk, and U.A.Perez-Salas, *Langmuir* **19**, 7796 – 7810 (2003).